POLITECNICO DI TORINO

I Facoltà di Ingegneria

Corso di Laurea in Ingegneria Nucleare

TESI DI LAUREA

CERN-THESIS-2002-015
19/03/2001

Quench propagation in High Temperature Superconducting materials integrated in high current leads.

Supervisors
Prof. Giovanni Del Tin (Politecnico)

Dott.ssa Amalia Ballarino (CERN)

Candidate
Davide Milani Luca

March 2001

To my family

Acknowledgements

This work has been made at CERN of Geneva in the LCH/ICP group, and it has been sponsored by the ASP association (Associazione per lo Sviluppo Scientifico e Tecnologico del Piemonte), which I thank.

First of all I wish to thank Professor G. Del Tin, from “Politecnico di Torino”, who gave me the possibility to come here, and I would like to thank Dr. A. Ballarino for the help she gave me during this year.

But the most important aspect of this work, a part from the scientific results, is that it represents the achievement of a formative path. A path that lasts several years during which I met a lot of people in the work and in the everyday life, who helped me to carry on and who enriched me with their being there.

It is to all these people that I owe my gratitude. Thanks all.

Preface

This thesis is the upshot of a research activity carried out at CERN in Geneva, in the LHC/ICP group.

It concerns the design and the optimisation of the high temperature superconducting (HTS) current leads for the powering of the superconducting magnets of the Large Hadron Collider (LHC): the new particle accelerator presently under construction at CERN. This high-energy machine requires low-temperature superconducting magnets, operating in superfluid helium at 1.9 K and 1.3 bar, to provide the necessary magnetic field to guide the particles. This implies a huge cryogenic system necessary to operate the accelerator.

The use of the high temperature superconductors technology for the current leads is made necessary to reduce the heat load into the cryogenic apparatus used to cool down the cold mass of the machine and so to limit the cooling power required, otherwise too onerous from the economic point of view.

The LHC current leads are made of a traditional copper conductor in the upper part, from 300 K to about 50 K, and by a superconducting part in the last track, from 50 K to 4.5 K. For this reason these current leads are called: *hybrid.*

My work is concentrated on the superconducting part of these leads.

I first characterised with electrical measurements, some samples of superconducting materials in order to assess their properties and the state of art regarding the high temperature superconductors technology. The HTS materials currently available for industrial purpose are of three types: YBCO 123 and BSCCO 2212 bulk material, and BSCCO 2223 tapes sheathed with a silver alloy matrix. To the purpose of the current leads each of these materials can be used. The choice depends on the special requirements of the circuit in which the leads will be integrated. My work is concentrated on the study of HTS assemblies, for lead application, made with BSCCO 2223 tapes.

Then I developed a thermal model to study the quench propagation in the HTS, that is the resistive transition of the superconducting materials. The main task of the theoretical model is to find the best configuration for the leads in order to prevent quench to occur and to limit its propagation in case of accident.

The theoretical model has been validated by the experiments on a 13 kA current lead prototypes. It has been used to study the influence of all the design parameters in the evolution of quench in order to find the optimum configuration and to be aware about the importance of each design parameter: type of metal matrix, critical current for the tapes, contact resistance, cooling parameters etc... The study of the quench evolution, then, allows to set up the parameters for the quench detection system that will be used to protect the leads once installed in the LHC machine.

Table of Contents

Glossary of symbols

$\dot{m}$	[kg/s]	Mass flow rate
ρ	[Ω m]	Electrical resistivity
θ	[K]	Gas temperature (Helium)
ν	[kg/m³]	Density
μ	[N/(s m²)]	Dynamic viscosity
μ/ν	[m²/s]	Cinematic viscosity
A	[m²]	Tape's cross section
C	[m]	Wet perimeter
c_p	[J/(kg K)]	Specific heat
D_{eq}	[m]	Equivalent diameter
dV	[V]	Voltage drop across the HTS
E	[V/m]	Electric field
E_c	[V/m]	Critical electric field
fu		Filling factor
h	[W/(m² K)]	Coefficient of thermal convection
He		Helium
h_{fg}	[J/kg]	Latent heat of evaporation
HTS		High temperature superconductor
I_c	[A]	Critical current
J_c	[A/m²]	Critical current density
k	[W/(m K)]	Coefficient of thermal conduction
L	[m]	Tape's length
n		Number of tapes
Q	[W]	Heat flow
Q2	[W]	Heat flow @ 4.5 K
Q_{min}	[W]	Minimum heat flow
R_c	[Ω]	Electrical contact resistance
S	[m²]	Cooling channel cross section
T0	[K]	Temperature of the upper end of the tape

T_c	[K]	Critical temperature
T_{cs}	[K]	Temperature of current sharing
T_H	[K]	Higher temperature
T_{HTS}	[K]	Tape’s temperature
T_L	[K]	Lower temperature
T_{lim}	[K]	Maximum allowable temperature
TN	[K]	Temperature of the lower end of the tape
U	[V]	Electric voltage
W_t	[J]	Total generated heat during transient

1 *Introduction*

1.1 An overview of the LHC

As more and more of fundamental physics is researched, the need for more energetic nuclear collisions increases. Particle physics beyond the domain explored with the electron positron collider (LEP) calls for an energy range of more than 1 TeV for the elementary constituents of matter, i.e. leptons or quarks.

This can not be achieved by upgrading the existing LEP or by building a larger electron positron collider: the synchrotron radiation forbids it. The energy losses due to the synchrotron radiation vary with the fourth power of the particle energy. The only way to achieve such high energies is to accelerate and collide protons. Their mass, 2000 times larger than the electron's one, leads to a considerable reduction of the radiation losses. The limiting factors, in this case, are the maximum magnetic guiding field and the proton trajectory radius.

The construction of a new accelerator at CERN, the Large Hadron Collider (LHC), was approved by the CERN council in 1994 [1]. It is designed to provide proton-proton collisions with centre-of-mass energy of 14 TeV and luminosity of 10^{34} $cm^{-2}s^{-1}$. It will also be able to collide heavy ions, such as lead, up to 1100 TeV. It is predicted that these collisions will cause phase transition of nuclear matter into quark-gluon plasma (as would have been observed about 10^{-10} s after the big bang), thus giving an insight into the initial structure of the universe.

The LHC will be installed in the existing LEP tunnel, 26.7 km in circumference. Existing particle sources and pre-accelerators will provide the beam, which will be held in orbit by a total of about 1000 main dipole magnets. A guiding field, increasing with particle energy will keep the orbit stationary.

Superconducting magnets with a nominal field of 8.4 T in 1.9 K superfluid helium will allow the storage of proton beams with an energy of up to 7 TeV per beam. The counter-rotating beams require two separate magnetic channels but due to the lack of space in the LEP tunnel, "two-in-one" magnets have been designed. In order to deflect the counter-rotating proton beams, the field direction in the apertures must be opposite. The quality of the magnetic field is essential to keep the particles on stable trajectories for about 10^8 turns.

Altogether, the LHC will contain about 3444 super-conducting magnets including 1232 main dipoles and 386 main quadrupoles. In addition, 4928 corrector magnets will be added, giving a grand total of around 8400 magnets.

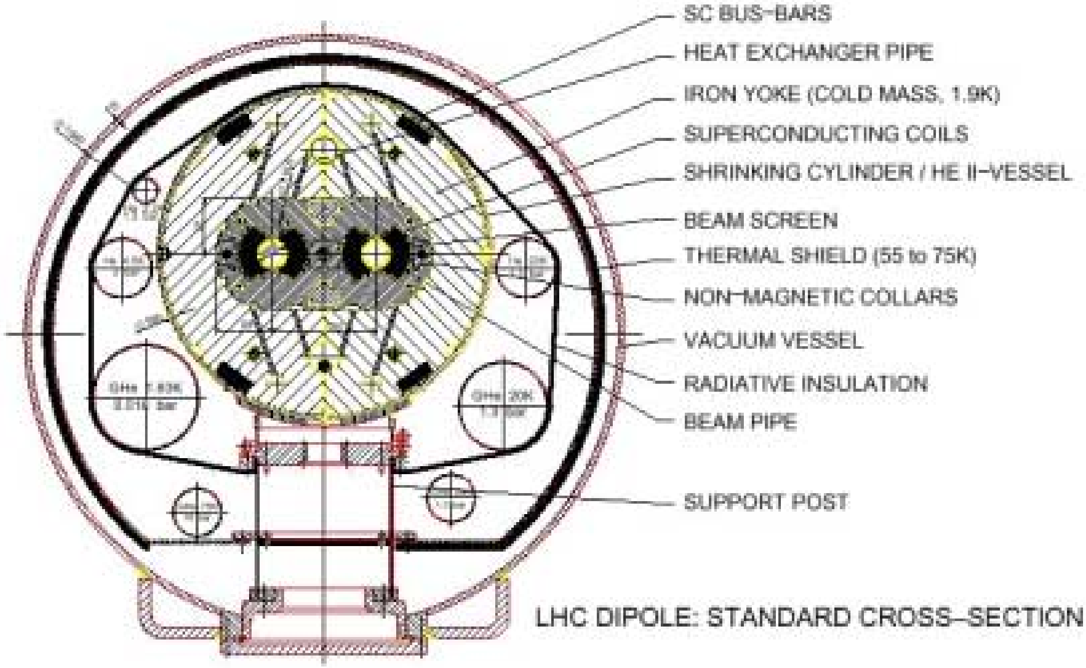

Figure 1-1. LHC dipole.

To power the magnets a total electrical current of about 3.5 MA must pass from the power converters, at room temperature, through the insulating vacuum and into the liquid helium environment. Using conventional conductors, this means a huge quantity of energy losses due to the Joule heating and a heavy load of the cryogenic lines. To solve this problem, LHC will use high temperature superconductors (HTS) in the lower part of the lead, giving a substantial saving in the cryogenic apparatus.

1.2 Technical description

The LHC layout is defined and constrained by the LEP tunnel geometry (see Figure 1-2).

The machine consists of eight bending arcs separated by eight straight sections, each approximately 528 m long, available for experimental insertions or utilities.

Of these only 4 will have experiments. The two high luminosity insertions, located at diametrically opposite straight sections: point 1 (ATLAS) and point 5 (CMS); and the two more low-beta insertions located at point 2 (ALICE Pb ions) and point 8 (B physics). The latter straight sections also contain the injection systems. The beams cross from one ring to the other only in these four locations.

The remaining four straight sections do not have beam crossing. Insertions 3 and 7 each contain two beam collimator systems using only resistive magnets: they are used for beam "cleaning" and collimation. Insertion 4 contains the Radio Frequency (RF) systems: one for each beam. Finally the straight section at point 6 contains the beam dump insertion: for the vertical extraction of the beams.

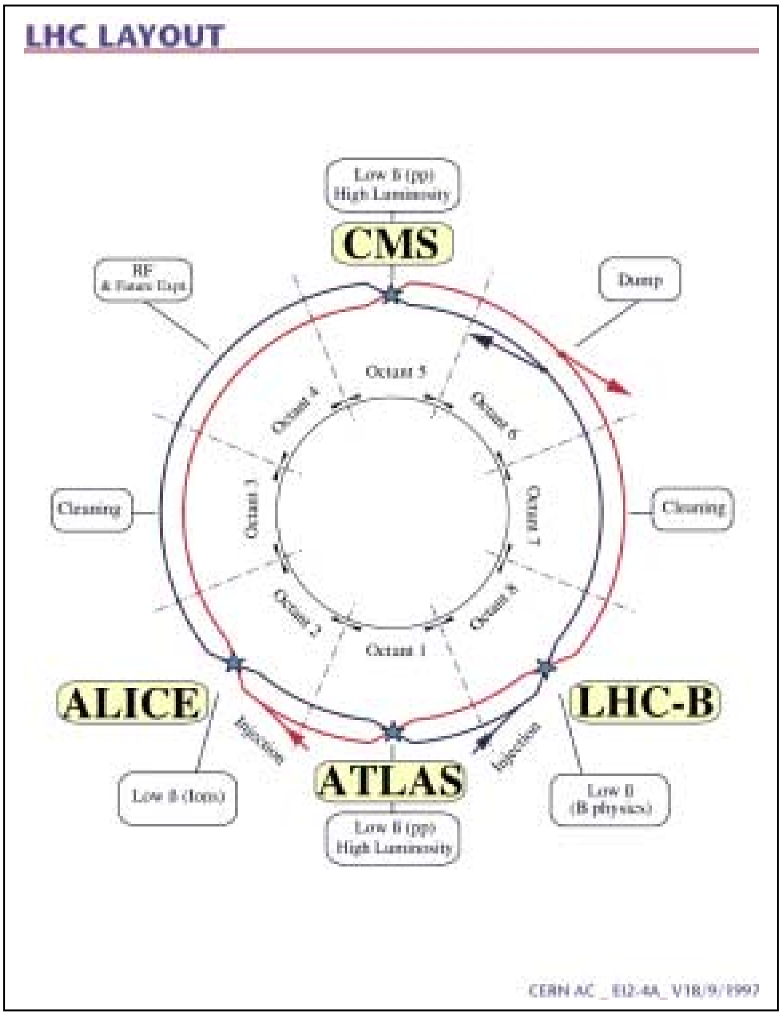

Figure 1-2. Schematic layout of LHC.

The main performance parameters are reported in the Table 1-1 [2].

Table 1-1: LHC performance parameters.

Energy	[TeV]	7.0
Dipole Field	[T]	8.4
Coil aperture	[mm]	56
Distance between apertures	[mm]	194
Luminosity	[cm^{-2} s^{-1}]	10^{34}
Beam-beam parameter		0.0034
Injection energy	[GeV]	450
Circulating current / beam	[A]	0.54
Bunch spacing	[ns]	25
Particles per bunch		10^{11}
Stored beam energy	[MJ]	334
Full crossing angle	[μrad]	200
Beam lifetime	[h]	22
Luminosity lifetime	[h]	10
Energy loss per turn	[keV]	6.7
Total radiated power per beam	[kW]	3.6

1.2.1 Optics and layout

The LHC circumference is made of eight arcs separated by straight insertions. Each of the eight arcs is composed of 23 arc cells giving a total arc length of 2456.160 m. All the arc cells are made of two identical half cells (see Figure 1-3).

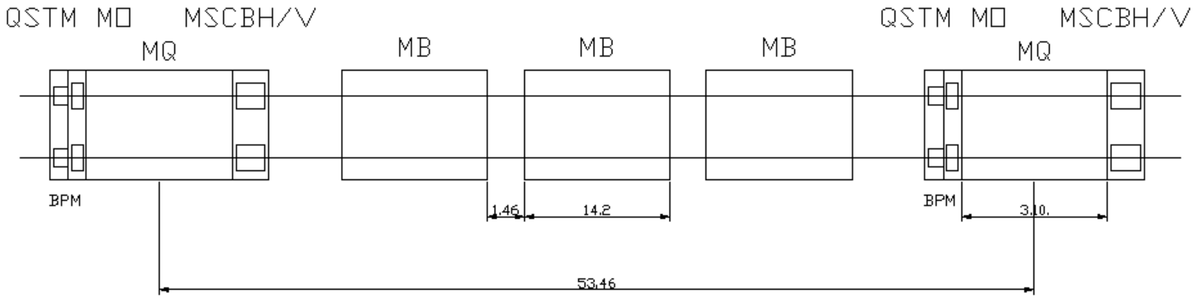

Figure 1-3. Layout of the arc half-cell.

Each half-arc cell consists of a string of three 14.2 m, twin aperture dipoles and one 3.10 m quadrupole separated from the string by 2.42 m. In the shadow of the dipole magnet ends, sextupole and decapole correctors are located respectively on the right and left side.

The arc quadrupole assembly has on its left side a beam position monitor (BPM) and an octupole, and on its right side a combined sextupole/dipole corrector.

The two dispersion suppressor (DS) cells consist of four quadrupoles interleaved with four strings of two dipoles each. They are placed after and before each straight section to adjust the beam parameters. The four DS quadrupoles are all powered in series with the arc cell quadrupoles.

The two high luminosity insertions at point 1 and 5 comprise the following sections:

- free space of 23 m on each side of the IP; a secondary particle absorber is placed 19 m from the IPs;
- low-β (or 'inner') quadrupole triplet;
- pair of separation dipoles;
- the matching (or 'outer') quadrupole triplet.

The inner triplet comprises four 5.5 m quadrupole magnets powered in series: Q1 and Q3 focusing magnet and Q2a and Q2b defocusing magnet (Figure 1-4). In the front of the triplet casing, only for the high luminosity insertion point (HL-IPs) there is a 21.6 m long absorber element for reason of alignment and protection from secondary particles. Finally there are two long trim quadrupole magnets individually powered. The separation magnets are two bending magnet D1 and D2. The outer triplet consists of several units of DS type quadrupoles.

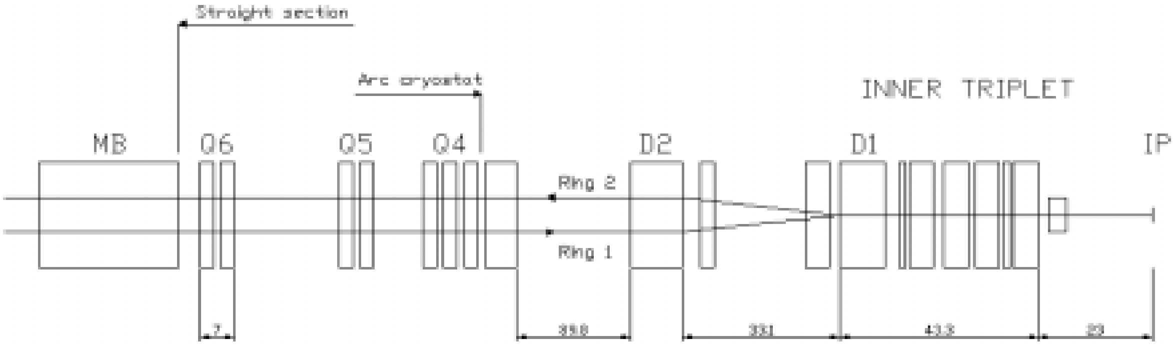

Figure 1-4. Layout of the Low-β Insertion 1 and 5.

The two other experimental insertion points (point 2 and 8) are the same except for the injection section. The injection system consists of a horizontally deflecting magnet and a cooper septum magnet, a kicker magnet and three dipoles to adjust the orbit. At the end of the assembly there is a series of injection beam stoppers to protect machine components from a badly injected beam.

The very important beam collimation functions are carried out in the betatron and momentum cleaning sections at point 3 and point 7. The betatron cleaning is settled at point 3: the deep underground location and the impossibility of any civil engineering work make it a well suited location for this function which inevitably produces large background radiation. The momentum cleaning is tentatively located in IP7 and has the same hardware layout as IP3.

The radio frequency (RF) system is settled in IP4. There are two separate RF systems, one for each beam. They are both equipped with a pair of dipoles (D3 and D4) to increase the nominal beam separation near the outer triplet.

The beam dump at IP6 has the purpose to remove the beam safely from the collider at the end of a physic run, when the luminosity has degraded and a refill is necessary. It will also be used frequently during setting up and machine studies and must always be ready in case of equipment malfunctions or abnormal beam behaviour, which might lead to beam loss and quenching of superconducting magnets. The principle is to horizontally kick the circulating beam into an iron septum magnet which bends the beam vertically so that it can be transported to an external zone sufficiently far away to permit beam dilution and shielding.

1.2.2 Cryogenics

To profit at the maximum of the well established Nb-Ti conductors technology, the LHC operates in pressurised superfluid helium below 2 K. In fact, the critical current density at this temperature for Nb-Ti wires is about 8 kA/mm^2, while it is only 5 kA/mm^2 at 4K, in absence of magnetic field.

The low bulk viscosity enables the coolant to permeate the heart of the magnet windings, while the very large specific heat (typically 10^5 times that of the conductor per unit mass), combined with the enormous heat conductivity at moderate flux may have a powerful stabilising action against thermal disturbances. Cooling more than 31000 tons of material, spread over 26.7 km, to below 2 K presents a considerable technological challenge.

As mentioned above the LHC will be installed in the existing circumference tunnel, which presently houses the LEP electron-positron collider.

The LHC magnets lie deep underground in the tunnel with access shaft to ground level and technical service areas only at the end of each sector. A direct consequence of these constraints is the cryogenic layout of the machine, with five cryogenic islands where all refrigeration and ancillary equipment is concentrated, both at ground level and underground. Each cryogenic island then feeds one or two adjacent tunnel sectors, which requires distributing and recovering the helium over distances of 3.3 km underground. This is achieved by means of a cryogenic distribution line, which runs along the cryomagnet string in the tunnel and feeds every 106.9 m long lattice cell [3].

The machine will be cooled by eight cryoplants, each with an equivalent capacity of 18 kW at 4.5 K [4]. Four of these will be the existing LEP refrigerators upgraded in capacity from 12 to 18 kW and adapted for LHC duty. The other four new plants, unlike those of LEP, will be entirely installed on the surface, reducing the need for additional underground infrastructure.

The LHC cryogenic system is required to:

- maintain the pressurised (1.3 bar) superfluid helium bath of all cryomagnets around the ring at their nominal temperature below 1.9 K;
- cool down from ambient temperature and fill each sector of the machine in less than two weeks;
- accommodate resistive transition of full cells of the machine lattice and recover from this transition in less than two hours, while minimising loss of cryogen and system perturbation.

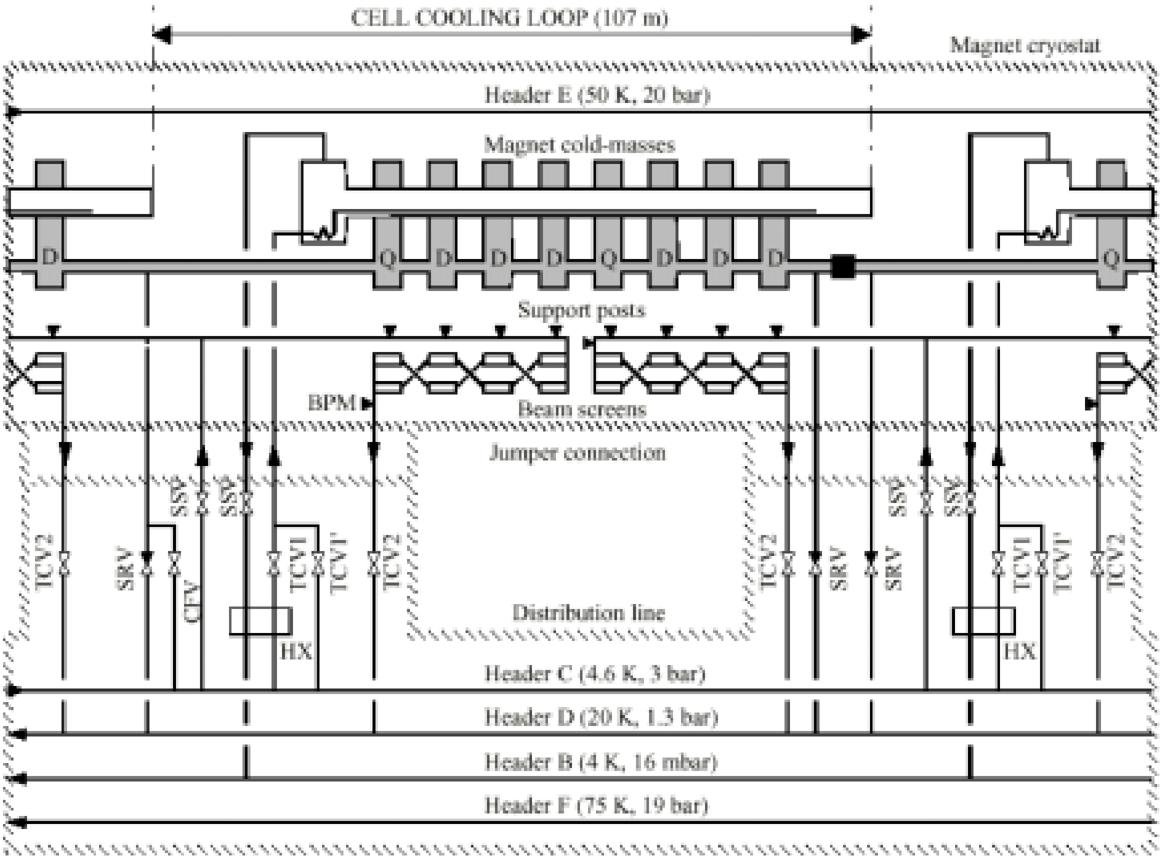

Figure 1-5. Cryogenic flow-scheme of LHC lattice cell.

To fulfil these requirements within the above constraint and boundary conditions, the LHC cryogenic system makes use of helium in several thermodynamic states. The flow scheme of a LHC lattice cell appears in Figure 1-5.

The cryomagnets operate in a static bath of pressurised helium II (see Chapter 5 for the helium phase diagram), cooled by heat exchange with flowing saturated helium II. Low temperature vapour resulting from the vaporisation of the saturated helium II is returned to the refrigerator by header B. Supercritical helium, distributed by header C, is used to fill the cryomagnet baths, to produce – after subcooling and Joule Thomson expansion – the saturated helium II flowing in the heat exchanger tubes, and to feed line C' in series with the beam screens operating between 5 and 20 K. The resulting gaseous helium is returned to the refrigerator by line D.

The first level of thermal shielding and heat interception in the magnetic cryostats and distributions line is provided by forced circulation of gaseous helium under pressure at temperature between 50 and 75 K through lines E and F respectively.

Special magnets which do not require cooling at 1.9 K operate in baths of saturated helium I at 4.5 K. Also 4.5 K helium I is used to cool the lower part of the

HTS-based current leads, the upper, resistive part of which is cooled by gaseous helium between 20 K and ambient temperature.

The steady state heat loads are of three basic types:

- heat inleaks, resulting from the thermal conduction of the cryostats;
- resistive heating in the non-superconducting sections of the magnet excitation circuit, which have to be taken by the superfluid helium bath;
- beam-induced loads dominated by synchrotron radiation, dissipation of beam-image currents, and impingement of photoelectrons accelerated by the beam potential.

1.2.3 Powering

To power the magnets of LHC a total electrical current of about 3.5 MA must be transported into and out of the cold mass. In order to reduce the heat leak into the helium bath the LHC has chosen to adopt the HTS technology.

Due to the low required voltage for the alimentation, the power converters will be installed close to the magnets, in underground caverns and service tunnels at the even points, thus minimising the voltage drop along warm bus work.

The connection of all magnet circuits to their associated power converters requires a large number of current leads which, with the exception of the low current orbit correction dipole magnets, will be grouped at the ends of the arcs in distribution feed boxes (DFBs) which are also connected to the same cryoline of the magnets.

The 1232 dipoles magnet are connected in series, octant by octant, each circuit having a stored energy if 1.25 GJ at the maximum field level of 9 T. This magnets operate at up to 13 kA [5].

The focusing magnets, in number of 396, are twin aperture quadrupoles also connected in series, but in two circuits per octant. They also operate at up to 13 kA.

Focusing at the interaction point is obtained by special quadrupoles excited individually or in small families, operating at up to 6 kA.

In order to control the beam orbit and other specific beam parameters, corrector magnets are provided. These magnets are much smaller than the others and operate at currents of up to 60, 120 or 600 A.

In the Figure 1-6 is reported the current rating of the LHC current leads [6].

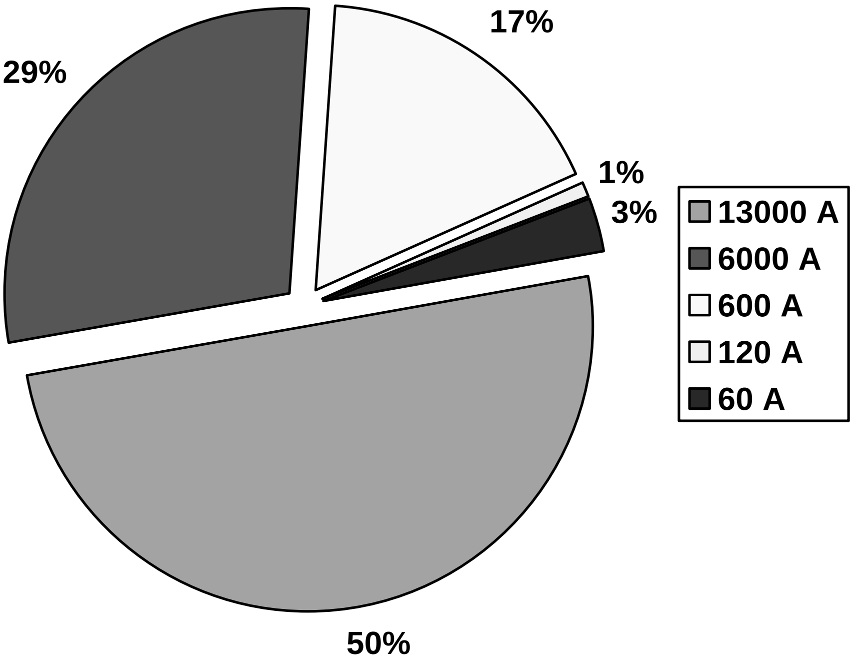

Figure 1-6. Current leads size: percentage of the total current (3.5 MA) distributed by a specific size of current lead. The current leads are marked, in the legend, with their size.

2 *Superconducting materials*

2.1 Introduction

The high current leads of the LHC use the superconductor's technology. A brief introduction on these materials is given to full understand the properties, performances and limits of these new ceramic materials.

Superconductivity was discovered in 1911 [7] by the Dutch physicist H. Kamerlingh Onnes, only three years after he had succeeded in liquefying helium. During his investigation on the conductivity of metals at low temperature he found that the resistance of a mercury sample dropped to an unmeasurably small value just at the boiling temperature of liquid helium. He called this phenomenon *superconductivity* and this name was retained since. The temperature at which the transition took place was called the *critical temperature* T_c.

Superconductivity is observed in a large variety of materials but not in the good electrical conductors like copper, silver and gold.

The discovery of superconductivity at 30 K in the La-Ba-Cu-O system by Bednorz and Müller in 1986 ignited an explosion of interest in high temperature superconductivity. These initial development rapidly evolved into an intense world-wide research effort that still persists after more than a decade, fuelled by the fact that high temperature superconductivity constitutes an extremely important and challenging intellectual problem and has an enormous potential for technological applications.

The discovery of the new oxide high-temperature superconductors in 1986 leads to a great deal of new works investigating their properties and their applications.

A great breakthrough occurred with the discovery of the yttrium-based compound with a critical temperature higher than the liquid nitrogen one. After that, rapidly, were discovered the Bi-compound that led the T_c up to 110 K. The use of liquid nitrogen as coolant, cheaper than helium, makes possible to simplify the cryostat design. So we can expect to operate high T_c superconductors with stable conditions even if there will be some amount of heat generation.

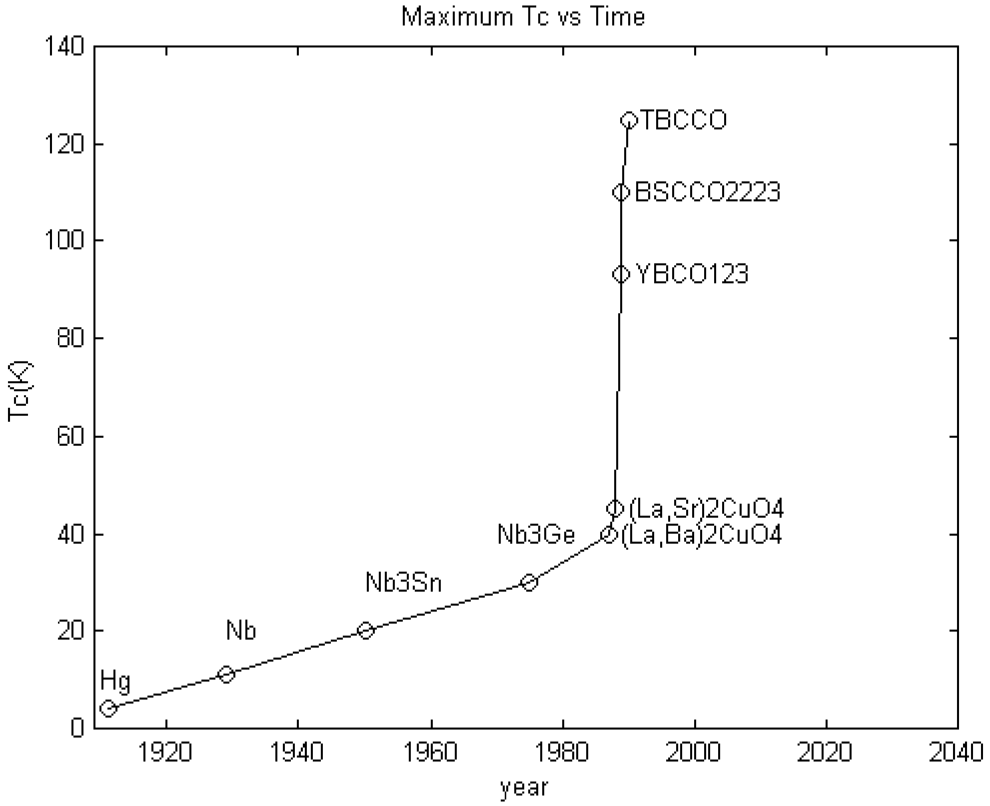

Figure 2-1. Highest known superconducting transition temperature as a function of time, since the discovery of superconductivity in 1911.

The use of these superconductors at the temperature of liquid nitrogen could greatly affect fields such as power generation, power transmission, magnetic energy storage, motors, electronics, medical technology and so on. Energy savings with the application of superconductors will be expected in the reduction of losses, the reduction of size of equipments and increase in efficiency.

The most natural employ of these new superconductors is the current lead application.

2.2 The discovery of High-T Superconductivity

A superconductor is usually referred to as high-temperature superconductor if the critical temperature T_c, the temperature at which occurs the normal-superconducting phase transition, is higher that the one of the Niobium-based superconductors. Then, if the superconducting state is attained by cooling in liquid nitrogen we are dealing with HTS.

In the following pages I will introduce the general theory about Low-Temperature superconductivity (the BCS model), to the purpose of understanding the situation that led to that discovery.

2.2.1 *BCS theory: basic concepts*

In a metal the positively charged ions form a regular crystal lattice. The valence electrons are not bound to specific ions but can move through the crystal.

In the simplest quantum theoretical model the Coulomb attraction of the positive ions is represented by a potential wall with flat bottom. The energy levels are computed by solving the Schroedinger equation; the electrons are placed on these levels following the Pauli exclusion principle: no more than two electrons of opposite spin are allowed on each level.

In this situation it is essential to apply the Fermi–Dirac statistic, based on the Pauli's principle and to avoid the classical Boltzmann statistic applied to normal gases, for which the average kinetic energy of the metal electrons is by no means given by the classical expression [8]

$$(1) \qquad \frac{1}{2}mv^2 = \frac{3}{2}k_B T$$

where m is the particle's mass, v its velocity, k_B the Boltzmann constant and T the thermodynamic temperature.

Instead, in the Fermi-Dirac statistic the energy levels are filled with two electrons each up to the so-called Fermi energy E_F. The electrons constitute a system called a "highly degenerate" Fermi gas. The Fermi energy is given by the formula

$$(2) \qquad E_F = \frac{\hbar^2}{2m}\left(3\pi^2 n_0\right)^{\frac{3}{2}}$$

the quantity $\nabla = h/2\pi = 6.58\ 10^{-15}\ eVs$ is the Planck's constant, and n_0 is the density of conduction electrons. Plotting the allowed quantum states of the electrons in the *momentum space* we obtain the so-called Fermi sphere: a sphere of radius equal to the maximum allowed momentum within which are located the occupied states.

These facts have some consequences on the study of the electrical conduction and the heat conduction: in both cases the most important carriers of electrical and thermal energy are the electrons; in the Fermi–Dirac statistic they obey to these rules so that not all the electrons of the metals can accept an additional momentum but only those on the right rim of the Fermi sphere have free states accessible.

Before trying to understand the vanishing resistance of a superconductor we have to explain why a normal metal has a resistance at all.

One can imagine collisions are the main responsible of the ohmic resistance. What is not so evident is that the collision centres are not the ion in the regular crystal lattice, but only imperfections:

- impurities;
- lattice defects;
- deviation of the metal ions from their nominal position due to thermal oscillation.

The last one is dominant at room temperature and gives rise to a resistivity that is roughly proportional to temperature while impurities and lattice defects are responsible for the residual resistivity at low temperature (<20 K).

All states inside the Fermi sphere are filled with electrons while all states outside are empty. In 1956 Cooper studied what would happen if two electrons were added to the filled Fermi sphere with equal but opposite momenta $\vec{p}_1 = -\vec{p}_2$; whose magnitude was slightly larger than the Fermi momentum p_F.

Assuming that an attractive force existed he was able to show that the electrons form a bounded system with energy less than twice the *Fermi energy:* $E_P < 2E_F$.

Realising that the Coulomb repulsion between the two electrons has a very short range as it is shielded by the positive ions and the other electrons in the metal, the attractive force must not be strong if the electrons are several lattice constants apart.

Already in 1950 Fröhlich and, independently, Bardeen had suggested that a dynamical lattice polarisation might create a weak attractive potential.

When an electron flies through the lattice it attracts the positive ions. Because of their inertia they cannot follow immediately: the shortest response time corresponds to the highest possible lattice vibration frequency (Debye frequency ω_D). The maximum lattice deformation lags behind the electron by a distance $d \cong v_F \dfrac{2\pi}{\omega_D}$; where v_F is the electron’s velocity.

The lattice deformation attracts the second electron because there is an accumulation of positive charges. The attraction is stronger when the second electron moves right along the track of the first one and when it is a distance d behind it.

This explains why a Cooper pair is a very extended object. In the space occupied by a Cooper pair there are about a million other Cooper pairs. The strong overlap is an important prerequisite of the BCS theory because the Cooper pairs must change partners frequently in order to provide a continuous binding.

Cooper, together with Bardeen and Schrieffer developed in 1957 a theory in order to explain this phenomena: the BCS theory, which gave them the Nobel Prize in 1972.

According to this theory the supercurrent is made up of Cooper pairs (electrons with opposite spin and momenta, attracted together).

The binding energy of these pairs results in an energy gap within which the density of states N(ε) = 0. The ground state has spin = 0. The maximum number of Cooper pairs is formed at temperatures close to 0 K. The pairs can be broken by thermal activation. At temperature $T>T_c$ all of the pairs are broken. When $T<T_c$ the broken pairs form a second fluid of normal electrons in a 2-fluid system.

The transition temperature (T_c) depends on several parameters according to the theory [9]:

- density of the electron state at the Fermi sphere $N(\varepsilon_F)$;
- attraction coupling constant V;
- energy shield of order ∇ω around the Fermi surface.

$$(3) \qquad \begin{aligned} k_B T_c &= 1.14\hbar\omega \ e^{-\frac{1}{N(\varepsilon_F)V}} \\ \lambda &= N(0)V \end{aligned}$$

The expression (3) determines the temperature below which the normal state of electrons becomes unstable with respect to the formation of a condensate of electron pairs with opposite spins and zero orbital momentum. The nature of the forces responsible for the effective attraction in the energy shell ∇ω is of no importance for derivation of (3). The BCS theory and the equation (3) can therefore be used to treat superconductivity in the case of other, i.e. non phononic, mechanism of attraction for the formation of electron pairs: generalised BCS pairing theory.

The electron attraction, which is responsible for superconductivity in conventional metals, is due to retarded electron-phonon interaction. It is related to the phonon energy and comes into play only in a narrow energy shell of order $\nabla\omega/k_B < 400$ K near the Fermi surface. The coupling constant itself depends on the phonon spectrum:

$$(4) \qquad \lambda = N(0)\left\langle g^2 \right\rangle \left\langle \frac{1}{M\omega^2} \right\rangle - \mu^2$$

The first term is determined by the square of the matrix element g for the electron-phonon interaction averaged over the Fermi surface, and by the averaged inverse lattice rigidity: $\left\langle \Phi^{-1} \right\rangle = \left\langle \left(M\omega^2\right)^{-1} \right\rangle$; M is the reduced mass of lattice ions; $-\mu^2$ describes an effective Coulomb repulsion of electrons.

A direct confirmation of the electron-phonon mechanism of pairing is the isotopic effect, i.e. the dependence of T_c on M: $T_c \propto M^{-\alpha}$.

The relations (3) and (4) show that in conventional metals with typical values of N(0) and g^2 it is difficult to obtain high transition temperatures: if we take a rigid lattice with a high phonon frequency ω in (3), we obtain by (4) $\lambda \approx \left\langle \omega^{-2} \right\rangle$ that leads to low values of T_c even if we take high values of the frequency.

It is possible to try to increase T_c by increasing the value of λ by synthesising materials with a high density of states. There is however a limit for the increasing of λ since a large value in metals leads to a strong renormalization of the phonon spectrum.

The greatest success in this direction has been attained for compounds of transition metals with the A15 structure of A_3B type where A = Nb, V and B = Sn, Si, Ge… Despite great research efforts, the maximum T_c even reached was T_c~23 K, in 1973 for the compound Nb_3Ge.

Taking into account the absence of progress in studying compounds of transition metals, in 1983 Bednorz and Müller addressed their attention to another class of compound, namely the oxide compounds.

In these compounds the joint action of high polarizability of oxygen ions and poor screening of electron-ion Coulomb interaction could drive to a strong electron-phonon coupling.

Their idea was of creating oxides containing the so-called Jahn-Teller ions: such ions like Ni^{3+} or Cu^{2+} are characterised by a strong interaction of electrons with local distortion of a crystal lattice. The distortion considerably decreases the electronic energy of the ions due to a lifting of the degeneracy of electrons level; the strong interaction of electrons with displacement surrounding ions can result in the formation of polarons, whose pairing in the form of bipolarons can also lead to superconductivity.

The study of Ni ions did not give any positive result. In 1985 Bednorz and Müller turned to compounds of Cu oxides, among them La and Ba copper oxides. Varying the ratio La^{3+}:Ba^{2+} in these compounds it was easy to control the valence of Cu and the concentration of carriers.

In January 1986 they discovered superconductivity below 35 K in one of these compounds.

This discover focused the attention on these compounds and in the following months several scientists confirmed this result. Later on it became clear that the oxide superconductors of this type have a layered perovskite like structure $La_{2-x}\,M_x\,Cu\,O_4$.

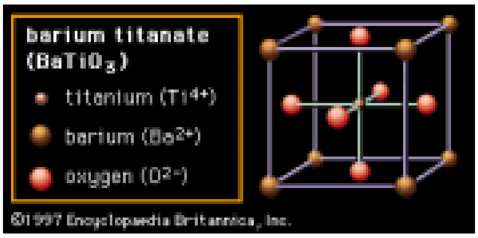

Figure 2-2. Example of perovskite like crystal.

In one year the critical temperature of the superconducting transition increases a lot compared to the value of 23 K of 1973. The T_c in the new compounds exceed the boiling point of liquid nitrogen equal to 77 K. The further active search for new compounds with higher values of T_c led to the discovery of superconductivity in the systems Bi-Sr-Ca-Cu-O and Tl-Ba-Ca-Cu-O, in which the transition temperature reached 110-120 K.

A maximum value of $T_c = 125$ K was found in the compound $Tl_2Ba_2Ca_2Cu_3O_{10}$. Even higher $T_c = 132$ K was discovered in Hg-Ba-Ca-Cu-O systems which can be further enhanced by applying external pressure. The highest reached value is $T_c = 241$ K for Bi and Hg based systems with 5-6 copper planes.

Actually there is no a theory that explains the nature of the superconducting state of these high temperature superconductors. And without a theory it is not possible to understand whether it is possible to obtain compounds with even higher T_c of the order of room temperature.

The BCS is not answering to many questions on HTS and cannot explain some "strange" physical behaviour.

It seems reasonable to ascribe to the electron-phonon interaction the pairing mechanism also in the copper oxide superconductors. Of course specific properties should be taken into account different from those of the traditional superconductors, like the strong Coulomb correlation leading among the others to strong antiferromagnetic fluctuation. This seems responsible of many anomalous properties of these oxides and has a high probability of giving a contribution to the superconducting pairing.

As a whole the synergetic pairing mechanism seems to be the most probable one in copper oxide compounds. This mechanism includes the electron-phonon interaction enhanced by charge fluctuation and the spin fluctuation interaction in the CuO_2 plane.

2.2.2 *Materials of interest*

All the new oxide compounds with high superconducting transition temperatures (T_c) can be divided into three class [10]: three dimensional compounds based on $BaBiO_3$, layered copper oxide compounds with hole conductivity (YBCO and Bi-compounds), and compounds based on Nd_2CuO_4 with electron conductivity. The most interesting one for the purpose of this work are the copper-oxide compounds.

The new oxide compounds possess many properties in common with conventional superconductors. At the same time the high-temperature superconductors have a number of physical properties by which they essentially differ from conventional metals.

In the copper-oxide superconductors, the main role is played by CuO_2 planes, which are separated by layers of other ions. As a result, a high anisotropy of the electronic and, in particular, superconducting properties, which are of quasi-two-dimensional characters, are typical of the cooper-oxide superconductors. The physical properties of the oxide compounds are strongly influenced by the deficit with respect to the oxygen and certain variations in their composition.

Studies of the thermodynamical properties of copper-oxide superconductors have shown a number of peculiarities in the temperature dependence of critical magnetic fields and specific heat. The existence of the strong anisotropy of electronic properties results in a large anisotropy of critical magnetic fields in the *a-b* plane and in the direction *c* perpendicular to this plane. The *a-b* plane is the plane of the transport direction, while the *c* axis is perpendicular to the current flow direction (see Figure 2-4).

Among many oxide superconductive materials, the most used for the purpose of wires and conductors, and in the particular for the current leads application, are: YBCO 123 (Y-Ba-Cu-O system), BSCCO 2212 and BSCCO 2223 (Ba-Sr-Ca-Cu-O systems). There were also other kind of Bi-compound doped with Pb or Tl, but are experimental one and not yet useful for an industrial application.

These materials have anisotropic structures and their grains must be aligned to obtain a high critical current density, which is the key in applications. The *critical current density* (J_c), is the maximum electrical current density that can be regarded as flowing without resistance through a superconductor.

Until now, bismuth-based compounds have revealed a tendency to show strong alignment when mechanically deformed (Bi-2223 compound) or cooled from a molten state (Bi-2212 compound).

This strong alignment in *a-b* plane eliminates weak links and the history effect disappears. The Bi-compounds show strong-coupled characteristics and have less severe weak link problems even if the materials have *a-b* tilt grain boundaries in a *c*-axis textured structure. Compared with Bi-compounds, the YBCO compounds show severe weak link problems when we have misoriented *a-b* tilt grain boundaries even in highly *c*-axis textured film.

The bismuth compound has another advantage for wire fabrication, that is a lower melting temperature than silver: YBCO has a higher melting temperature than silver and this makes it difficult for use in a melt texturing process with silver-sheathes or substrate. Another point in favour of Bi-compounds is its weak oxygen deficient problem. In addition to this, raw materials for Bi-compounds (with the exception of Bi-Th compounds) do not need rare earth elements and the Bi-2223 compounds show the highest critical temperature, 110 K. As regards the Bi-thallium compounds, they show higher critical temperature, but they have severe toxic problem and so it is not easy to work with them. Thus Bi-2223 is today considered to be one of the best candidates for long wire fabrication. Even if actually, important efforts are put in the fabrication of YBCO wires.

For the ceramic HTS materials to be commercially useful in high field magnets, energy storage devices, motor/generators and power transmission cables they need to be shaped into composite multifilamentary wires or ribbons containing both the superconductor and a metal. Such a composite geometry is desirable for several important reasons:

- parallel electrical path serves as a bypass in case of local failure in HTS;
- heat sinking;
- minimal loss of energy by magnetic flux motion;
- ac loss reduction;
- mechanical protection of the brittle superconductor core against Lorentz force and stresses during handling;
- protection from atmospheric environment to avoid oxidation which would change the non stoichiometric content of oxygen.

In the next section several processing techniques are reported for the common high temperature superconductors: YBCO-123, Bi-2212 and Bi-2223.

2.3 YBCO 123

This is the first discovered oxide high temperature superconductor with a critical temperature above that of liquid nitrogen.

$YBa_2Cu_3O_{7-x}$ (YBCO) was discovered in 1987 by Wu's team, and it has a T_c of 92 K. The original compound is observed in two modifications: the first one is the orthorhombic phase; the second is the tetragonal phase.

The latter is observed at low temperature, while the last at temperature > 500 ºC. It is seen that YBCO has a typical layered perovskite-like structure with two CuO_2 planes separated by a layer of Y ions which are bounded by the layers Ba-O4, Cu1-O1 and Ba-O4. The oxygen O2 and O3 are strongly coupled with Cu2 in the CuO_2 planes, unlike the weakly coupled oxygen O1 in the Cu1-O1 chains. It is also seen that the physical properties of YBCO depend considerably on oxygen content: there are differences between the orthorhombic and the tetragonal phase.

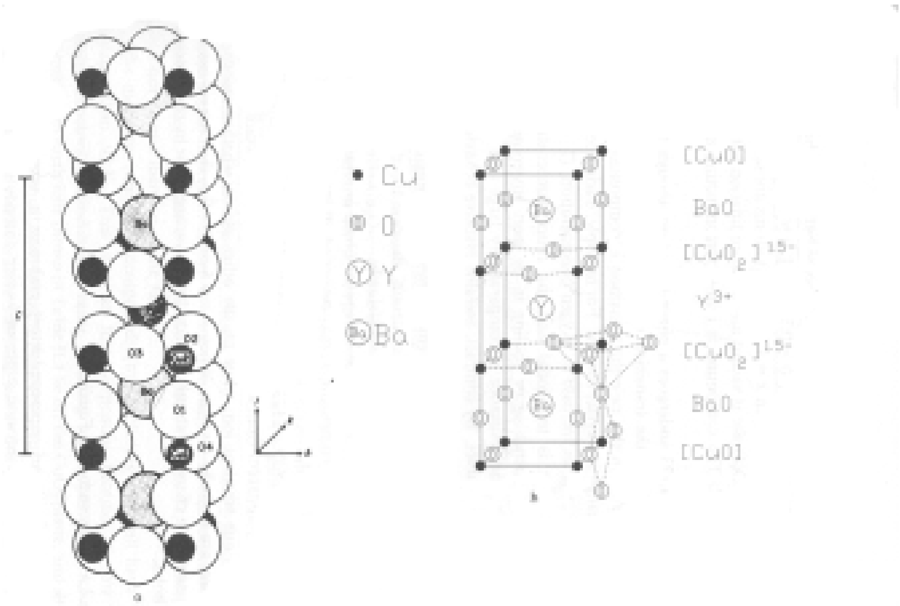

Figure 2-3. YBCO crystal structure.

The most diffused methods to synthesize this compound are the melting processes: melt texturing, epitaxial growth and liquid phase processing. The so-called ‘powder in tube’ technique is not used because of the poor performances of the specimen obtained by this way.

The continuous development of new technique is an attempt to reach higher performances.

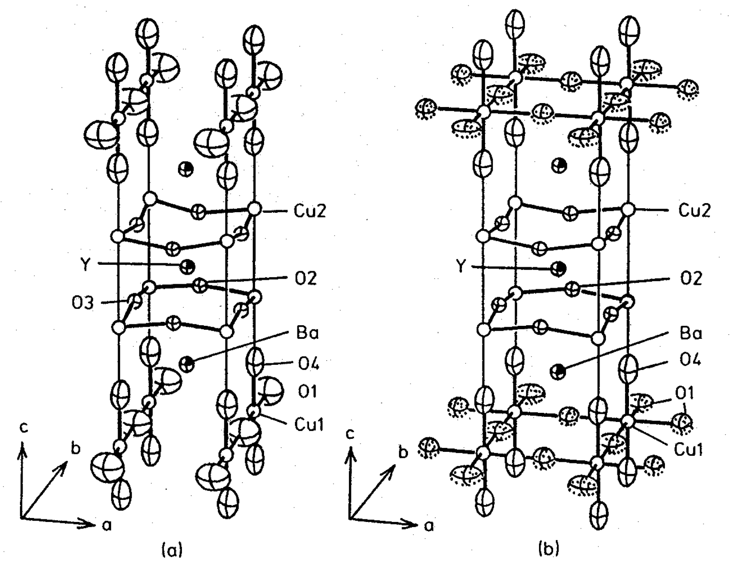

Figure 2-4. Orthorhombic and tetragonal phase for YBCO.

Among the above mentioned approaches, the most simple is the melt cast process (MC).

2.3.1 *Melt processing*

Higher critical current density could be achieved by melt processing YBCO [11]. In air the YBCO phase diagram shows a peritectic point at about 1010 °C where Y_2BaCuO_5 (the green phase) and $Yba_2Cu_3O_{7-x}$ coexist.

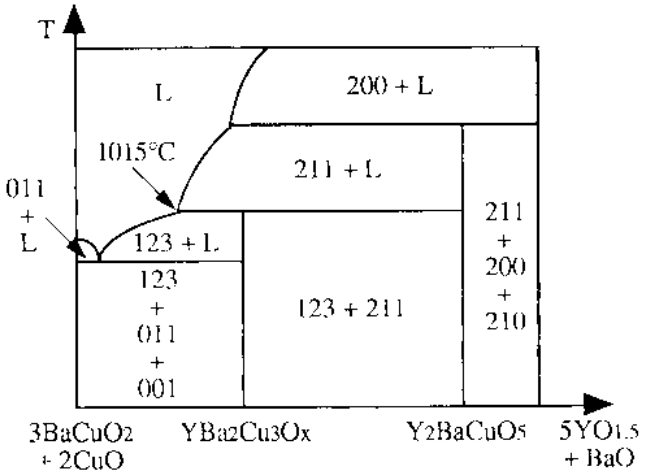

Figure 2-5. Phase diagram of YBCO.

Using different processing routes through this phase diagram, large-grained specimens with high intragrain critical current densities could be produced by applying partial melting of the samples.

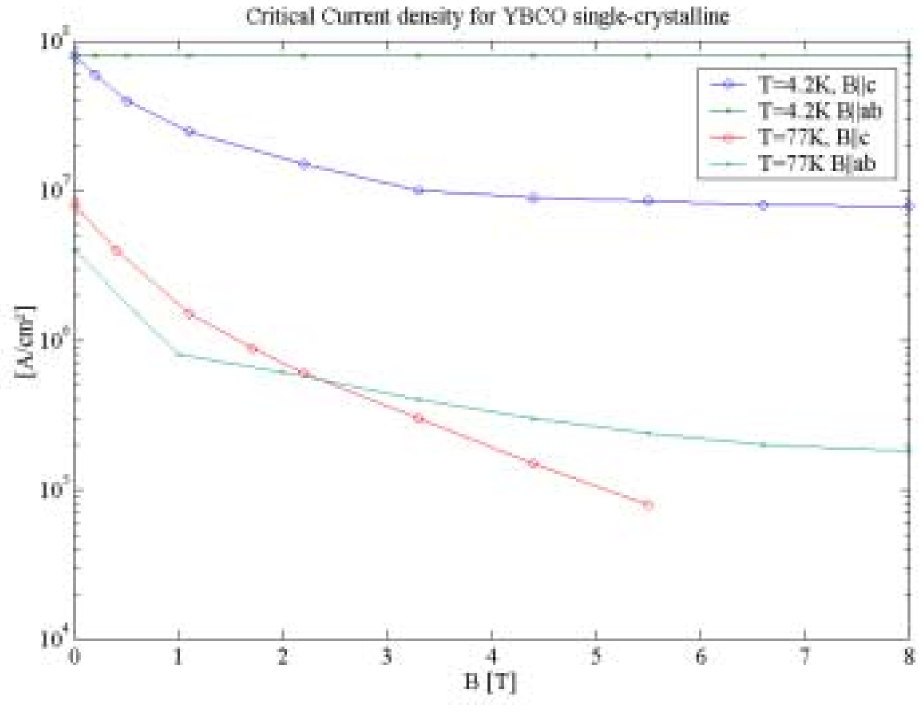

Figure 2-6. Behaviour of Jc due to the different orientation of the magnetic field [11].

All these techniques suffer from the fact that these grain boundaries also act as a weak link. Therefore only specimen sizes up to few centimetres in length can carry high current densities. Although useless in other areas as applications for superconducting wires, they will be applied in other areas such as the magnetic shielding technology.

In Figure 2-6 is reported the influence on J_c of the orientation of the applied magnetic field.

In order to improve the critical current densities in polycrystalline material, especially in the presence of a magnetic field, texture is required. Some variants of the melt processing, called *melt texturing*, have been developed to achieve it: the most important of these are the liquid phase processing (LPP), the melt texture growth (MTG), the powder melting process (PMP) and the liquid zone melting (LZM).

Melt texturing of the 123 compound results in a superconductor with a layered microstructure of thin YBCO plates stacked in the *c*-direction. All melt texturing techniques involve the melting of 123 above its peritectic temperature, T_p.

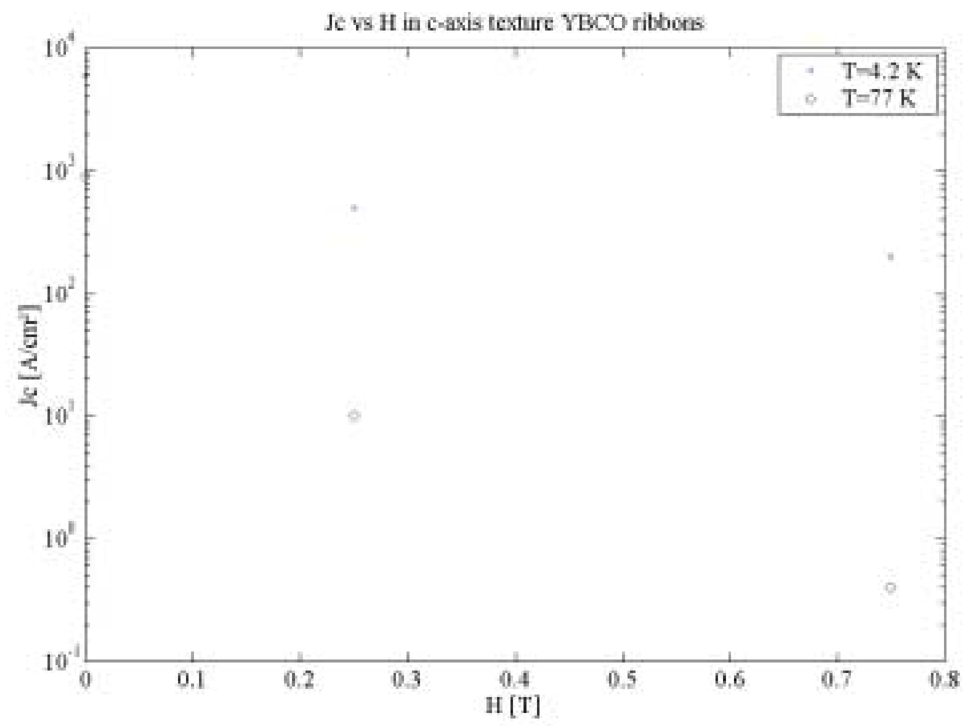

Figure 2-7. Critical current density in function of the applied magnetic field [8].

When heated above T_p, 123 incongruently melts into a solid and a liquid phase according to the reactions:

123 → 211 + liquid 1015 ºC < T < 1300 ºC

211 + liquid → Y_2O_3 + liquid 1300 ºC < T < 1500 ºC

As a function of the cooling rate specimens with different characteristics can be obtained. If any temperature gradient is imposed or if the conditions are favourable for multiple-nucleation of 123 even in presence of a thermal gradient, the sample would contain centimetre-sized domains of well-aligned grains with arbitrary orientations with respect the sample axis. These samples are extremely useful not only for investigating basic pinning mechanism in high J_c bulk materials, but also for several applications, especially magnetic bearings where a long-range grain alignment is not crucial. For high current-carrying applications, however, a uniform grain alignment over long lengths is essential. Directional solidification of 123 with specimen transport under a prescribed temperature profile has the potential of producing textured 123 that is aligned along the specimen axis over long length. In these methods it is crucial the fixed cooling rate on each cooling step.

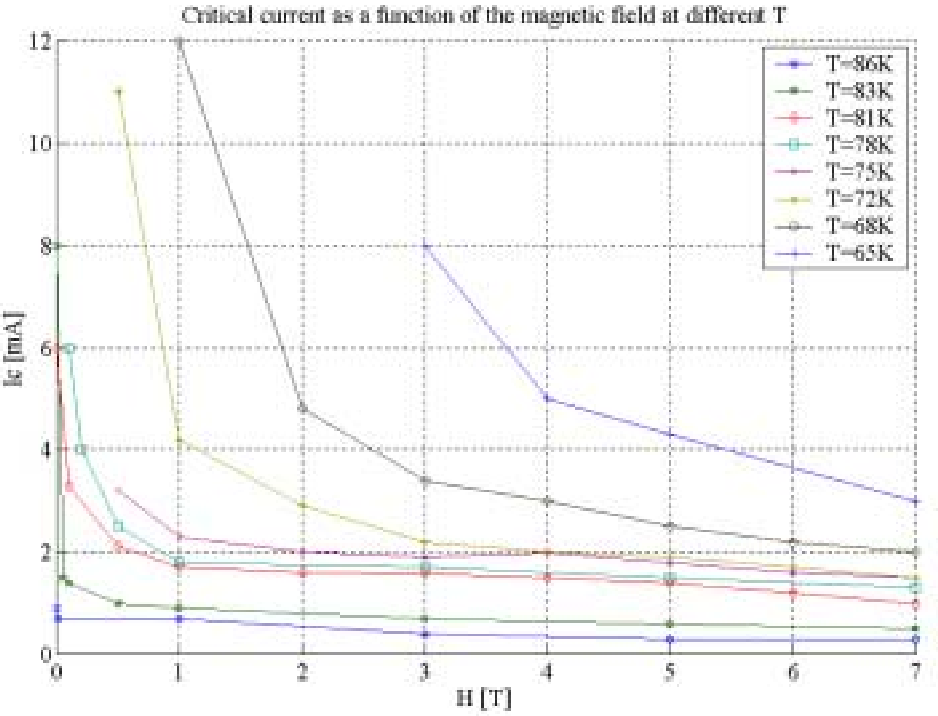

Figure 2-8. Influence of T on Ic transport [13]. The measures summarised here are performed on pellets of 6 mm in diameter and 1 mm in thickness and the results were not referred to the cross section of the samples.

A new promising technique, following this procedure, is the liquid phase processing [12]. According to this procedure, after some annealing steps and slow cooling at a fixed rate it is possible to control the microstructure of the superconductor. Doing so it will be possible to achieve better performance as regards the critical current density. Values of 15000 A/cm² at 77 K were obtained for specimen treated with this process and in absence of applied magnetic fields. Common values for the critical current density are reported in Figure 2-7 and Figure 2-8 .

The critical current density reported is referred to the *engineering* current density, i.e. evaluated over all the specimen cross section. Hereinafter I will refer to this engineering J_c, unless differently said.

2.4 BSCCO 2212

The Bi-compound superconductors were discovered in 1988 by Maeda, Von Schnering et al. showing a T_c up to 110 K.

BSCCO 2212 is the commercial name for the $Bi_2Sr_2Ca_1Cu_2O_{8+x}$ compound.

The Bi-based compounds can have various numbers of copper-oxygen planes and are described by the general formula $A_2Ca_{n-1}B_2Cu_nO_{2n+4}$ where A = Bi or Tl and B = Sr or Ba. The transition temperature also depends on the number of the copper-oxygen planes and takes the values 10, 85 and 110 K for the Bi compounds.

The most diffused techniques in order to obtain a high performance superconductor of BSCCO 2212 are the following:

- Powder in tube technique (PIT)
- Melt Cast process (MC)
- Dip Coated (DC)

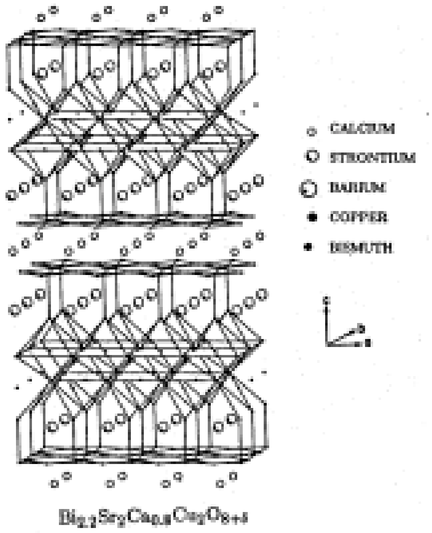

Figure 2-9. BSCCO crystal structure.

2.4.1 Powder in tube

The powder is prepared by a standard mixed oxide procedure [14]. Appropriate amounts of high-purity Bi_2O_3, $SrCO_3$, CaCO and CuO are thoroughly mixed and calcinated in three steps in the temperature range 800-850 ºC. After each calcination step the powder is ground to ensure optimum homogeneity. The remaining carbon content is between 120 and 150 ppmw.

Finally the powder is filled into a Ag tube typically of 8 mm outer and 6 mm inner diameter and subsequently the whole composite is drawn to the final diameter of 1.5 mm. Then specimens are subjected to a final annealing procedure at temperatures above 800 ºC in order to optimise superconducting properties of the $Bi_2Sr_2Ca_1Cu_2O_{8+x}$ phase.

By stacking together several pieces of monofilamentary [15] wire and putting them into a silver tube, we can obtain a composite structure that, once processed by drawing, produces up to 50 m of multifilamentary wire 1.3 mm in diameter.

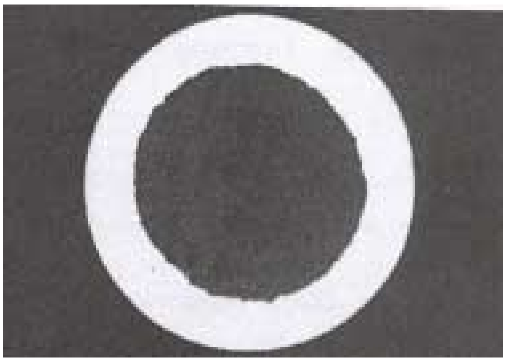

Figure 2-10. Cross-section of monofilamentary BSCCO 2212 wire.

Otherwise it is also possible to roll the wire until a tape is processed in lengths of about 800 m.

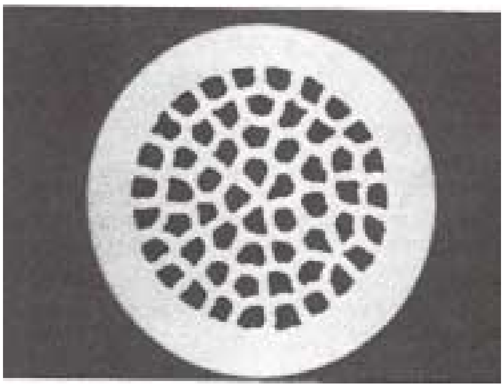

Figure 2-11. Cross-section of multifilamentary BSCCO 2212 wire.

Electrical measurements performed at 77 K on straight monofilamentary wire samples, gave a T_c value of about 88 K and a J_c of about 500 A/cm² at zero field. At 4.2 K J_c in self-field results to be higher than 2 10^4 A/cm², dropping to less than 1000 A/cm² by increasing the filed by a few Tesla [15].

As regards the multifilamentary typical values are: at 77 K, J_c higher than 1000 A/cm² in self-field; at 4.2 K, J_c of up to 40000 A/cm² in self-filed.

Mechanical stresses are dangerous for these materials, for example, for wound samples, 1 m in length, a J_c degradation of about 50% was systematically observed in this study [15].

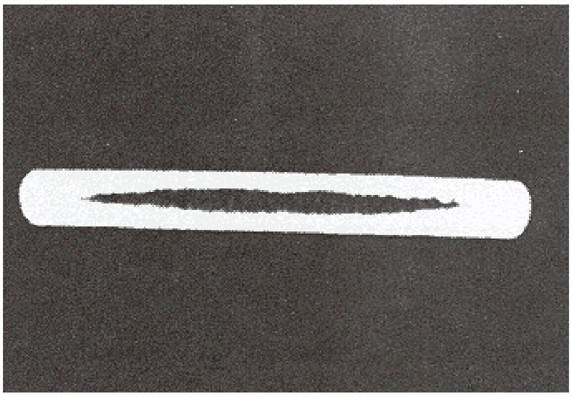

Figure 2-12. Cross-section of BSCCO 2212 monofilamentary tape 0.3 mm in thickness.

Short samples of tape (0.3 mm thickness) gave J_c at 77 K of about 1000 A/cm² at zero filed. The behaviour of Bi2212 as a function of the magnetic filed at 77 K is reported in Figure 2-13. At 4.2 K, J_c of up to 60000 A/cm² was measured.

Coils prepared with the rolled tape showed a J_c degradation of about 40%.

For high current application BSCCO 2212 tapes with higher performances were made [8,11].

The behaviour of J_c for these tapes as a function of the magnetic field at 4.2 K is reported in Figure 2-14. The J_c at 77 K is reported in Figure 2-13.

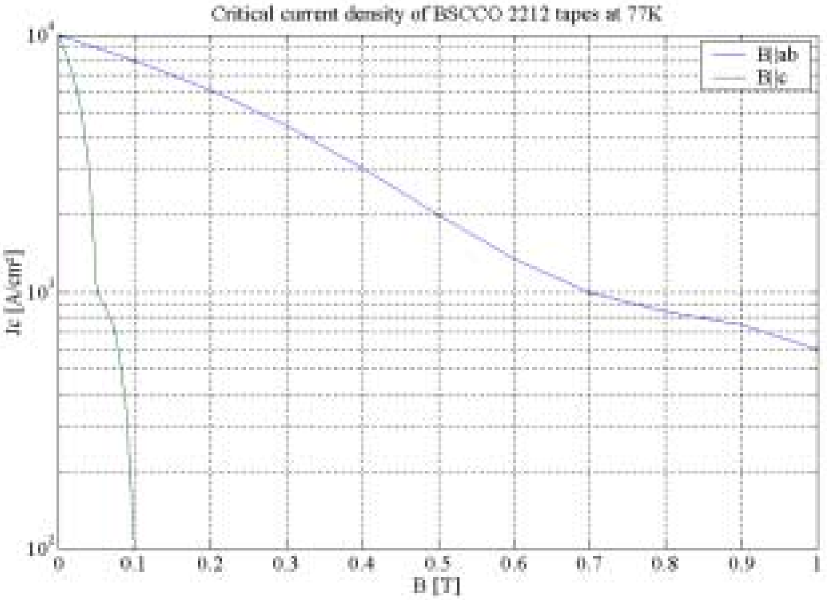

Figure 2-13. Critical current density of BSCCO2212 at 77K in function of the magnetic field [11].

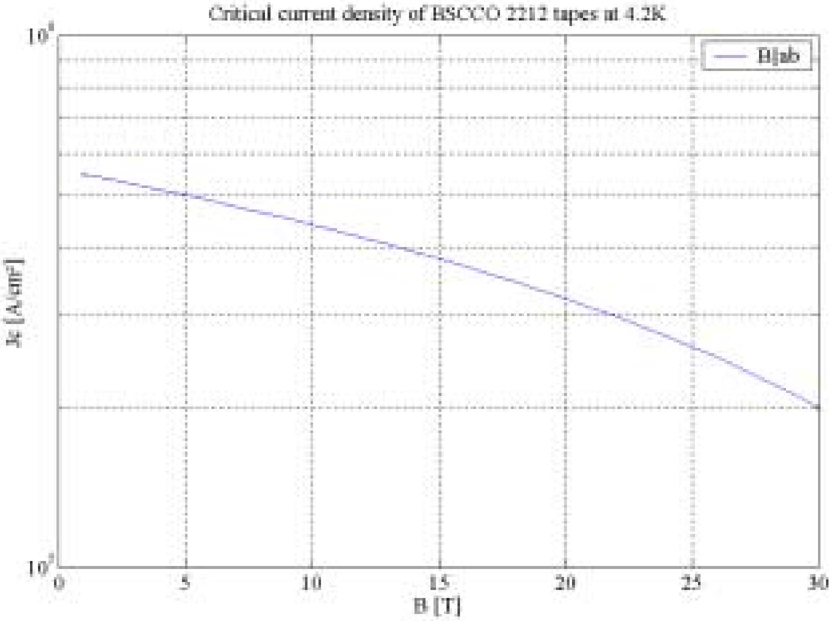

Figure 2-14. Critical current density of BSCCO2212 at 4.2K in function of magnetic field [8].

2.4.2 Melt cast process

According to this procedure [16] the starting materials (Bi_2O_3 5N; $SrCO_3$ 2N5; CaO 3N; CuO 5N) are mixed together, with a metal ratio near 2:2:1:2, calcined, then mixed with $SrSO_4$ and melted between 1000 ºC and 1200 ºC. The obtained homogeneous melt is poured into moulds, either rotating or static, where a solidification and slow cooling to room temperature occurs. The obtained melt cast bodies, consisting of a more or less coarse grained heterogeneous material with a lack of oxygen compared to the starting mixture, are already in the shapes desired for the later applications. The material, after having been removed from the mould is subjected to an annealing procedure between 750 ºC and 850 ºC in order to reach the 2-layer phase and to adjust its oxygen content. The heating conditions such as temperature, duration and gas atmosphere depend on the dimension of the individual form part. The electrical properties of the superconducting bulk parts are moreover influenced by the preparation of the raw material (calcination style), the amount of $SrSO_4$, the melting conditions and a pre- or post heating of the mould.

It is also possible to fabricate hollow forms by using a centrifugal technique: i.e. casting the hot melt into rotating moulds where the melt is evenly distributed on the inner side wall, due to the centrifugal force. The solidifying melt shrinks away from the mould walls and leaves an air gap resulting in a clattering of the ceramic cylinder. To prevent the cylinder from shattering the rotation speed must be tuned during the different stages of the solidification process.

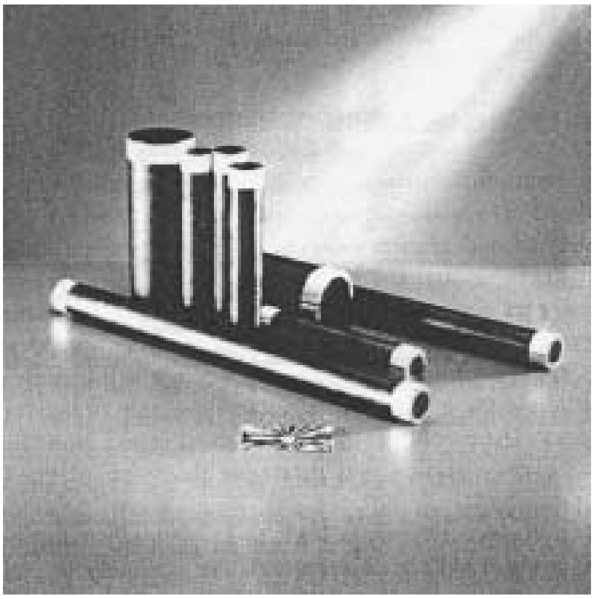

Figure 2-15. Hollow bulk material made of BSCCO 2212.

The electrical contacts are usually inserted into the moulds before casting the melt material and are embedded in the cast material. The partial melt during the annealing step is responsible for an interaction between silver and BSCCO leading to current contacts with good mechanical and electrical performance.

Typical performance of specimen obtained following this procedure is, in zero field and at 77 K, a maximum J_c of about 4250 A/cm² [17].

2.4.3 Dip coating

Dip-coating [18] is performed by drawing 5 mm wide by 25 or 50 micron thick silver tapes up to five meters in length through slurries of BSCCO-2212 powder. The powders are manufactured by aerosol or spray pyrolysis methods. Several combinations of binder, dispersant and carrier fluid were explored. Samples are reacted using various time/temperature cycles.

Tests performed on specimens obtained using this technique have shown critical current densities ranging from 1100 to 2700 A/cm².

In comparison with the PIT technique, with to this method it is more difficult to obtain low contact resistance because the electrical contacts are to be made on the ceramics instead of on the silver sheath.

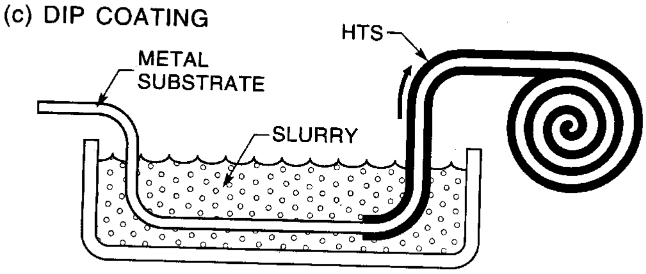

Figure 2-16. Dip coating process.

2.5 BSCCO 2223

BSCCO 2223 is the commercial name for the $Bi_2Sr_2Ca_2Cu_3O_{10}$ superconducting compound.

Its critical temperature is about of 110 K. This is, at the present, the most promising high temperature superconductor because of the relatively high transition temperature and the fact that pinning properties at T>10 K are superior to those of Bi-2212. The critical current densities achieved are of the order of some 10^4 A/cm² at 77 K and 0 T, with a moderate magnetic field dependence of J_c up to magnetic fields of a few Tesla.

The most diffused technique in order to produce Bi-2223 is undoubtedly the ‘powder in tube’ method.

2.5.1 Powder in tube

A schematic of the 'powder in tube' [19] process used for fabricating Ag sheathed Bi-2223 wires and tapes is shown in Figure 2-17. The process is the same of the one described for the Bi-2212 except for the different raw materials and for the different annealing step.

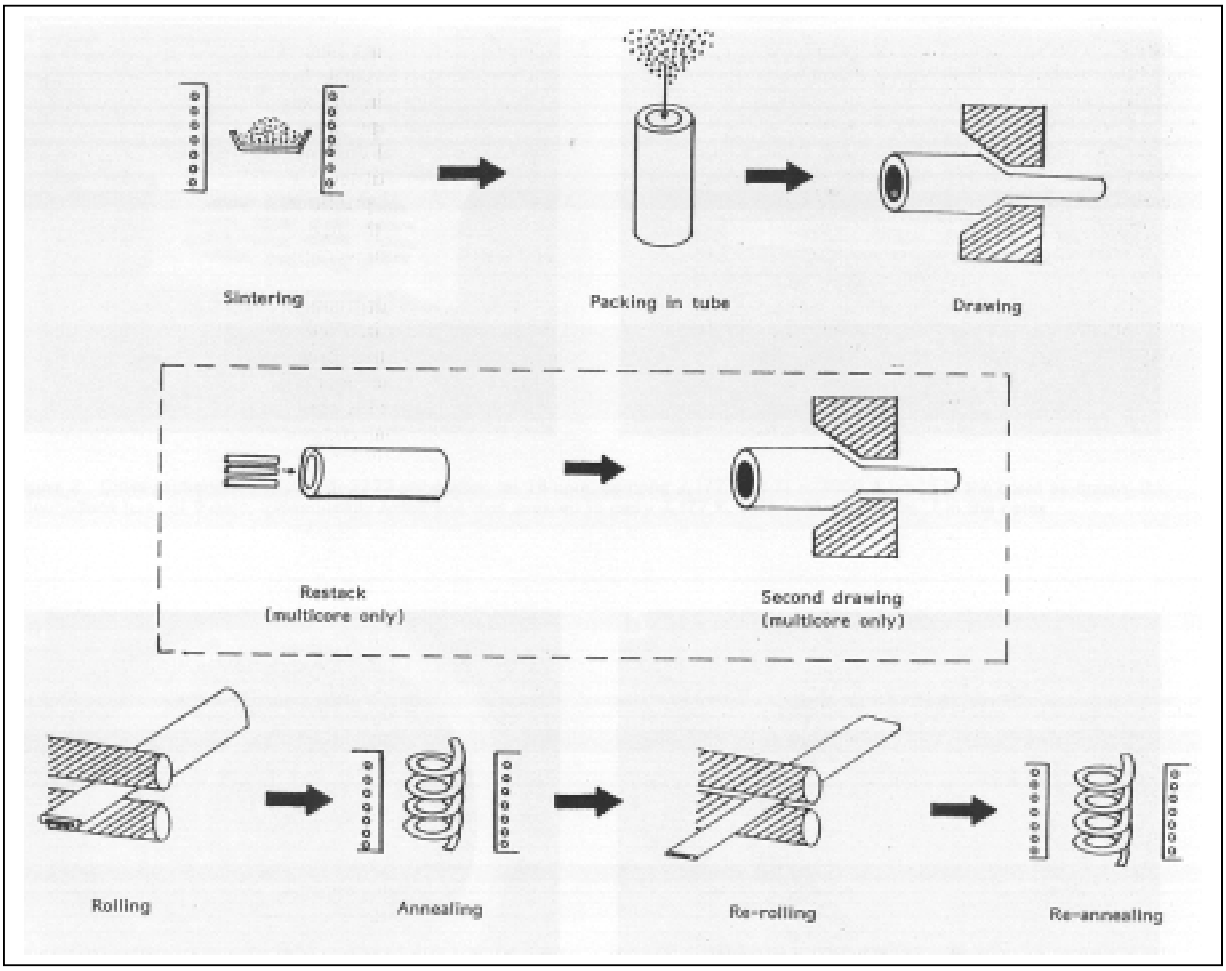

Figure 2-17. PIT process diagram.

Precursor powder optimized for the high T_c phase is usually prepared from the >99.9 % purity Bi_2O_3, PbO, $SrCO_3$, CaO or $CaCO_3$ and CuO with cation ratios, respectively, in the vicinity of 1.8, 0.4, 2.0, 2.2 and 3.0. To achieve a homogeneous mixture of the precursor powder, sintering and grinding are repeated from 1 to 5 times. Typical heat treatment schedule includes temperatures between 800 and 870 ºC and time duration of 24 – 100 h. The annealing conditions needed to obtain the highest J_c values in each type of tape are different. J_c values of 1.9 and 1.6 10^4 A/cm² at 77 K are found in tapes from SS (solid state reaction method) and PL (Polymer matrix method) powder respectively. The powder is then packed into silver tubes. To ensure complete filling of the tube space, the powder is introduced gradually with mechanical agitation.

In multifilamentary tapes, the most common and useful in order to ensure high current transport, differences are seen due to the number of filament (N) packed in the silver tube [20]. The results obtained are shown on Table 2-1.

Table 2-1

N	d (mm)	S_{eff} (%)	J_c (A/cm^2)	J_{eff} (A/cm^2)	$\langle S_f \rangle$ (mm^2)
8	0.34	8.05	1230	63	0.0053
16	0.35	7.44	1420	106	0.0025
24	0.35	8.29	3400	282	0.0019
32	0.35	7.42	2980	221	0.0013
288	0.75	1.84	100	20	0.00015

N is the number of filaments; δ is the tape thickness in mm; S_{eff} is the effective superconducting cross section given by $S_{eff} = S_{HTS} / S_{total}$; here J_c is the critical current density at zero external field; J_{eff} is the effective critical current (critical intensity divided by total cross section) and $\langle S_f \rangle$ is the average cross-section of each filament.

It is evident that upon decreasing the average cross section for the filaments ($\langle S_f \rangle$) there is an increase in the J_c. It is due to the increasing surface volume ratio. Upon decreasing $\langle S_f \rangle$, however, there is an increase of the ratio of the mean square deviations $DS_f = \langle (S_f - \langle S_f \rangle)^2 \rangle^{1/2}$ versus $\langle S_f \rangle$ (this phenomenon is called sausaging). The smaller section along a filament ($S_{f,min}$) determines I_c, but as $S_{f,min} \approx (\langle S_f \rangle - DS_f)$ sausaging decreases the measured J_c.

The dependency of J_c on d (and consequently d_f) has also been studied in *N*=24 rolled tapes. The tests demonstrates that under d_f = 10 mm the sausaging or the inhomogeneities along the tape limit the J_c value.

The result is an optimized value for *N* of 24. Sausaging is the main limit to the J_c values, however, at least for filamentary down to 10 mm in thickness.

Best values for the critical current densities of a silver sheathed Bi-2223 are: at 77.3 K 53700 A/cm^2 in zero magnetic field, 42300 A/cm^2 at 0.1 T and 12000 A/cm^2 at 1 T.

Most common values are shown in Figure 2-18.

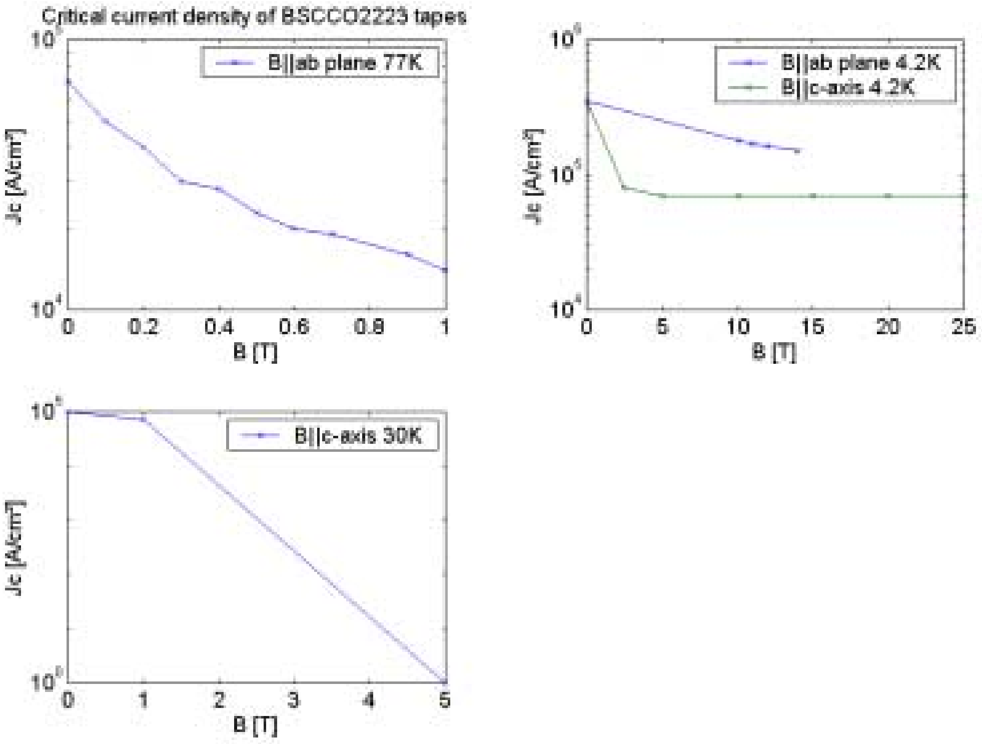

Figure 2-18. Critical current density of BSCCO2223 in function of the applied magnetic field [11].

3 Characterization

In the previous chapter the attention was focused on three different types of HTS materials which are the most promising to the purpose of the design of current leads.

Among these conductors, oxide superconducting tapes (BSCCO) sheathed with pure silver have several advantages: high J_c characteristic, thanks to a better crystal orientation in the superconducting core; mechanical flexibility and the thermal stability. Between BSCCO 2212 and 2223 the second one seems to be preferable due to the high performances as regard the current density and the low sensitivity to the magnetic field. However the high thermal conductivity of pure Ag sheath, creates a high heat load into the cryogenic system.

A way to reduce thermal conductivity of metals is by alloying. As silver is generally congenial to oxide superconductors the choice is between the two most common silver alloys: Ag-Au or Ag-Cu alloys.

The second one presents a rather steady behaviour of the thermal conductivity upon increasing the content of Cu, furthermore this alloy reacts with the Bi-based superconductors and causes degradation of the superconducting characteristics. In the Ag-Au alloy, instead, the thermal conductivity drastically decreases with an increase in Au content and, above all, it does not react with the oxide.

Thus, in the following sections the attention will be pointed on this kind on superconductors: BSCCO 2223 Ag-Au sheathed.

3.1 Critical current measurement

The critical current density J_c is an important parameter for characterising a superconductor: it is a measure of the conductor's current carrying capacity.

J_c varies for different materials and, depending on the manufacturing process, it varies for different conductors made from the same material.

Strictly speaking J_c is not measured: rather it is calculated from the critical current, I_c, by dividing it by the specimen's cross-section.

In the preferred method for measuring I_c, a direct current is applied to the superconductor while the voltage across a given length it is measured.

I_c can be defined as the *maximum current that a superconductor can carry at a particular temperature and applied magnetic field with zero resistance*. The detection of the normal-superconducting transition is made measuring the voltage drop across the sample. Due to the difficulty to measure an infinitesimally small voltage or a fainting resistivity the way to detect it, is to introduce an I_c criterion. There are two possible choices:

- an electric field criterion;
- a resistivity criterion.

Both criterions are based on the measurement of a finite voltage across the test specimen. The electric field criterion defines I_c as the current where the electric field strength equals a selected value, E_c; the resistivity criterion defines I_c as the current where the resistivity of the test specimen equals a selected value, ρ_c. Typical values for the HTS of E_c and ρ_c are 0.1 μV/cm and 10^{-12} Ω cm, respectively [22].

The electric field strength E and the electrical resistivity ρ, are related to each other by the current density:

$$(5) \qquad \begin{gathered} E=\frac{V}{L}; \quad J=\frac{I}{S}; \quad \rho=\frac{VS}{IL} \\ J=\frac{I}{S}=\frac{VIL}{LVS}=\frac{E}{\rho} \rightarrow \quad J=\frac{E}{\rho} \end{gathered}$$

where V is the voltage drop, I the flowing current; S the cross sectional area and L the specimen’s length.

The superconductor’s Voltage-Current (V-I) characteristic is determined by recording the voltage as the current is increased. Typically it is measured at a selected temperature, in liquid helium or liquid nitrogen, and over an appropriate range of applied magnetic field. The V-I characteristic can be usually approximated by the empirical equation:

$$(6) \qquad V=V_0\left(\frac{I}{I_0}\right)^n$$

where I_0 is a reference current at a voltage V_0 and n is the empirical parameter that reflects the shape of the V-I curve. It indicates the abruptness of the transition from the superconducting to the normal state. Typical values of n range from 10 to 60 for commercial high temperature superconductors. In the LTS n is larger (more than 100) because the transition from the superconducting to normal state is more rapid: the slope of the V-I curve is steep.

Those measures present a number of measurement problems we have to solve in order to obtain realistic data.

3.1.1 Interfering voltages

There are numerous sources of interfering voltages that can complicate the I_c measurement due to the low voltage implied in those tests. Although they cannot be eliminated, in many cases they can be reduced to acceptable levels if their sources can be isolated. The most common sources of interfering voltages are:

1. voltages induced in the loop formed by the test specimen and the voltage sensing leads. They can be eliminated by twisting and shielding the sensing leads. Moreover is necessary to avoid any relative motion between the test specimen and the magnetic field. Changes in the current level may also interfere;
2. Hall effect according to which a transverse electric field develops in a solid material when it carries an electric current and is placed in a magnetic field. This source can be eliminated by simply placing the connection points of the voltage sensing lead on a line that is parallel to the longitudinal axis of the specimen;
3. thermoelectric voltages due to increasing temperature of the voltage sensing region and temperature gradient along the specimen;
4. thermoelectric voltages generated at points in the voltage sensing circuit that are outside the cryogen bath;
5. other interfering voltages come from ground loops and common mode: both involving bad ground circuits on the test apparatus;
6. convoluted voltage: those voltages occur when the current path is not parallel to the conductor’s longitudinal axis. This leads to an electric field distortion that can, in its turn, cause anomalous voltages.

Designing a test apparatus one has to take into account those sources of interference in order to obtain good measurements from the tests.

3.1.2 *Specimen damage*

The oxide superconducting materials are mechanically fragile and it is easy to damage them by bad handling lessening or compromising their performances.

The chemical reactions between the specimen and soldering flux or water in the atmosphere can seriously degrade the conductor's I_c. It is necessary to be careful while soldering the electrical contacts to the specimen. In presence of bad contact resistance the joule heating can cause thermal runaway or quench compromising the functionality of the superconductor.

Being the oxide superconductors extremely susceptible to mechanical damage, the assembly of the experimental apparatus has to be done carefully. Mechanical stresses can compromise the capabilities of the conductor: bending, torsion etc. are to be avoided. Another source of mechanical stress is the low coefficient of thermal expansion of the oxide that can lead to a different elongation between the specimen and the support introducing a mechanical stress that could result in inferior performances. In presence of an external magnetic field also the Lorentz's force is to be taken into account since it also produces stresses on the sample.

3.1.3 *Magnetic field considerations*

The high temperature superconductors, working at rather high temperature (like 77 K), have demonstrated a high sensitivity to magnetic fields even if of few mT. The presence of external magnetic field influences J_c, but also the orientation of the field interferes with the J_c evaluation. The HTS are anisotropic materials and have a different (J_C, B) curve according to the direction of the external magnetic field. Performing a current test, the presence and orientation of an external magnetic field has to be taken into account.

3.1.4 *Current tests*

The critical current tests have been performed on BSCCO 2223 tapes made by different manufacturers.

The specimens are numbered according to their manufacturer and I tested 2 samples of each type in order to have comparable data about their performance. In the table are summarised the properties of the tapes measured.

Table 3-1.

Manufacturer	Description
BICC	3.4 mm x 0.3 mm tape. 4% at. AgAu
NST Zerome Gold	3.4 mm x 0.3 mm tape. 4% at. Au
Russian tape	3 mm x 0.3 mm tape. 10% at. Au
Russian tape	3 mm x 0.3 mm tape. 1% at. Au

The tapes have been soldered on a copper contact pad and then placed on an insulating support in order to avoid any mechanical stress on the superconductor.

The test is performed in a liquid nitrogen bath (77 K) in order to keep constant the temperature of the sample.

The set-up is sketched in Figure 3-1.

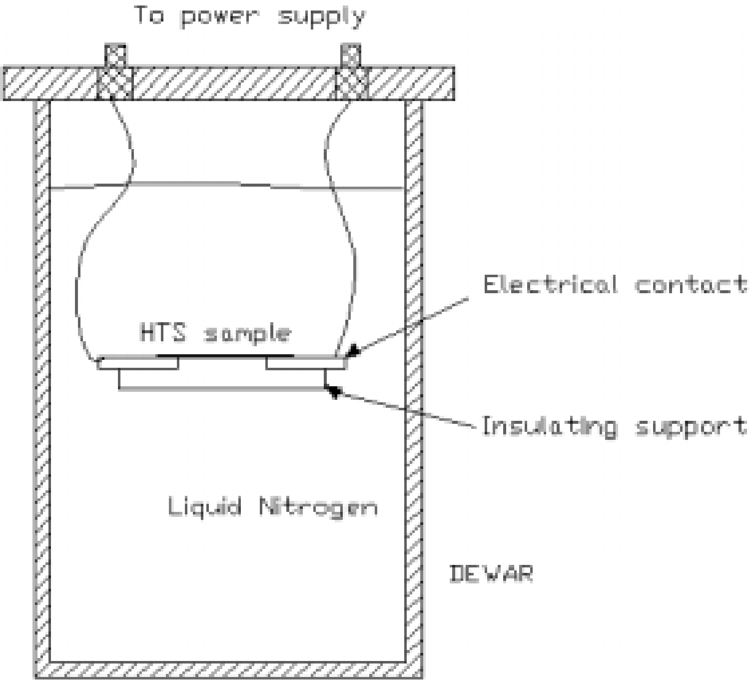

Figure 3-1. Cryogenic apparatus.

The specimen is equipped with four voltage taps in order to measure the voltage drop across the tape and the two contact resistances of the junction between copper and the superconductor.

In order to avoid local thermal stresses during the soldering procedure, the sample was warmed up to 180 ºC at both ends and then soldered on the copper plate with indium. After soldering it is necessary to wipe out the flux used to sold silver and indium to avoid dangerous chemical reaction of corrosion on the tape. The voltage taps are placed according to the scheme in Figure 3-2.

The distance between the voltage taps is around 5 cm. Using an electric criterion of 1μV/cm, the voltage drop limit is then set to 5 μV.

An acceptable value for the contact resistance has been set equal to 1 μΩ. The dimensioning of the copper pad is then made according to this limit.

The material properties at 77 K are:

$$\rho_{Cu} = 1.9\ 10^{-9}\ \Omega\mathrm{m}$$
$$\rho_{AgAu} = 1.0\ 10^{-8}\ \Omega\mathrm{m}$$
$$\rho_{In} = 9.0\ 10^{-8}\ \Omega\mathrm{m}$$

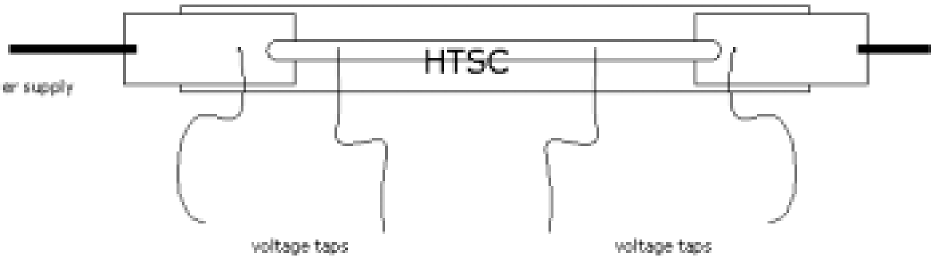

Figure 3-2. Voltage tap's layout.

The maximum allowed current density for the copper wires is set to 4 A/mm². With a current flowing of 50 A:

$$J \le 4\frac{\mathrm{A}}{\mathrm{mm}^2} \Rightarrow 4 = \frac{50}{\mathrm{x}} \Rightarrow \mathrm{x} \ge 12.5\,\mathrm{mm}^2\ \text{wire section}$$

Now it is necessary to evaluate the length of contact required for low resistance joints. The highest resistivity is that of indium.

$$R = \rho\frac{l}{S}$$
$$S = \rho\frac{l}{R}$$
$$S = a \times b \Rightarrow \mathrm{b} = \frac{\mathrm{S}}{a}$$

l is the thickness of the soldering; *S* is the soldering area; *a* the width of the tape and *b* the soldering length to be evaluated.

Assuming for *a* the value of 3 mm and for *l* the value of 0.1 mm, using the imposed limit for the R:

$$S = 9e-8 * \frac{0.1e-3}{0.1e-6} = 9e-5 \text{ m}^2$$

$$b = \frac{9e-5}{3e-3} = 30 \text{ mm}$$

As regard the copper pad in order to reduce to the minimum the heating due to the Joule effect a cross section ten times the one of the leads is good.

The final shape of the test device is reported in Figure 3-3.

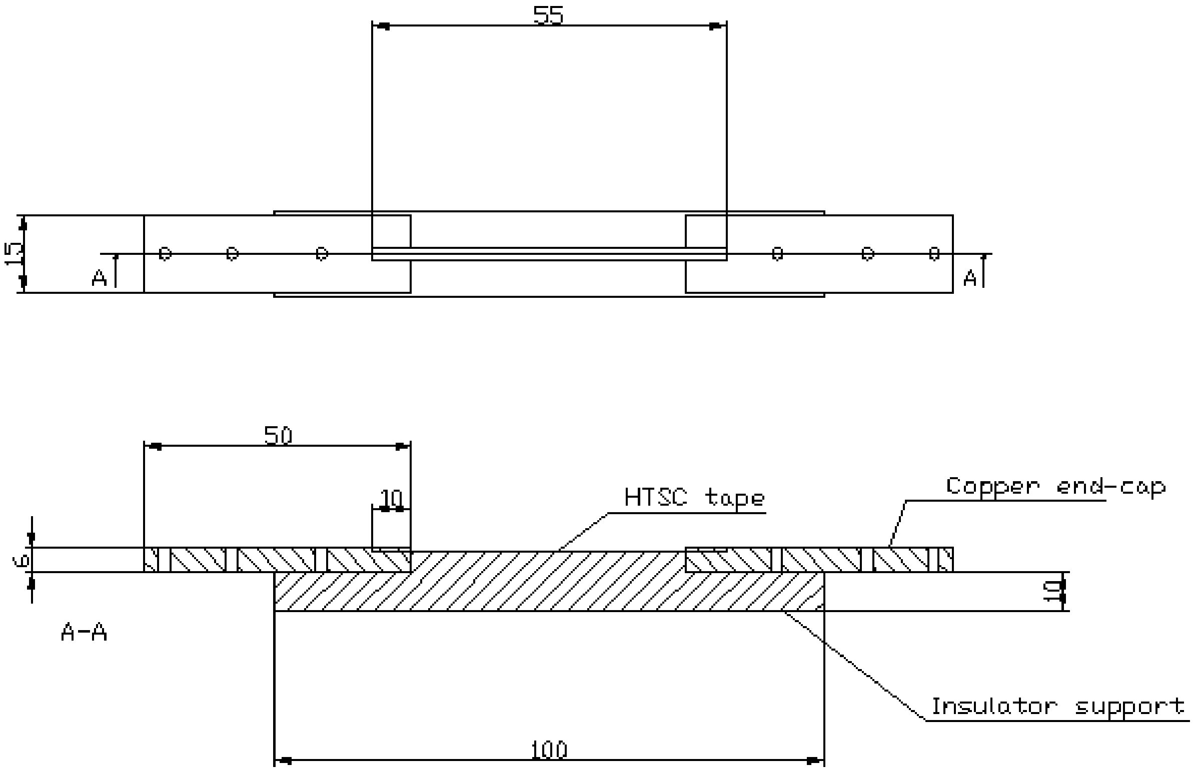

Figure 3-3. Device description.

The results I obtained from these tests are reported in the following pages.

Figure 3-4. Picture of the tape assembly for the tests.

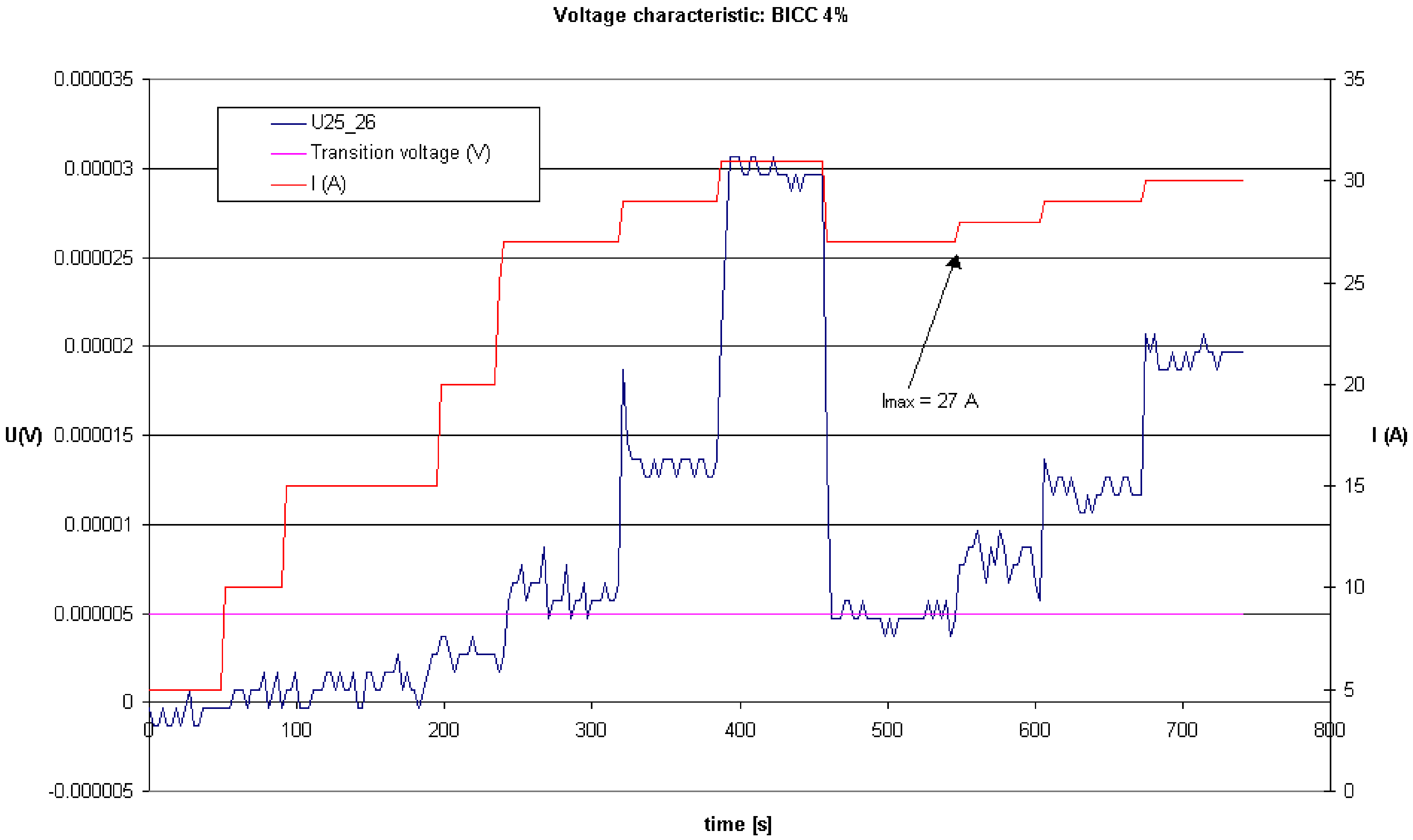
Voltage characteristic: BICC 4%
U25_26
Transition voltage (V)
I (A)
U(V)
0.000035
0.00003
0.000025
0.00002
0.000015
0.00001
0.000005
0
-0.000005
I (A)
35
30
25
20
15
10
5
0
0
100
200
300
400
500
600
700
800
time [s]
Imax = 27 A

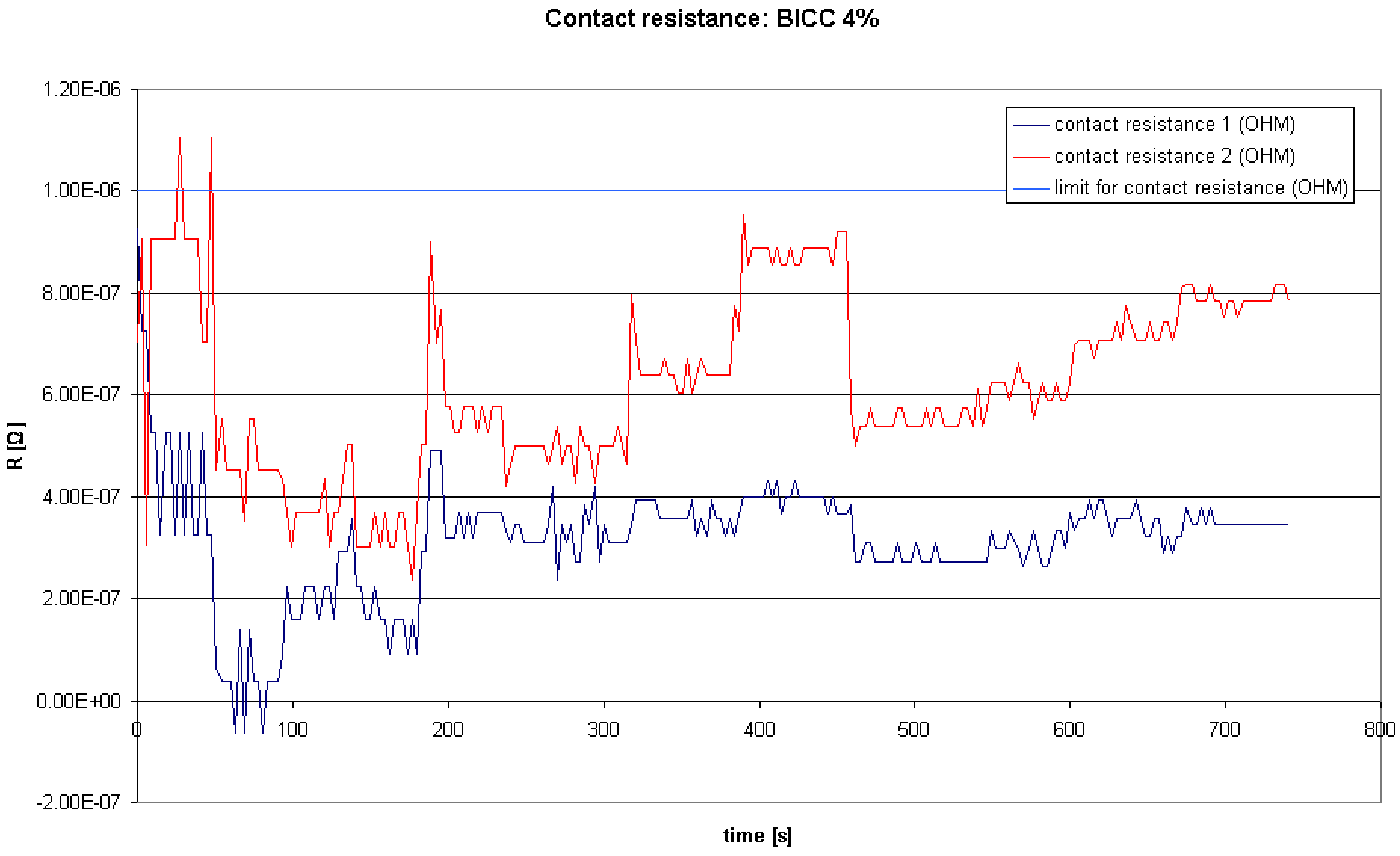
Contact resistance: BICC 4%
R [Ω]
1.20E-06
1.00E-06
8.00E-07
6.00E-07
4.00E-07
2.00E-07
0.00E+00
-2.00E-07
0
100
200
300
400
500
600
700
800
time [s]
contact resistance 1 (OHM)
contact resistance 2 (OHM)
limit for contact resistance (OHM)

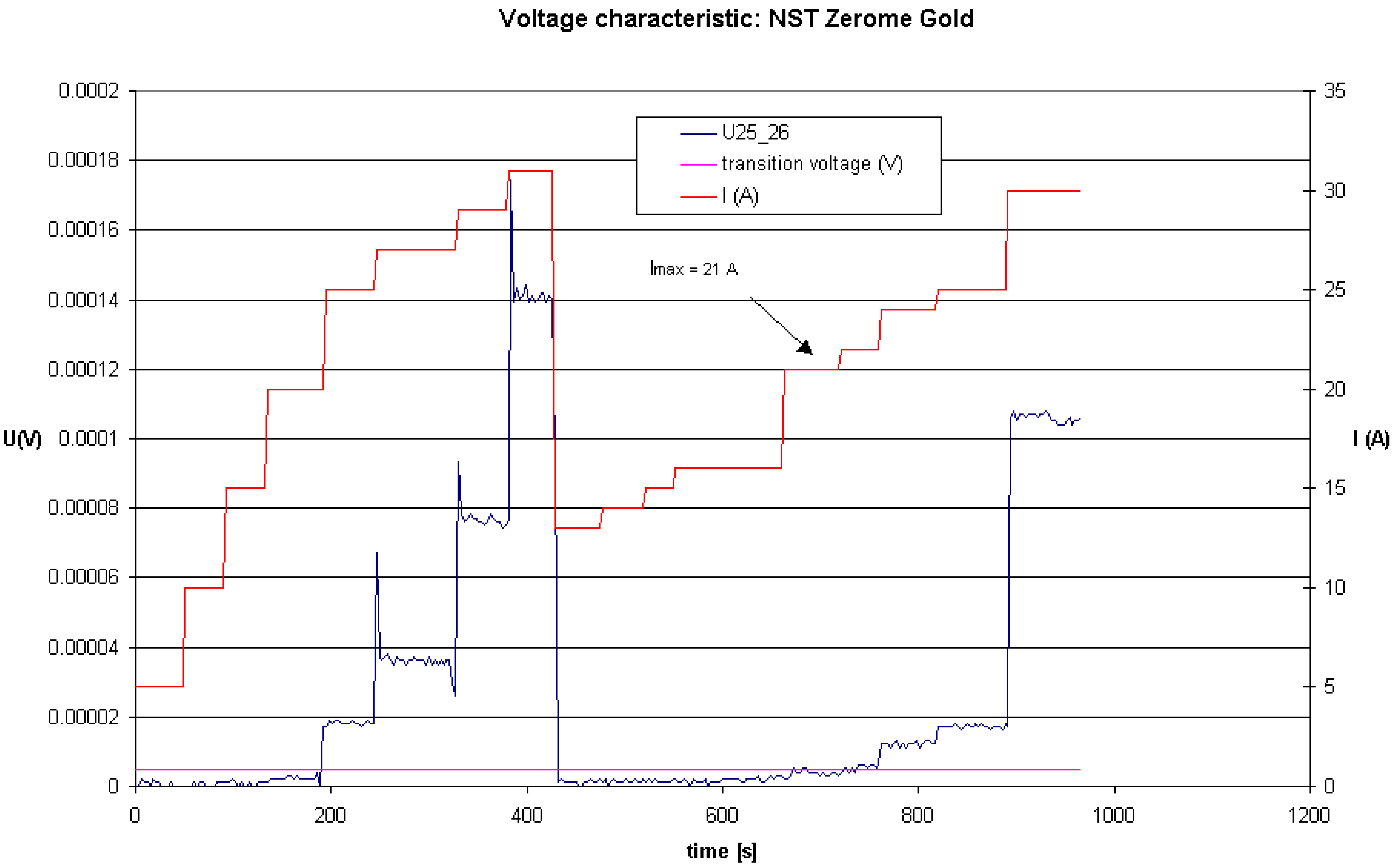
Voltage characteristic: NST Zerome Gold
U25_26
transition voltage (V)
I (A)
Imax = 21 A
U(V)
I (A)
time [s]
0.0002
0.00018
0.00016
0.00014
0.00012
0.0001
0.00008
0.00006
0.00004
0.00002
0
35
30
25
20
15
10
5
0
0
200
400
600
800
1000
1200

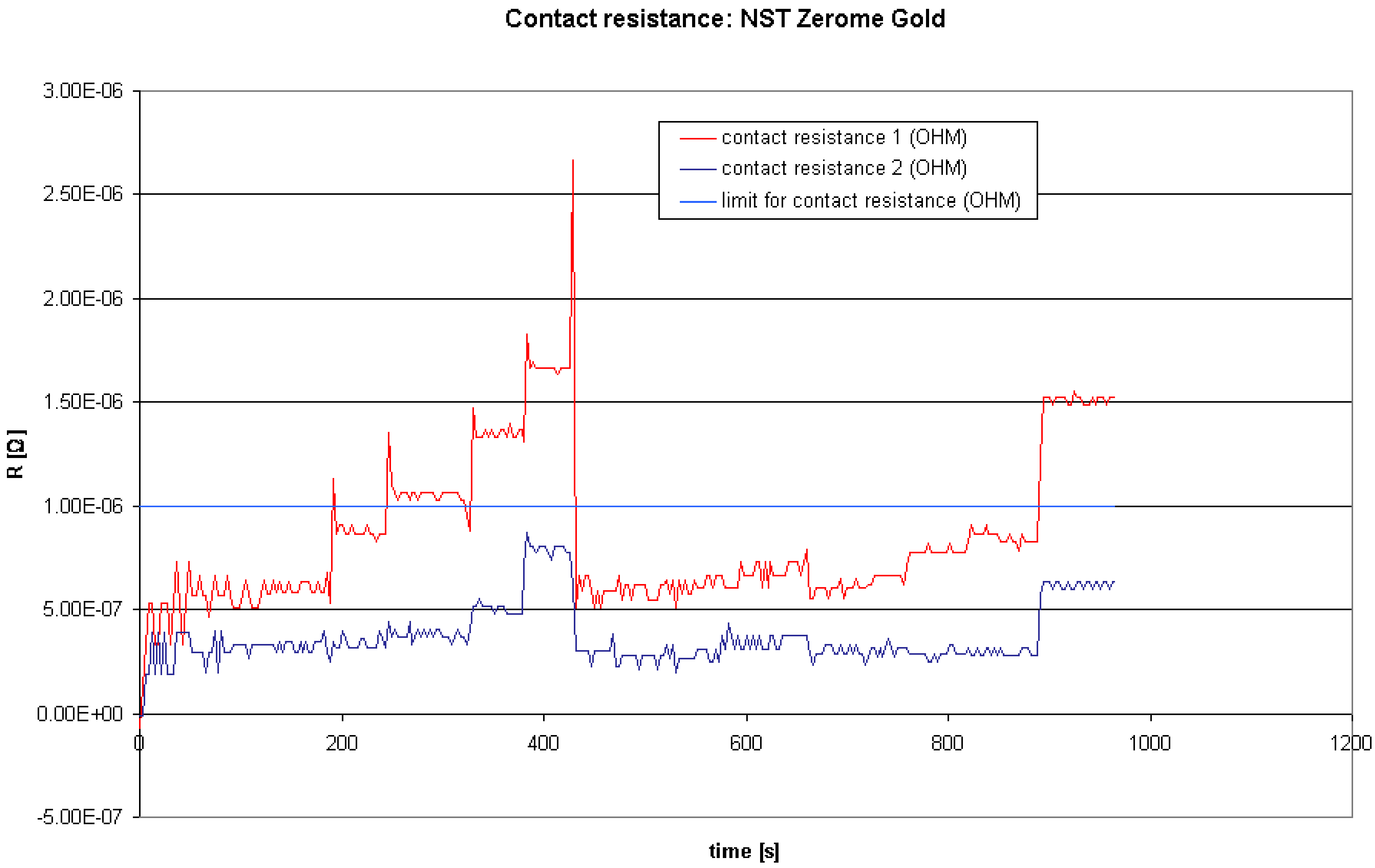
Contact resistance: NST Zerome Gold
contact resistance 1 (OHM)
contact resistance 2 (OHM)
limit for contact resistance (OHM)
R [Ω]
3.00E-06
2.50E-06
2.00E-06
1.50E-06
1.00E-06
5.00E-07
0.00E+00
-5.00E-07
0
200
400
600
800
1000
1200
time [s]

Voltage characteristic: Russian 10%

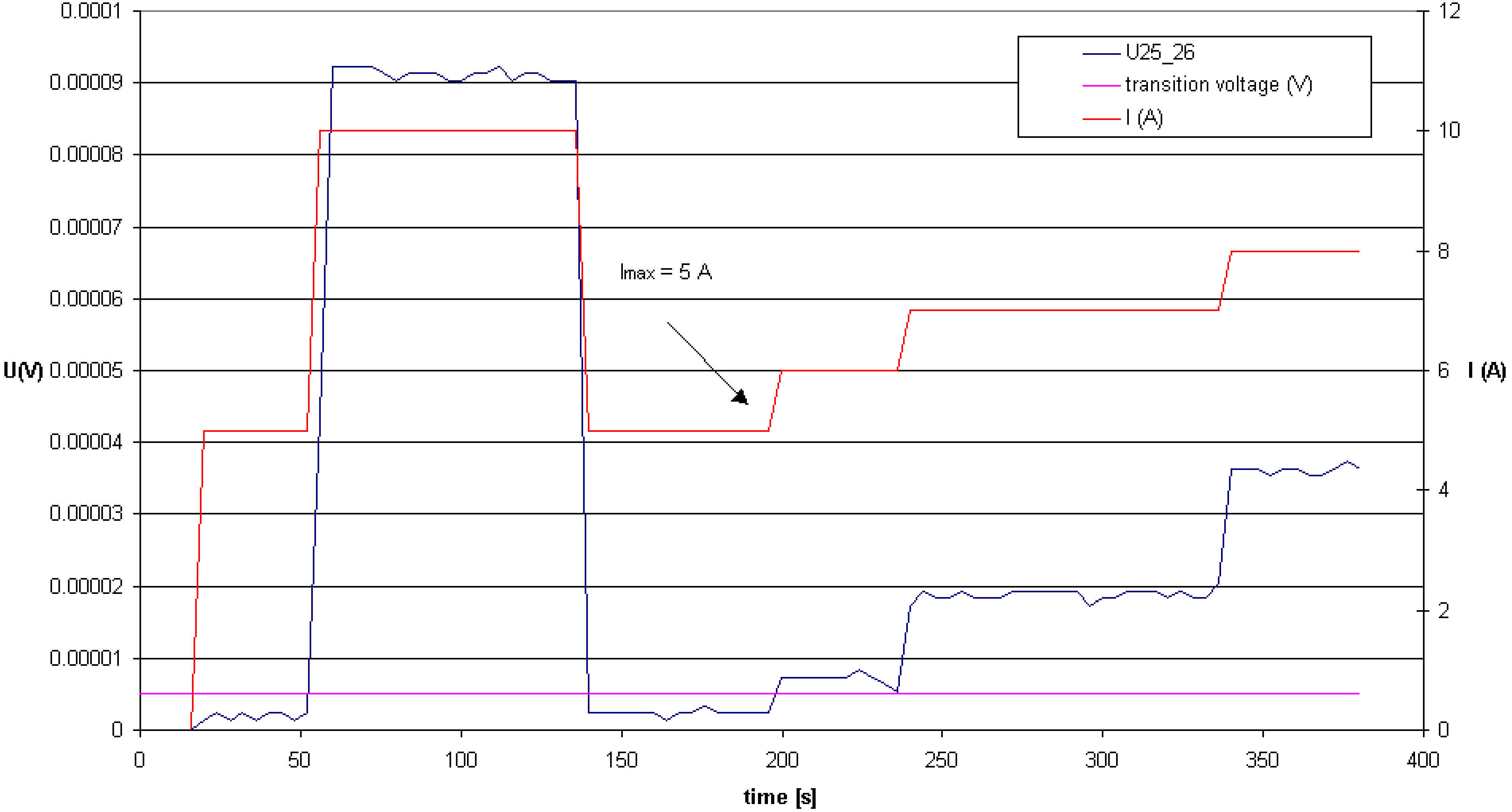

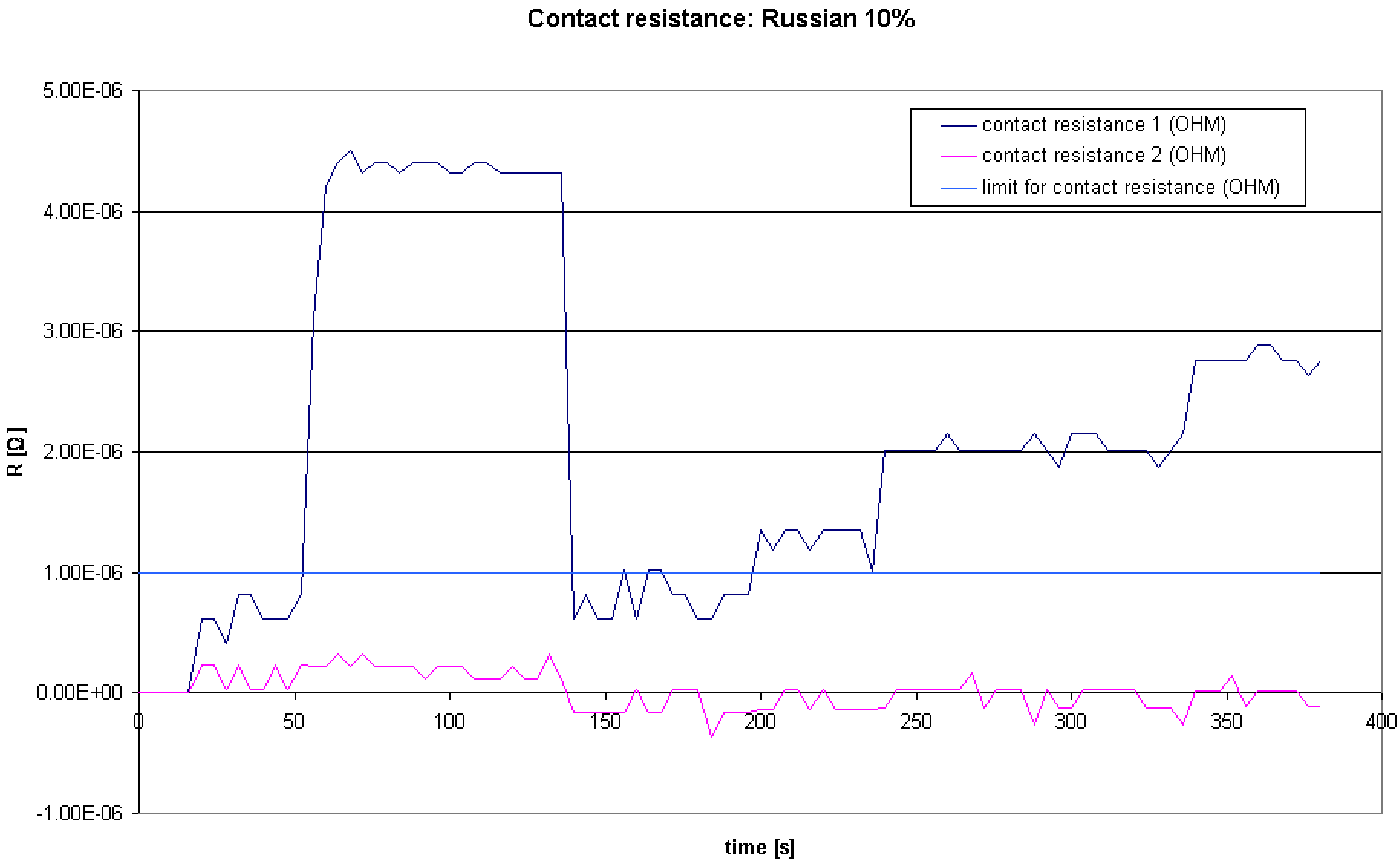
Contact resistance: Russian 10%
contact resistance 1 (OHM)
contact resistance 2 (OHM)
limit for contact resistance (OHM)
R [Ω]
5.00E-06
4.00E-06
3.00E-06
2.00E-06
1.00E-06
0.00E+00
-1.00E-06
0
50
100
150
200
250
300
350
400
time [s]

Voltage characteristic: Russian 1%

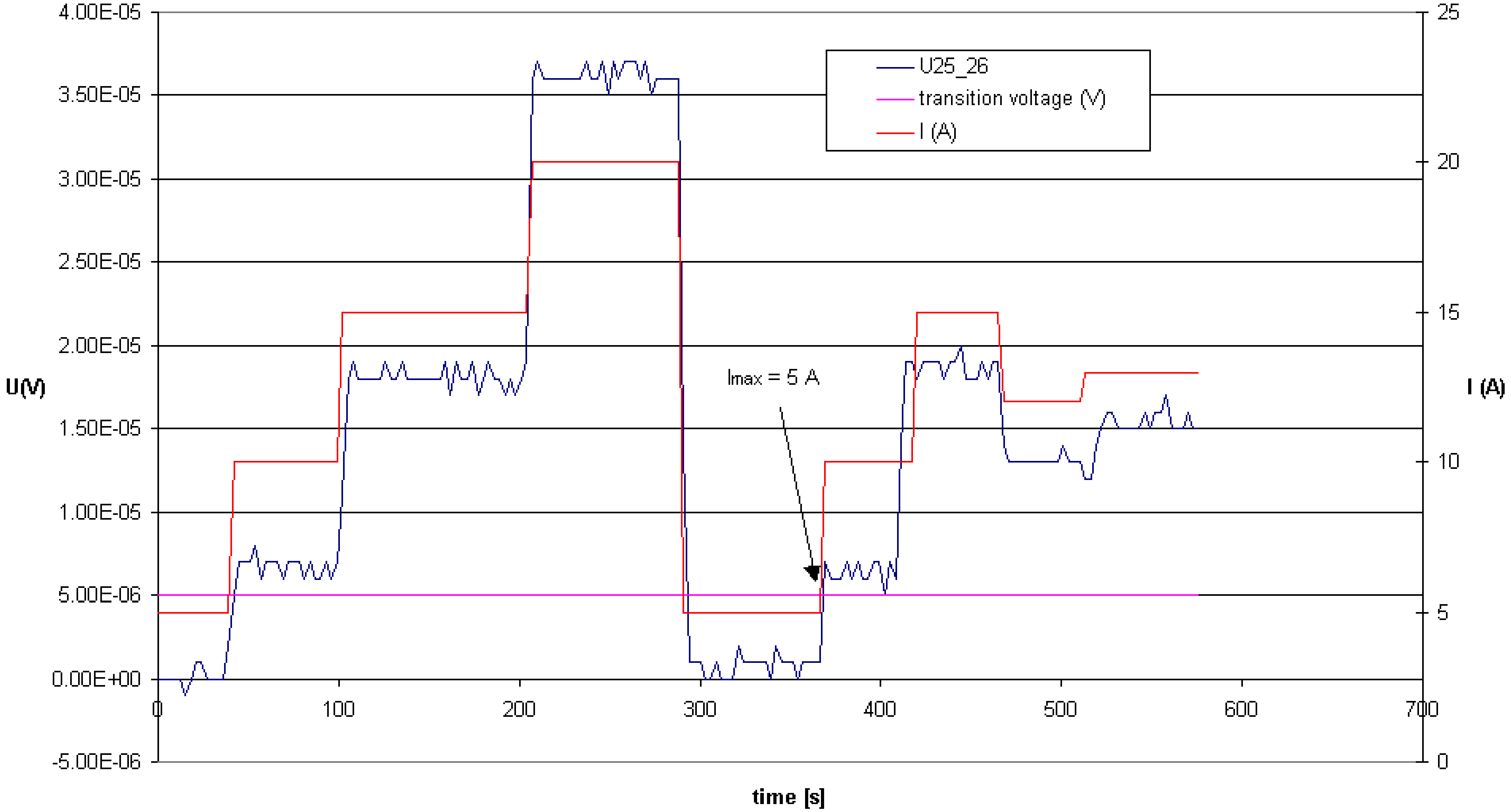

Contact resistance: Russian 1%

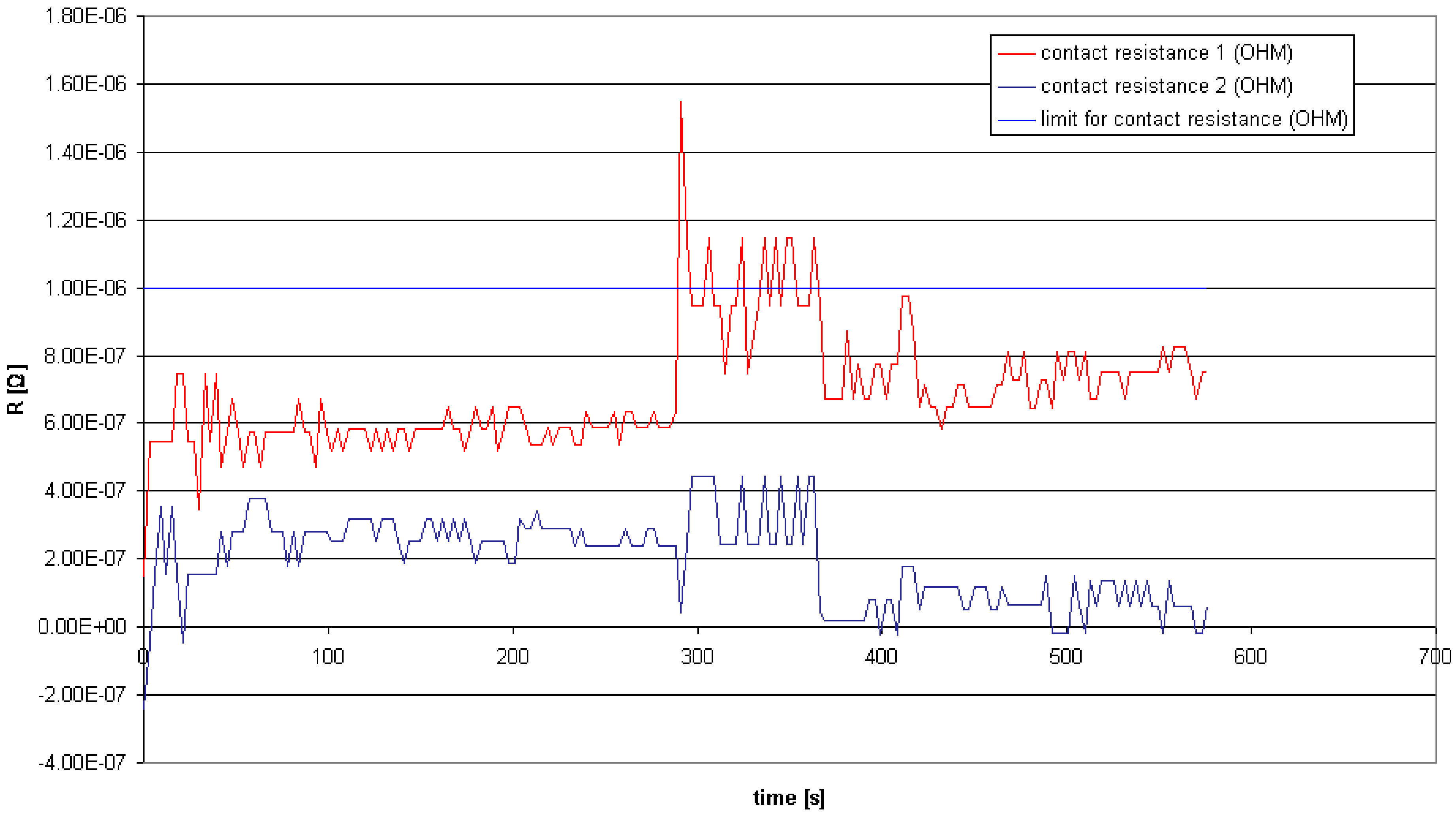

In all the plots of the voltage characteristic it is reported the voltage limit according to the electrical field criterion. When the voltage drop across the tape overcomes this limit, then the superconductor is considered to be resistive. The electrical current flowing at that moment is the maximum allowable current.

The contact resistance in almost all the samples is below the allowable threshold though in some case, at high current, it overcomes this limit. Nevertheless it does not invalidate the tests because of the small duration in time so that the small Joule heating is not dangerous.

A sketch of the disposition of the voltage probe is shown in Figure 3-5.

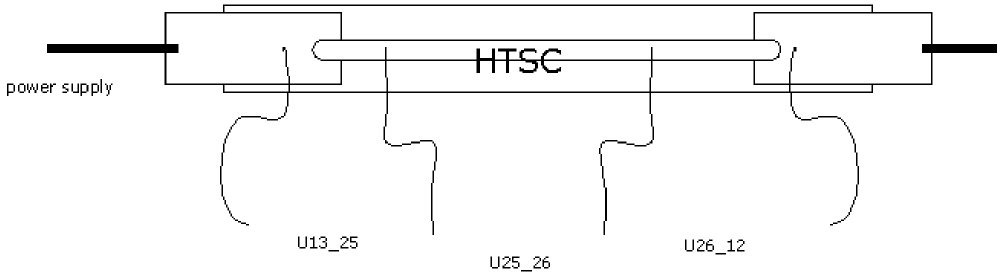

Figure 3-5. Voltage probe disposition.

The measured critical current densities at 77 K are reported in the following Table 3-2.

Table 3-2.

Tape	Ic [A]
BICC 4%	27 A
NST Zerome Gold	21 A
Russian 10 %	5 A
Russian 1 %	5 A

3.2 SEM Analysis

A useful tool for gaining information on the composition and stoichiometry of new crystalline samples is a Scanning Electron Microscope (SEM) equipped with an Energy dispersive x-ray (EDX) spectrometer.

The scanning electron microscope differs from transmission electron microscopes which use the transmission of electrons through a sample to resolve an image: it requires the preparation of films so thin that they are transparent to a beam of electrons with energies of roughly 200 keV. This implies that the film must have a thickness of only one or a few hundred nanometres (10^{-9} metre). The scanning electron microscope uses a narrow beam of electrons (often of about 40 keV) that scans the surface of a sample and forms a corresponding image from the backscattered electrons or secondary electrons. No special surface preparation is necessary and, since the depth of focus in an SEM is much greater than in an optical microscope, quite irregular surfaces, such as fractures, can be studied successfully.

The electron beam is obtained by thermionic effect applying a voltage to a tungsten filament. A strong electric field between the filament and the anode plate causes the electrons to be accelerated towards the target. The optical column of the electron microscope must also typically be pumped down to a hard vacuum so that the filament does not oxidize and to prevent air molecules from interfering with the electron beam. It usually operates at a pressure low enough so that the mean distance that the electrons in the beam cover, before striking an air molecule, is longer than the length of the microscope column.

The electron beam is scanned back and forth over the surface of the specimen using electromagnetic lenses and the electrons that are reflected or emitted from the specimen are used to resolve an image on a cathode ray tube or computer monitor.

The electrons in the beam will penetrate to a depth that is directly proportional to the energies of the electrons in the primary beam and inversely dependent on the atomic number of the atoms in the specimen. The scattering effect within the sample could be divided into two main groups. In the first group, electrons are scattered due to elastic collision with atoms in the specimen and lose very little energy in the process: these electrons are called backscattered electrons and typically have energies greater than 50 eV. In the second group, electrons collide inelastically causing the specimen atom with which they collided to ionise. Electrons emitted as a result of this ionisation are called secondary electrons and generally are characterised by energies less than 50 eV.

The primary and secondary electrons are collected and passed to a scintillator, which produces light when bombarded with electrons. The light is passed to a photomultiplier tube, where it is converted back to an electric signal with an effective gain of 10000 times or more. The resultant amplified current is used, in turn, to modulate the brightness of a display cathode-ray (television) tube that is scanned in synchronism with the probe beam in the microscope column. In this way it is possible to obtain a final magnification of 1,000-250,000 magnitudes on the screen.

Another effect of the striking beam is the emission of radiation, in particular x-ray radiation. Some electron energy is caught in the electric field of the atom, as the electrons decelerate, and is irradiated as x-ray: this is the background white radiation. A small but significant portion of the electron beam collides with the electrons of the target atoms. Some of the target electrons are knocked out of their orbitals, leaving the target atom in a high-energy excited state. The excited state is brief and the stored energy is released as the electrons from the others orbitals drop into the vacant one. These electron transitions are quantized and the radiation emitted has specific wavelengths: the x-rays exiting the target have a few strong characteristic concentrations of specific wavelengths superimposed on the white radiation.

There are two ways of detecting the x-rays released from the sample: a wavelength dispersive spectrometer, which separates x-rays according to wavelength; or an energy dispersive spectrometer, which measures the energies of the x-rays [23].

The geometry of the crystal lattice controls the directions of diffracted beams. The intensity of these beams depends on the types of atoms in the crystal and their arrangement in the unit cell.

X-ray spectroscopy in the SEM analysis involves the identification of a specific energy or wavelength for elemental analysis of the specimen. Once detected the relative peaks of the X-ray spectrum above the white-noise, Bremstralung radiation, can then be used to determine the chemical composition of the sample.

3.2.1 X-ray diffraction

Together with the SEM analysis another way to examine the crystal lattice and phase composition of a sample is the x-ray diffraction. In this section I will briefly describe how it works.

The atoms contained in a solid are arranged so that a specific structural motif is repeated in a periodic manner in all directions. This property allows the description of the location of every atom in a macroscopic crystalline substance by only describing the location of a few atoms with respect to a three dimensional crystal lattice [24].

Once defining the three-basis vector of the lattice, they can be used to enclose the basic repeating unit of the crystal. This parallelepiped, known as *unit cell,* is described by the crystallographic axes *a, b* and *c* and their interaxial angles a, b and g. All crystals can be divided into 14 categories due to their lattice types. These are the so-called Bravais lattices.

When X-rays illuminate a crystalline material, the atoms in the crystal act as scattering centres. Because of the periodic nature of crystals, the scatterers can be considered to be associated with periodically spaced plane a distance *d* apart. For certain angles of incidence of the beam the X-rays are scattered coherently and in phase. The Bragg equation that gives the geometric condition required for a coherent scattering, is given by:

$$(7) \qquad n\lambda = 2d\sin\theta$$

where *n* is an integer, l is the wavelength of the incident X-rays, *d* is the interplanar spacing and q is the angle between the plane and the incident X-ray beam. If the X-rays illuminating the sample are of fixed wavelength, i.e. they are monochromatic, this equation gives a simple relationship between *d,* interplanar spacing, and the diffraction angle.

It then becomes necessary to identify these planes in some systematic way. This is best done by describing the planes in terms related to their intercept on the crystallographic axes: a method developed by H. Miller.

In this construction the fractional intercepts of the plane on each axis are determined, the reciprocal of these intercepts are calculated and, finally, any fractions are cleared to leave three integers *h, k* and *l.* Doing so the general equation of the plane can be written as:

$$(8) \qquad \left(\frac{hx}{a}\right)+\left(\frac{ky}{b}\right)+\left(\frac{lz}{c}\right)=n$$

For any given set of value for the Miller indices *hkl,* the all possible values of *n* leads to the description of an infinite set of equally spaced parallel planes. The Miller indices also provide a convenient method for determining the interplanar spacing, d_{hkl}, which replaces *d/n* in the Bragg equation.

It is evident from the above that the relative dimension of the crystal lattice determine the diffraction angles in an X-ray diffraction experiment.

However the Bragg's equation does not contain information about the scattered intensity from a given phase. It only provides a geometric condition for scattering to be observed.

What then determines the diffracted intensity?

It is known that the X-rays are scattered by an atom in different ways according to the scattering power of it. This scattering power depends on the physical and chemical characteristics of the atom such as: atomic number Z, mass number M and so on. According to the intensity of the diffracted beam one can determines the kind of atom in the unit cell that is responsible of such behaviour. So it appears obvious that the scattered intensity in an X-ray diffraction experiment is determined by crystal structure.

X-ray diffraction can be broadly divided into two major techniques:

- single crystal
- powder diffraction

The single crystal technique is quite powerful. In this procedure an individual crystal is oriented so that each *hkl* plane may be examined separately. In this way it becomes easy to determine the unit cell parameters and symmetry elements associated with the crystal structure. Furthermore, recording the intensity for each reflection from a given *hkl* plane it is possible to determine the location of each atoms in the crystal: the crystal structure.

Unfortunately these experiments are sometimes quite time consuming and so the technique is limited in its appeal in a day to day analytical tool.

The X-ray powder diffraction experiments, on the other hand, can be obtained quickly and are useful in the identification of phases in mixtures of crystalline substances. In this method the sample is ground so that it is composed of micron sized crystallites and the X-ray diffraction pattern of this powdered sample is then recorded.

Because of the randomly orientation of the crystallites, each *hkl* plane has a definite probability of being positioned at its proper Bragg angle. The powder diffraction technique reduces the three dimensional *hkl* information to a single dimension, d_{hkl}. This information, however, constitutes the "fingerprint" of a given crystalline substance, so the powder method is useful for the identification of unknown phases.

3.2.2 Tape analysis

The BICC tapes and the Russian one were analysed according with the SEM analysis, in order to check their chemical composition and the quality of the manufacturing. Instead of the NST tape another Russian tape was analysed with a different Au content in the metallic matrix.

In the following paragraph are reported the results of these tests.

3.2.2.1 BICC

The chemical composition of the oxide material is:

Element	Weight %	Atomic %
Ca	8.59	22.35
Cu	15.06	24.71
Sr	21.50	25.58
Bi	54.85	27.36

The oxide is clearly a BSCCO type.

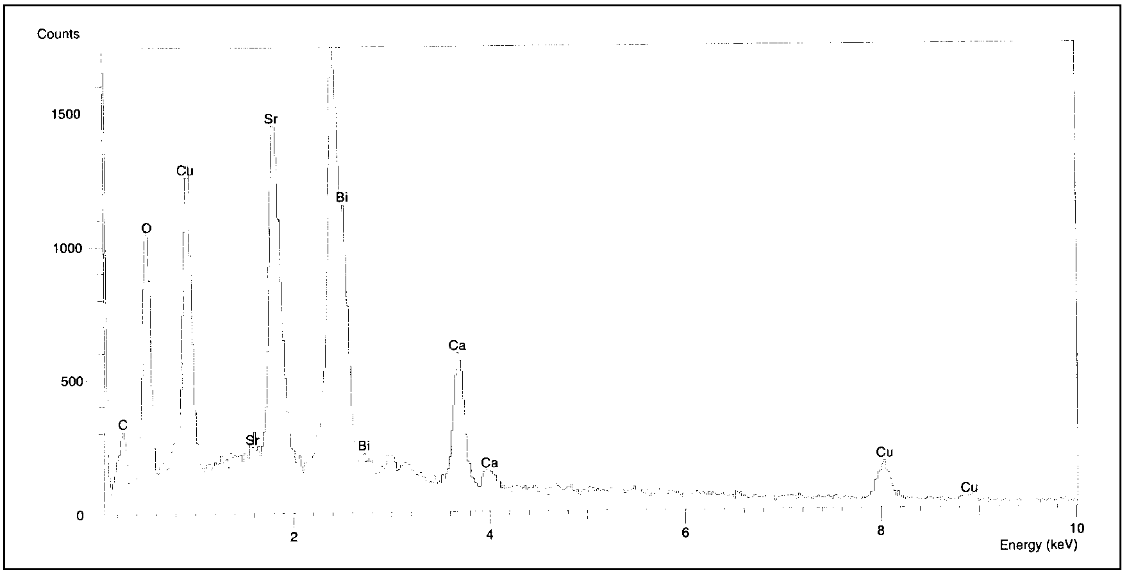

Figure 3-6. Quantitative x-ray analysis: superconducting part.

The silver matrix is an Ag-Au alloy with a Gold content of 4% in weight.

Element	Weight %	Atomic %
Ag	96.07	97.81
Au	3.93	2.19

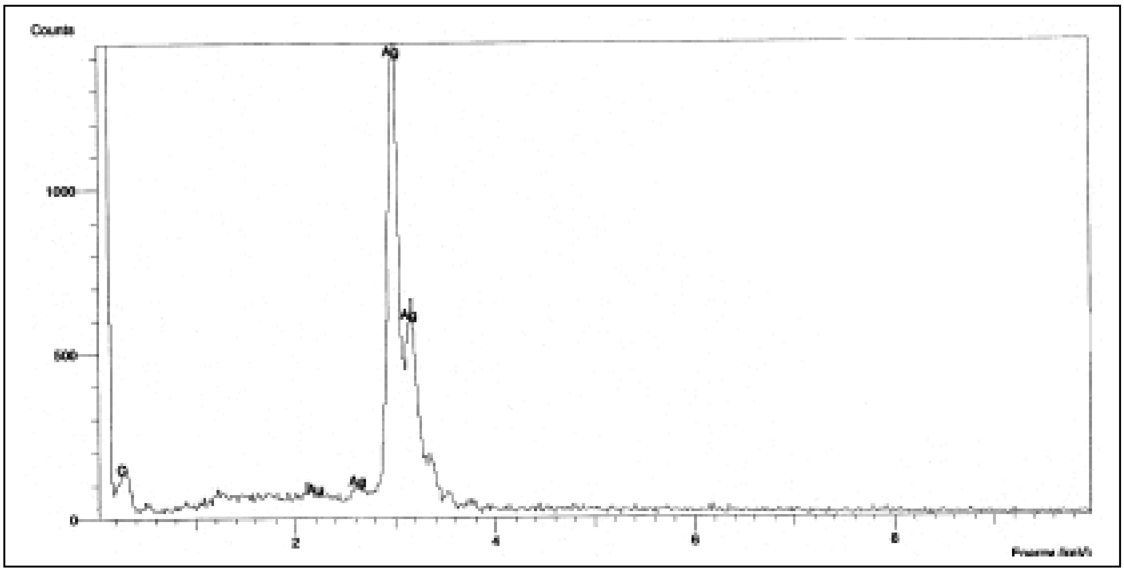

Figure 3-7. Qualitative x-ray analysis: silver matrix.

3.2.2.2 Russian 10

The chemical composition of the oxide material is:

Element	Weight %	Atomic %
Ca	8.39	21.68
Cu	16.25	26.49
Sr	21.13	24.97
Bi	54.22	26.86

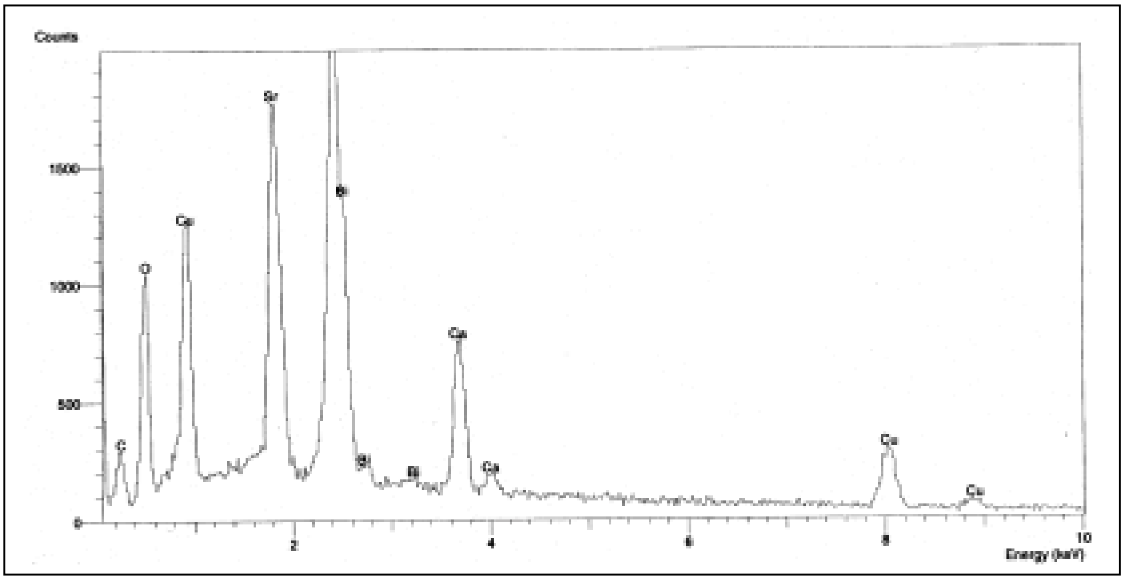

Figure 3-8. Qualitative x-ray analysis: superconducting part.

The matrix alloy is an Ag-Au with gold content of 10% atomic.

Element	Weight %	Atomic %
Ag	82.42	89.54
Au	17.58	10.46

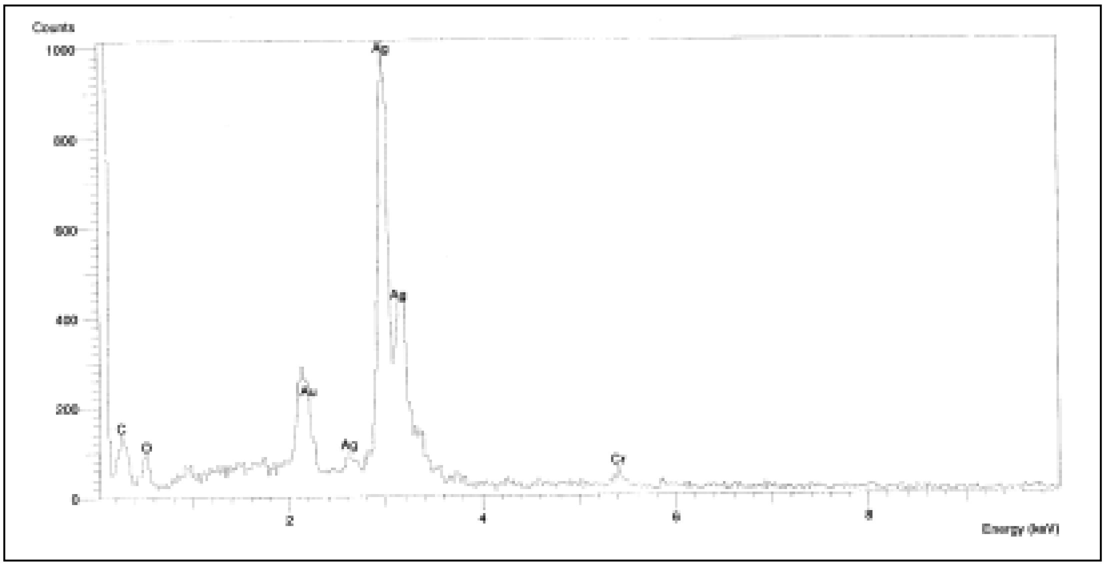

Figure 3-9. Qualitative x-ray analysis: silver matrix.

3.2.2.3 Russian 1

The oxide composition is:

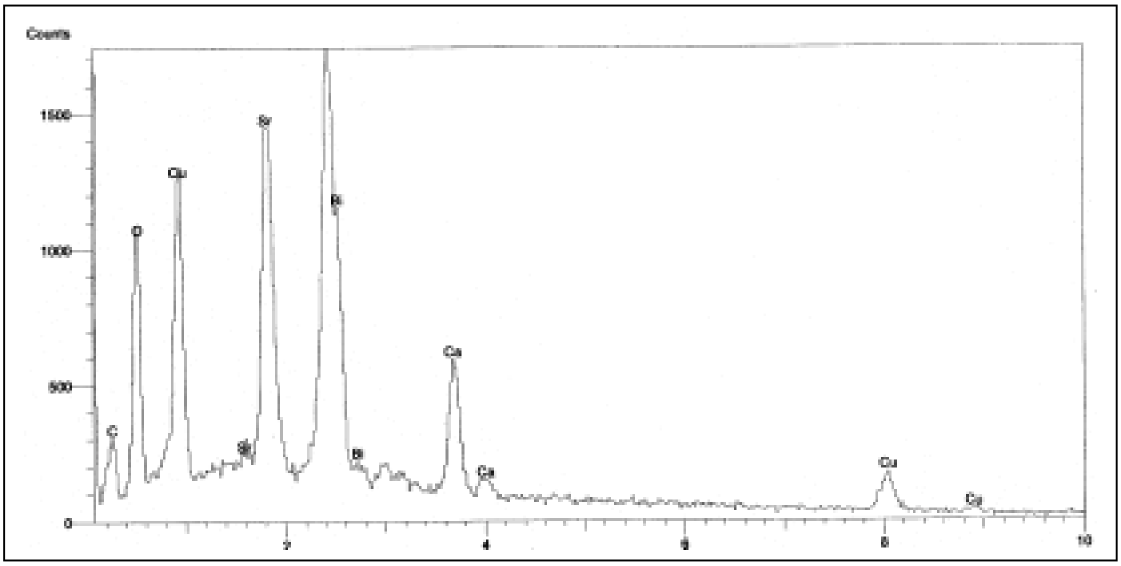

Figure 3-10. Qualitative x-ray analysis: superconducting part.

Element	Weight %	Atomic %
Ca	9.09	22.59
Cu	19.74	30.96
Sr	18.96	21.56
Bi	52.22	24.90

The alloy matrix is an Ag-Au 1% at.

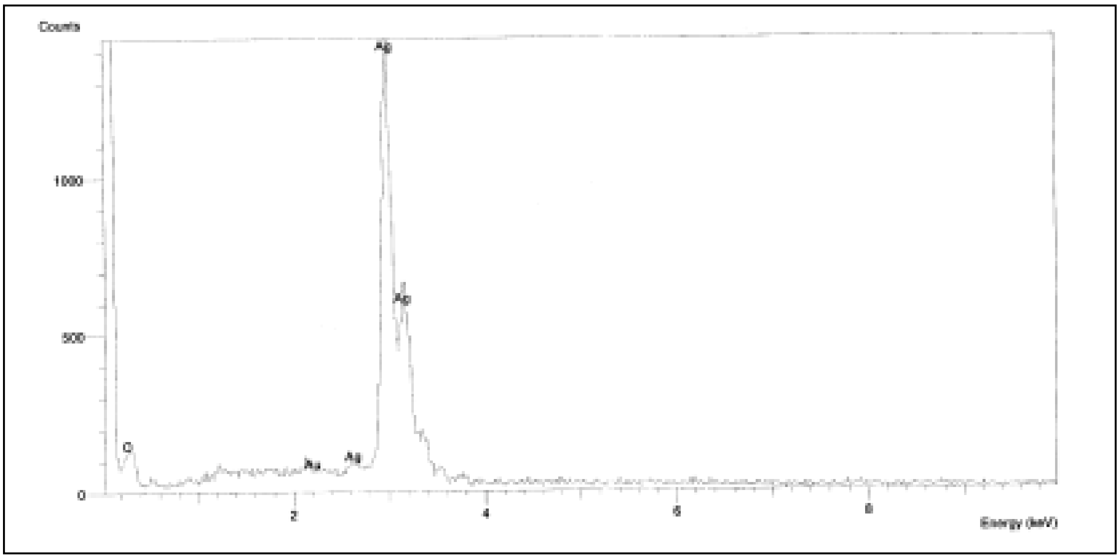

Figure 3-11. Qualitative x-ray analysis: silver matrix.

Element	**Weight %**	**Atomic %**
Ag	98.23	99.02
Au	1.77	0.98

Some images were taken during the analysis of the longitudinal and transversal cross section of the samples.

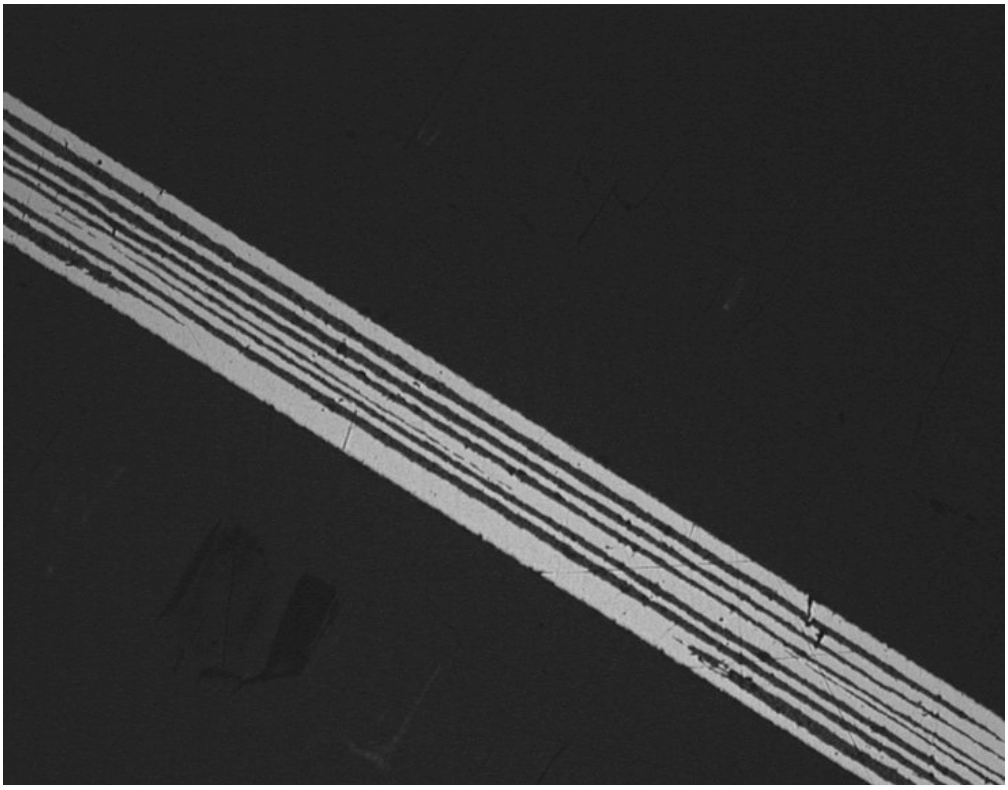

Figure 3-12. Transversal cross section of BICC’s tape.

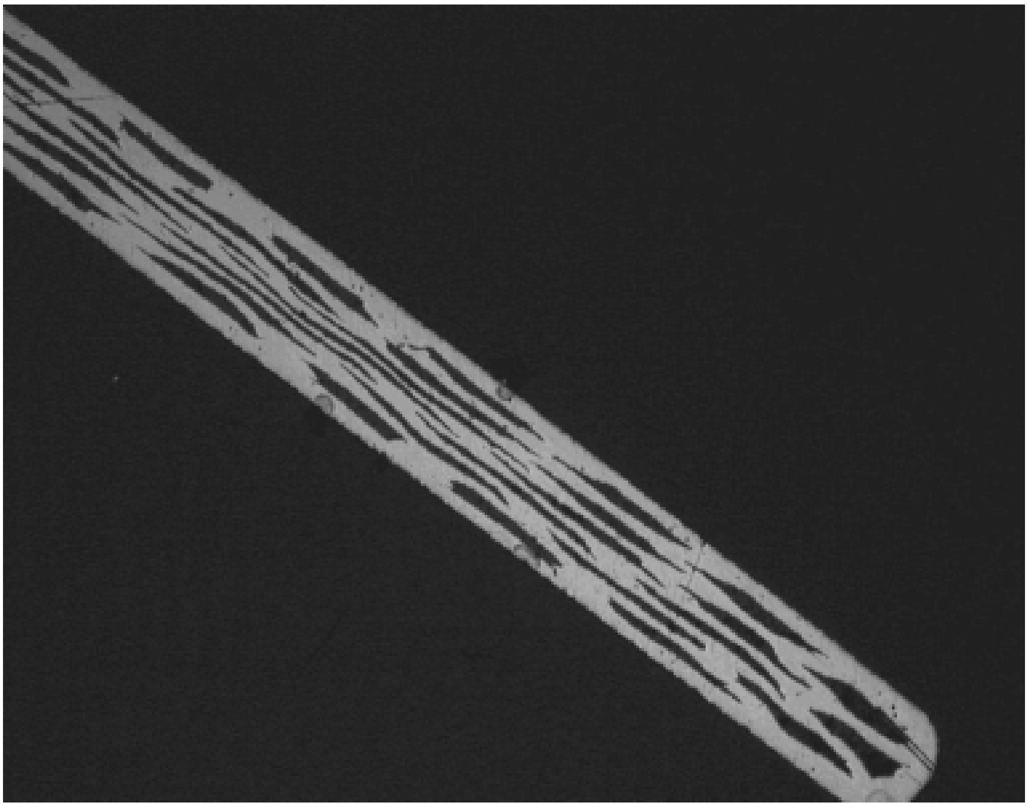

Figure 3-13. Longitudinal section of the BICC’s tape.

4 Thermal model

Since the discovery of high temperature superconductivity (1986), large efforts were made to improve the electrical and mechanical properties of the HTS. At present day their wide technological employment is limited by the sensitivity to mechanical stresses, the low critical currents and the sensitivity to magnetic field at high temperature. An immediate and less stringent application of this emerging technology is in the current leads.

The Large Hadron Collider (LHC), currently under construction at CERN, is by far the largest user of superconducting magnets requiring the transfer of over 3 million amperes of current from the power converters, at room temperature, into the liquid helium bath. The HTS technology for the current leads is a great opportunity to incorporate these materials into large-scale systems.

The use of HTS in the lower part of the current leads instead of using classical vapour cooled leads, allows reducing the heat leak into the liquid helium environment by a factor of ten [25].

Due to their crucial rule it is necessary to study the leads in all their critical aspects. The most critical one is the resistive transition: known as quench. When in resistive mode almost the whole amount of current passes through the metallic matrix or through the protection shunt of the HTS, which starts to heat up.

If a quench occurs it is important to evaluate all the consequences for the leads and above all it is important to know their behaviour during this kind of transient and all the factors that influence it in order to protect the assembly and to avoid the burn-out.

In this chapter it will be described a thermal model for the high temperature superconducting part of the current leads which will take into account all the physical aspect of the problem and which will allow to study the behaviour of the leads during a quench transient.

4.1 Current leads description

Hybrid superconducting-normal metal current leads have undergone intensive development over the last few years and they are now suitable for application in low temperature superconducting systems. Current leads introduce heat into cryostat by thermal conduction and, if the leads are not superconducting, by Joule heating. Different types of hybrid leads have been designed to electrically connect the power supplies, at room temperature, to the low temperature superconducting magnets, using both bulk materials and high temperature superconducting tapes.

At CERN first, and then within the framework of the European BRITE/EURATOM [26, 27] project a pair of hybrid superconducting current lead has been designed: it is composed of copper conductor for the electrical connection from room temperature to an intermediate temperature (T_{HTS} = 77K), and high temperature superconducting tubes conducting the current down to liquid helium temperature. The material used was the Bi-2212 bulk tube with integrated silver contacts, manufactured by the melt casting method.

In the BRITE/EURATOM design the copper part is cooled by cold nitrogen vapour produced during the operation from the liquid nitrogen bath where the copper conductor is dipped. The superconducting part, because of the low thermal conductivity of the Bi-2212 conductor, can operate in a vacuum ambient where cooling is provided only by thermal conduction. With this assembly current density up to 1000 A/cm² are reached in a 1.15 T magnetic field. The helium boil-off, due to the heat conducted outside the vacuum insulation, is reduced by a factor of ten and the total refrigeration load by a factor of five.

Another design uses the YBCO bulk conductors. It is a hybrid solution, which could be of a conduction cooled type or a vapour cooled type as regards the HTS part [28, 29]. This model is though to work in a metastable mode: a partially superconducting state for which the effective resistivity is about 0.1 times that of the normal state. Composites of Ag and YBCO are of interest because Ag improves the mechanical strength of the superconductor. In this case, with leads operating in the superconducting state, the helium boil-off will be less than half that obtained for pure metal leads.

For operating current densities above 10000 A/cm², textured Bi-2223/Ag tapes are an alternative to Bi-2212 bulk materials [30]. The use of the HTS on the lower part of the current leads, has the potential to reduce the required room temperature refrigeration power to one fifth of that consumed by a conventional current lead. In this case several solutions for the cooling scheme are possible: using separate cooling for the resistive and the superconducting part, using unique cooling for the two, using nitrogen vapour for the resistive part and helium vapour for the superconducting, and in different assembly type.

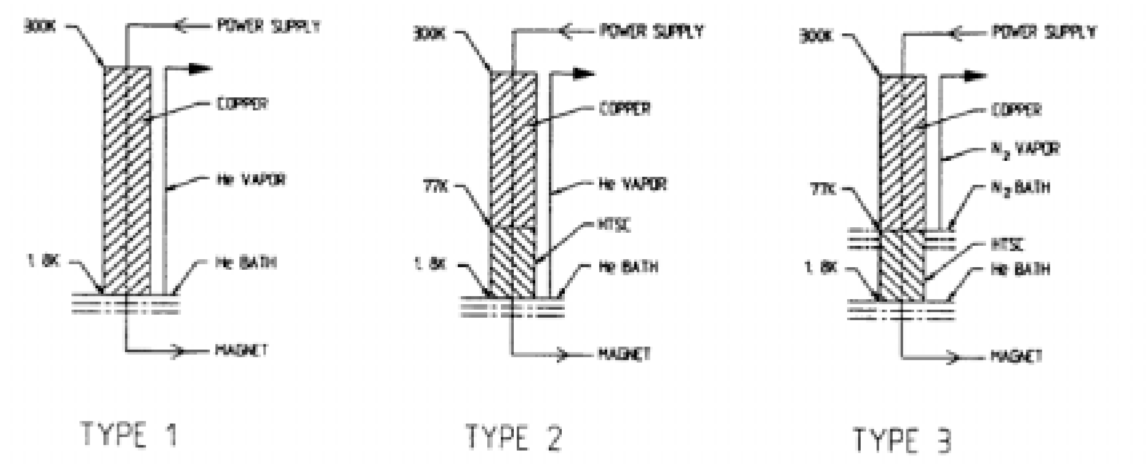

Figure 4-1. Example of three different cooling scheme [31].

The current leads for LHC are designed to take full advantage of the cryogen available. Prior to start the design of the leads a study has been made [25] to evaluate the exergetic costs of different cooling methods offered by the already well defined infrastructure of the LHC machine, and the potential saving in liquefaction power.

The most convenient solution, now adopted for all the HTS leads, consist in the following. The superconducting bus from the magnet traverses a lambda plate to enter the 4.5 K liquid helium bath in the distribution feed boxes (DBF), i.e. cryostats where the leads are located. At its cold end the lead dips into the 4.5 K, 1.3 bar helium. The lower section of the lead incorporates HTS material, the warm end of which is maintained at less than 50 K using helium gas from the 20 K, 1.3 bar line, recovered from the beam screen cooling line. This gas is used to cool the classical upper heat exchanger and is recovered at room temperature in the warm gas line. The HTS part of the element operates in self cooling conditions between an intermediate temperature (T_{HTS} = 50 K), depending from the flow and the design of the resistive part, and the 4.5 K liquid helium bath.

Different HTS materials have been tested. My work is concentrated on the BSCCO 2223 with an Ag-Au matrix. The silver alloying is necessary to reduce the heat leak due to the high thermal conductivity of silver: alloying with gold reduces the thermal conductivity of the metal. A sketch of the assembly is reported in Figure 4-2.

As regards the silver-alloy matrix different enrichment in Au are possible and also different ratios between superconducting oxide and metallic matrix. One of the goals of the model is to scan over the different choices.

The main goals of the theoretical model are:

- to evaluate the heat leak into the liquid helium bath;
- to evaluate the temperature profile across the HTS;
- to calculate the helium boil-off due to silver conduction;
- to study the quench transient.

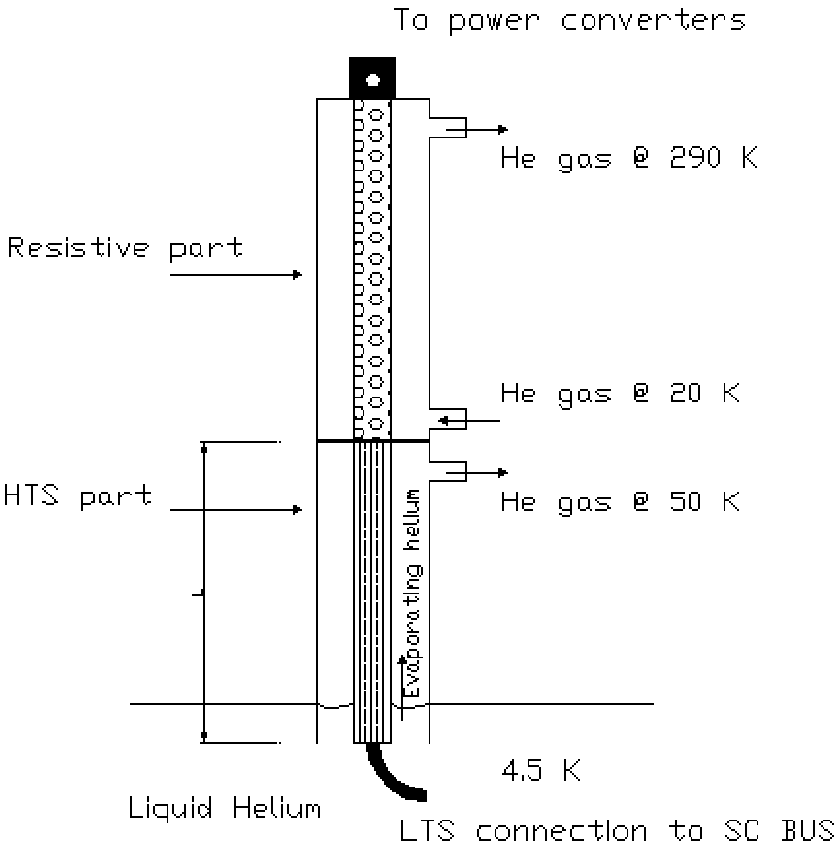

Figure 4-2. Cooling scheme of a current lead for the LHC.

4.2 All-metal leads

The 4.2 K heat leak in low temperature systems due to conventional all metal current leads often represents an important part of the total losses in these systems. As stated above the choice of a hybrid current lead which uses an HTS on the lower part will considerably reduce this heat load.

The minimum heat leak for a conduction-cooled all-metal current lead is easily achievable by solving the general equation for the heat balance:

$$\begin{aligned} & Q(T) = -k(T)A\frac{dT}{dx} \\ & \frac{dQ}{dx} = \frac{\rho(T)I^2}{A} \end{aligned} \tag{9}$$

k(T) and *ρ(T)* are the thermal conductivity and electrical resistivity, A is the cross sectional area and *I* the flowing current. As a first approximation we can assume *k* and ρ constants in the temperature range $T_H - T_L$ (temperature of the upper end and lower end respectively). Then we can integrate:

$$\begin{aligned} & \frac{\rho AdQ}{I^2} = -kA\frac{dT}{Q} \\ & QdQ = -k\rho I^2 dT \\ & \int QdQ = -\int k\rho I^2 dT \\ & Q(T) = I\sqrt{2k\rho(c-T)} \end{aligned} \tag{10}$$

If we want to know when the Q_L is minimum, i.e. what is the configuration of the lead which minimise the heat flowing into the cold region at T_L, looking at the equation (10) it is clear that this will occur when *c* is a minimum. Then *c* represent the highest possible temperature on the lead, for if *T* is larger than *c*, the quantity under the radical becomes negative. The temperature range varies from T_H and T_L: the minimum for *c* is, then T_H, i.e. the temperature of the hot end of the lead.

Substituting in (10) this value of *c* it is obvious that this means that the minimum for the heat flow in the cold region is reached when no heat enters the wire at the hot end.

According to these equations the losses cannot be reduced below the limit imposed by the relation existing between the electrical resistivity and the thermal conductivity described by the Wiedemann-Frantz-Lorentz law (WFL), which applies to pure normal metals. In the HTS the electrical resistivity vanishes if the material remains in the superconducting state: this permits to escape from the WFL law and to greatly reduce the 4.2 K heat load.

In order to appreciate the power saving due to the HTS current leads it is necessary to make an estimate of the conventional heat leak due to conventional all metal current leads.

The Wiedemann-Frantz-Lorentz law is expressed as:

$$(11) \qquad k(B,T)\rho(B,T) = \Lambda T$$

where *k* is the thermal conductivity for the metal and ρ is the electrical resistivity as functions of the magnetic field (B) and of the temperature (T). *Λ* is the Lorentz number $\Lambda = 2.45\ 10^{-8}\ \mathrm{W\Omega K^{-2}}$.

The equation that describes the conduction heat transfer for an all-metal conductor is:

$$(12) \qquad \frac{d}{dx}\left(k(T)A\frac{dT}{dx} \right) + \frac{\rho(T)I^2}{A} = 0$$

where *A* is the cross section area of the conductor and *I* the flowing current.

If we set:

$$(13) \qquad \begin{array}{l} Q(T) \equiv -k(T)A\dfrac{dT}{dx} \text{ and consequently} \\ k(T) \equiv -\dfrac{Q(T)}{A}\dfrac{dx}{dT} \end{array}$$

writing the (11) as:

$$(14) \qquad \rho(T) = \frac{\Lambda T(x)}{k(T)}$$

the equation (12) could be rewritten as:

$$(15) \qquad \begin{array}{l} \dfrac{d}{dx}Q(T) = -\dfrac{I^2}{A}\Lambda\dfrac{T(x)}{k(T)} \\ -\dfrac{d}{dx}Q(T) = \dfrac{I^2}{A}\Lambda T(x)\dfrac{A}{Q(T)}\dfrac{dT}{dx} \end{array}$$

integrating the (15) respect the unknown *x*:

$$(16) \qquad -Q(T)dQ = I^2\Lambda T(x)dT$$

Integrate the (16) between T_H = 300 K and T_L = 4.2 K, assuming that $Q_H = 0$, the result is:

$$Q_L{}^2 = I^2 \Lambda \left(T_H{}^2 - T_L{}^2 \right) \qquad (17)$$
$$\frac{Q_L}{I} = \sqrt{\Lambda \left(T_H{}^2 - T_L{}^2 \right)}$$

Substituting the values of T and Λ the result is:

$$(18) \qquad (Q_L)_{\min} = 46.9 \frac{W}{kA}$$

In the ideal vapour cooled all-metal current lead, is possible to obtain an approximated relationship similar to (18) [32]:

$$(19) \qquad (Q_L)_{\min} = I \sqrt{\Lambda T_L \frac{h_{fg}}{c_p}}$$

where h_{fg} is the latent heat of evaporation for the coolant and c_p is its specific heat.

A more complete analysis about the gas-cooled current leads was made by Wilson [33]. He solved the following equation:

$$(20) \qquad \frac{d}{dx}\left(k(T) A \frac{dT}{dx} \right) - f \dot{m} c_p \frac{dT}{dx} + \frac{I^2 \rho_{el}(T)}{A} = 0$$

where f is an empirical factor which takes into account the efficiency of the heat exchange and $\dot{m}$ is the mass flow of the cooling gas.

For gas-cooled leads, according to equation (20), a specific heat flux of 1.04 W/kA [34] results for the theoretical minimum for the heat flux in the helium bath.

4.3 General heat transfer equations

In Figure 4-3 is sketched the HTS part of a hybrid lead.

I considered the control volume sketched in Figure 4-4: the geometry is monodimensional and the Cartesian axes x is pointing to the lower temperature, that of the helium bath.

The general equation for the energy balance is written as:

$$(21) \qquad Q_{in} + Q_{gen} = \frac{dU}{d\tau} + Q_{out} + Q_{conv.}$$

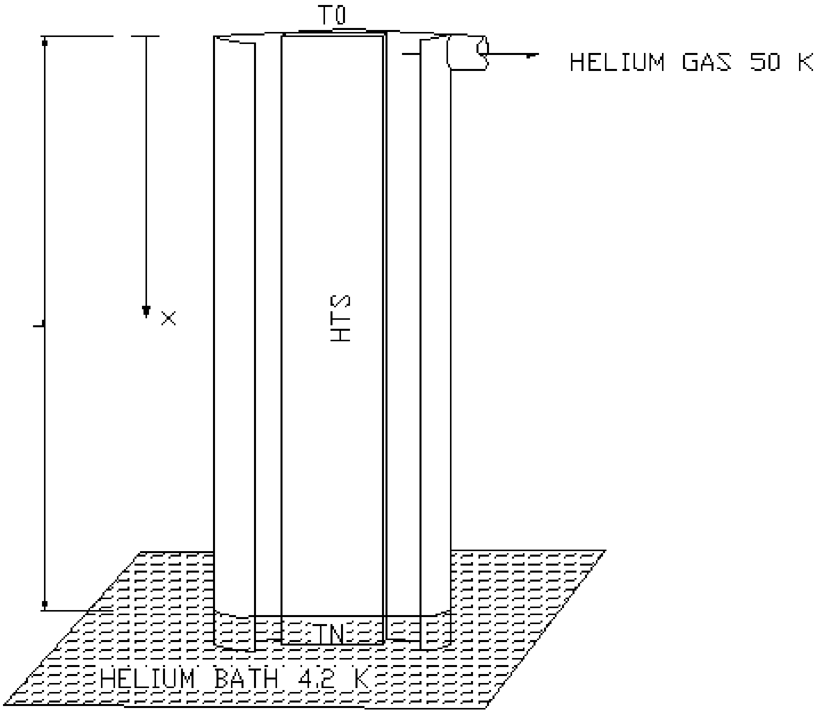

Figure 4-3. Scheme of the physical problem.

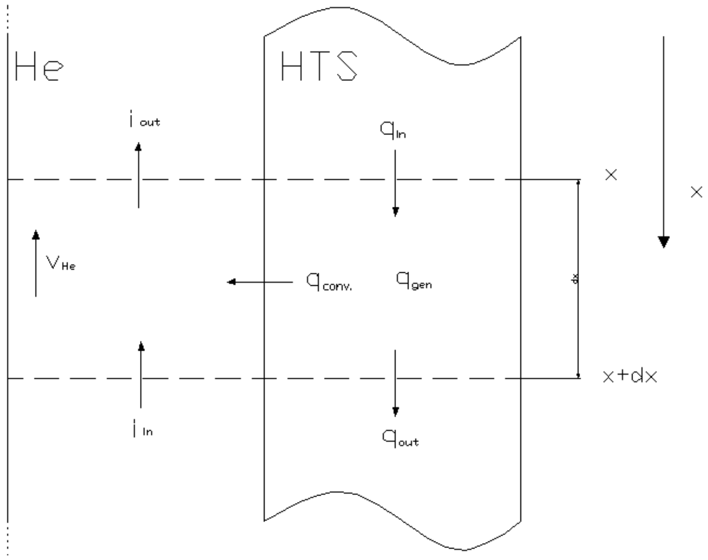

Figure 4-4. Energy balance.

For the HTS tape and according to the Fourier's equation [35] for the heat conduction, the single terms could be expressed as:

$$Q_{in} = -k(T)A\frac{\partial T}{\partial x}$$

$$Q_{out} = -A\left[k(T)\frac{\partial T}{\partial x} + \frac{\partial}{\partial x}\left(k(T)\frac{\partial T}{\partial x}\right)dx\right]$$

where *k(T)* is the coefficient of thermal conductivity and *A* the constant cross section of the tape.

The heat generation is due to the Joule’s heating and then:

$$Q_{gen} = q_v A dx = \frac{\rho_{el}(T)I^2}{A}dx$$

where $\rho_{el}(T)$ is the electrical resistivity of the tape and *I* the current flowing.

The term representing the convection heat exchange is:

$$Q_{conv} = h(T)C(T-\theta)dx$$

where *C* is the wet perimeter of the tape and *h(T)* is the coefficient of convection heat exchange.

Finally, the variation of the internal energy of the tape, upon an infinitesimal time interval is:

$$\frac{dU}{d\tau} = \nu c_p(T)A\frac{\partial T}{\partial t}dx$$

where ν is the density of the tape in kg/m^3 and c_p its specific heat.

According to the equation (21) the energy balance for the tape is:

$$-k(T)A\frac{\partial T}{\partial x} + q_v A dx = \nu c_p(T)A\frac{\partial T}{\partial t}dx - A\left[k(T)\frac{\partial T}{\partial x} + \frac{\partial}{\partial x}\left(k(T)\frac{\partial T}{\partial x}\right)dx\right] + h(T)C(T-\theta)dx \tag{22}$$

As regards to the helium cooling the tape similar considerations could be done. Due to the channel geometry, I considered the helium vapour to be at constant pressure. The enthalpy in *x* is, then, expressed as: $i_x = c_p(\theta)\theta_x$; where θ_x is the helium temperature in *x*.

The enthalpy balance across the helium control volume leads to, according to the (21):

$$h(T)C(T-\theta)dx + \dot{m}c_p(\theta)\left[\theta + \left(\frac{\partial\theta}{\partial x}\right)dx\right] = \nu c_p(\theta)A\frac{\partial\theta}{\partial t}dx + \dot{m}c_p(\theta)\theta_x \tag{23}$$

To notice that all the properties are now referred to helium.

In the helium vapour balance the term $\dot{m}c_p$ is called the *thermal capacity* of the cooling fluid and it is a crucial parameter for the cooling.

The helium vapour used to cool the tape comes from evaporation in the liquid bath. The mass flow of the helium vapour is expressed by:

$$(24) \qquad \dot{m} = \frac{k(T)A}{h_{fg}} \left(\frac{dT}{dx} \right) \Bigg|_{x=L}$$

where h_{fg} is the latent heat of evaporation for the helium.

Those equations constitute the system of partial differential equations to be solved in order to obtain the temperature profile of the HTS tape and helium gas. From the (22), (23) and (24) the systems of equations is:

$$(25) \qquad \begin{cases} \left(\nu c_p(T)A\right)_{HTS} \dfrac{\partial T}{\partial t} = A \dfrac{\partial}{\partial x}\left(k(T) \dfrac{\partial T}{\partial x} \right) - h(T)C\left(T - \theta\right) + \dfrac{\rho_{el}(T) I^2}{A} \delta \\ \left(\nu c_p(T)A\right)_{He} \dfrac{\partial \theta}{\partial t} = h(T)C\left(T - \theta\right) + \dot{m}\left(c_p(T)\right)_{He} \dfrac{\partial \theta}{\partial x} \\ \dot{m} = -\dfrac{k(T)A}{h_{fg}} \left(\dfrac{dT}{dx} \right) \Bigg|_{x=L} \end{cases}$$

and the initial conditions are: $\begin{cases} T(t=0,x) = T_{steady}(x) \\ \theta(t=0,x) = \theta_{steady}(x) \end{cases}$

To describe analytically the resistive transition of the superconductor, I introduced the function δ which depends on the tape's temperature:

$$(26) \qquad \delta(x) \begin{cases} = 1 \quad \text{if } \mathrm{T(x)} \geq \mathrm{T_{crit}} \\ = 0 \quad \text{if } \mathrm{T(x)} < \mathrm{T_{crit}} \end{cases}$$

The system is non-linear: the solution must be find numerically.

Before proceeding with the numerical computation I have to be sure of the existence of the solution of this problem.

All the material's properties are continuous function of temperature. Also the temperature profile is continuos because it is the profile of a finite and coherent tape. For the same reason *T* is limited and then also the material properties which depend on it.

The system of differential equation can be formally written:

$$\begin{cases} X' = f(t, X) \\ X(t_0) = X_0 \end{cases}$$

In the real analysis there is a theorem that assures if *f(t,X)* is continuos in a rectangle $\Omega=\{(t_a, t_b), (X_a, X_b)\}$ then the solution exists [36]. The theorem of uniqueness of solutions requires, for the solution to be unique, that *f(t,X)* is *Lipschitz continuos* in the variable X. A continuos function is Lipschitz continuos in a region Ω, if in that region its partial derivatives are continuos in the variables {X}. It is easy to verify that in this problem these hypotheses are satisfied and then the solution of (25) exist and it is unique.

4.4 Numerical scheme

The numerical solution of the previous equations is the only way I have to find a result. I developed a thermal model as close as possible to the real problem, and I took into account all the phenomena in order to have a model that well predict the behaviour of the superconducting assembly. In order to achieve it I reduced to the minimum the simplifications in the theoretical model: I consider the temperature dependence of the material's properties and I consider the case of a real heat exchange between the tapes and the helium gas.

I afford at first the solution of the steady case. It is the solution in the nominal working conditions and gives some interesting results for the lead design. Secondly, I solved the unsteady case. With this model it is possible to analyse the transient of the HTS and the quench propagation.

4.4.1 Steady state solution

In the steady case the time dependence of the temperature profile is ignored: the $\frac{\partial}{\partial t}$ term then cancels and, from equation (16), the new system of equation to solve is:

$$(27) \qquad \begin{cases} A\dfrac{\partial}{\partial x}\left(k(T)\dfrac{\partial T}{\partial x}\right) - h(T)C(T-\theta) = 0 \\ h(T)C(T-\theta) + \dot{m}\left(c_p(T)\right)_{He}\dfrac{\partial \theta}{\partial x} = 0 \\ \dot{m} = -\dfrac{k(T)A}{h_{fg}}\left(\dfrac{dT}{dx}\right)\Big|_{x=L} \end{cases}$$

The resistive term is not present because in the normal condition the HTS is below the T_c and then the δ factor, previously defined, is always $\delta = 0$.

For the numerical model I use the *finite difference* scheme for it is simple and, if the *central difference* method is performed it has a second order accuracy.

I decoupled the systems solving at first the equations relative to the temperature profiles for a given *"guess"* value of the mass flow. From this temperature profile I computed the respective value for the mass flow and I compared it with the *guess* one. Then I repeated the process until the two values were equal or less than a fixed small value.

For the equations of the temperature profiles, the finite difference approximation provides an algebraic equation at each grid node; it contains the variable value at that node as well as values at neighbouring nodes. It includes also some non-linear terms that require linearization. This leads to a system of linear algebraic equations of the following form:

$$(28) \qquad A_P T_P + \sum_l A_l T_l = Q_P$$

where P denotes the node at which the partial differential equation is approximated and index l runs over the neighbour nodes involved in finite difference approximations.

In order to solve the non-linearity, before solving this "real" system, i.e. with the material's property function of T, I solved analytically the system of equation considering the properties constant over all the range of temperature. This solution is not exact but it is close to the exact one and it is linear. I used this solution to solve the non-linearity due to the dependence of the material properties from the temperature. In fact I considered the properties of the HTS at the temperature given by the analytical solution: doing so I solved the non-linear system like if the properties do not depend on temperature.

For the numerical discretization, I used a uniform grid for the spatial term *x*: focusing our attention of the *i-th* value x_i I called x_{i+1} the one on its right and x_{i-1} the one on its left. The space between two consecutive nodes is $x_i - x_{i-1} = \Delta x = h$.

The difference approximation for the first derivative, using the central differencies, is [39]:

$$\frac{dT}{dx} = \frac{T_{i+1} - T_{i-1}}{2h} + o(h^2)$$

and for the second derivative:

$$\frac{d^2T}{dx^2} = \frac{T_{i+1} - 2T_i + T_{i-1}}{h^2} + o(h^2)$$

where h is the space discretization Δx, i represent the node at which the derivative is computed, as stated above.

According to this scheme the equations (27) become:

$$(29) \qquad \begin{cases} (k_{i+1} - k_{i-1}) \dfrac{T_{i+1} - T_{i-1}}{4\Delta x^2} + k_i \dfrac{T_{i+1} - 2T_i + T_{i-1}}{\Delta x^2} - \dfrac{Ch_i}{A}(T_i - \theta_i) = 0 \\ Ch_i (T_i - \theta_i) + \dot{m} c_{p_{He}} \dfrac{\theta_{i+1} - \theta_i}{\Delta x} = 0 \\ \dot{m} = -k_{end} A \dfrac{1}{h_{fg}} \left(\dfrac{T_{end} - T_{end-1}}{dx} \right) \end{cases}$$

The final matrix for the first two equations is:

$$(30) \qquad \begin{bmatrix} 8k_i + \alpha h_i & -\alpha hi \\ \dfrac{1}{1 + \dfrac{\beta}{h_i}} & -1 \end{bmatrix} \times \begin{bmatrix} T_i \\ \theta_i \end{bmatrix} = \begin{bmatrix} (T_{i+1} - T_{i-1})(k_{i+1} - k_{i-1}) + 4k_i (T_{i+1} - T_{i-1}) \\ -\dfrac{\beta}{\left(1 + \dfrac{\beta}{h_i}\right) h_i} \theta_i \end{bmatrix}$$

where $\alpha = \dfrac{4C}{A} \Delta x^2$ and $\beta = \dfrac{\dot{m} c_{p_{He}}}{C \Delta x}$

It is easy to notice that it has got the form described in equation (28).

This matrix has to be solved for each node *i*.

I took into account also the contact resistance at the end of the HTS, between the HTS and the Low-Temperature superconducting wires that are designed to connect the current leads to the bus-bars cable.

In this case the right term of the (29) becomes:

$$\begin{bmatrix} (T_{i+1}-T_{i-1})(k_{i+1}-k_{i-1})+4k_i(T_{i+1}-T_{i-1})+R_c I^2 4\Delta x^2 \dfrac{\delta}{A} \\ -\dfrac{\beta}{\left(1+\dfrac{\beta}{h_i}\right)h_i}\theta_i \end{bmatrix}$$

where R_c is the value for the contact resistance in *Ohm/m* and δ is a discrete function defined as:

$$\delta = \begin{cases} 0 \text{ if } \mathrm{i} \neq \text{end} \\ 1 \text{ if } \mathrm{i} = \text{end} \end{cases}$$

Once solved this system for a *guess* value of the mass flow $\dot{m}$, I need to iterate to find the $\dot{m}$ that satisfies the (27).

I solved the non-linearity due to the mass flow with iterations over the $\dot{m}$. I computed the temperature profile for two *guess* value of $\dot{m}$*:* called m_1 and m_2, and I used the first two equations of (27) to evaluate the temperature profile; using the third equation of (27) I evaluated the two $\dot{m}_c$*:* called m_{c1} and m_{c2} corresponding to the two temperature profile computed.

With a linear interpolation of the two couple of $\dot{m}$ and $\dot{m}_c$ I can find a new guess value, called $\dot{m}$. Using this value I evaluated the new temperature profile and, according to this, a new $\dot{m}_c$. Comparing these two values I can see if I found the $\dot{m}$ value that solves the system or not.

If it is not the convergence solution I solved again the system of the two first equations and again I found a new value of $\dot{m}_c$ corresponding to the new temperature profile.

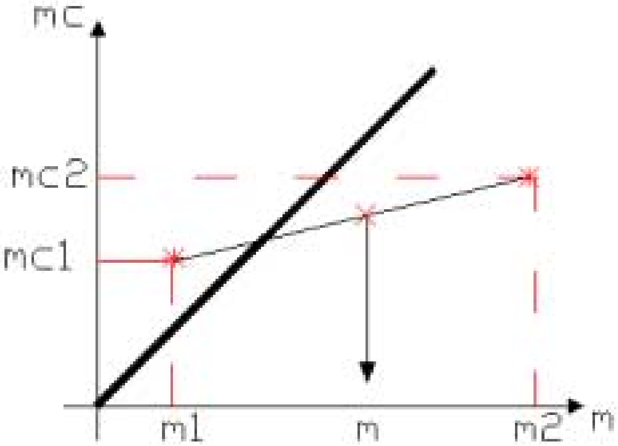

Figure 4-5. Mass flow function: with $\dot{m}$ I call the guess value for the mass and $\dot{m}c$ the calculated value according to the 3rd equation of the system reported above. At convergence $\dot{m} = \dot{m}c$. Since they are different I have to iterate. To seek the new value for the next iteration I perform a linear interpolation which gives a value closer to the ideal line. In this case the new guess values are *m1* and *m*.

The most common procedure is based on the difference between two successive iterates; the procedure is stopped when the difference, measured by some norm, is less than a pre-selected value. I choose the relative difference as criterion and I stopped the iterative process only when the relations:

$$\left|\frac{\dot{m}-\dot{m}_c}{\dot{m}}\right| \leq precision$$

was satisfied.

The value of the constant *precision* is set to 10^{-10}, i.e. close to the machine precision 10^{-16} for Matlab®.

The list of the code is reported in the appendix.

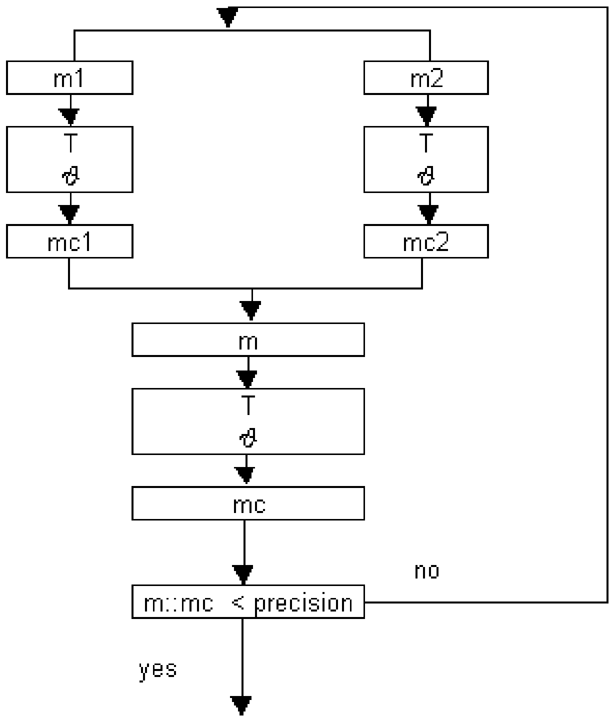

Figure 4-6. Flow chart of the mass iteration described above.

4.4.2 *Unsteady state solution*

Now I took into account the time dependence of the temperature profile of both the tape and the helium gas.

The equations are those reported previously:

$$(31)\quad \begin{cases} \left(\nu c_p(T)A\right)_{HTS}\dfrac{\partial T}{\partial t} = A\dfrac{\partial}{\partial x}\left(k(T)\dfrac{\partial T}{\partial x}\right) - h(T)C\left(T-\theta\right) + \dfrac{\rho_{el}(T)I^2}{A}\delta \\ \left(\nu c_p(T)A\right)_{He}\dfrac{\partial \theta}{\partial t} = h(T)C\left(T-\theta\right) + \dot{m}\left(c_p(T)\right)_{He}\dfrac{\partial \theta}{\partial x} \\ \dot{m} = -\dfrac{k(T)A}{h_{fg}}\left(\dfrac{dT}{dx}\right)\Bigg|_{x=L} \end{cases}$$

Considering now also the time dependence, I have a second coordinate direction to consider. One big difference respect to the spatial coordinate is that for the time one there is no backward influence. What happens during the time evolution depends only on the previous history of the transient.

For initial value problems, it is sufficient to consider the first order ordinary differential equation with an initial condition:

$$(32)\qquad \frac{dT(t)}{dt} = f\left(t, T(t)\right); \quad T(t_0) = T_0$$

The basic problem consists in finding the solution T a short time Δt after the initial point. The solution at $t_1 = t_0 + \Delta t$, T_1, can be regarded as a new initial condition and the solution can be advanced to $t_2 = t_1 + \Delta t$, $t_3 = t_2 + \Delta t$, etc…

The simplest methods can be constructed by integrating (32) from t_n to $t_{n+1} = t_n + \Delta t$:

$$(33)\qquad \int_{t_n}^{t_{n+1}} \frac{dT}{dt} dt = T^{n+1} - T^n = \int_{t_n}^{t_{n+1}} f\left(t, T(t)\right) dt$$

where I use the shorthand notation $T^{n+1} = T(n+1)$. This equation is exact. However, the right hand cannot be evaluated without knowing the solution so some approximation is necessary.

The mean value theorem of calculus guarantees that if the integrand is evaluated at the proper point $t = \tau$ between t_n and t_{n+1}, the integral is equal to $f(\tau, T(\tau))\Delta t$, but this is of little help since τ is unknown.

A good approximation is given by the *implicit* or *backward Euler* method [38]: using the final point in estimating the integral I obtain:

$$(34)\qquad T^{n+1} = T^n + f\left(t_{n+1}, T^{n+1}\right)\Delta t$$

With reference to stability, the method is called stable if it produces a bounded solution when the solution of the underlying differential equation is also bounded. The *implicit Euler* method is known [39] to be unconditionally stable, i.e. it produces bounded solutions for any time step if $\partial f(t,T)/\partial T < 0$.

I choose the *implicit Euler* because it produces smooth solutions even when Δt is very large while another implicit method like the *trapezoid rule* frequently yields solutions which oscillate with little damping. Consequently, the *implicit Euler* method tends to behave well, even for non-linear equations.

The equation system (31) then, becomes:

$$\begin{cases} \dfrac{\partial T}{\partial t} = \alpha\left[\dfrac{\partial k(T)}{\partial T}\left(\dfrac{\partial T}{\partial x}\right)^2 + k(T)\dfrac{\partial^2 T}{\partial x^2}\right] - \beta(T-\theta) + R_c\delta \\ \dfrac{\partial \theta}{\partial t} = \gamma(T-\theta) + \varepsilon\dfrac{\partial \theta}{\partial x} \\ \dot{m} = -k(T)A\dfrac{1}{h_{fg}}\left(\dfrac{dT}{dx}\right)_{x=L} \end{cases}$$

where:

$$\alpha = \frac{1}{(\nu c_p)_{HTS}} \qquad \gamma = \frac{Ch(T)}{(S\nu c_p)_{He}} \qquad R_c = \frac{\rho_{el} I^2}{(\nu c_p A^2)_{HTS}}$$

$$\beta = \frac{Ch(T)}{(A\nu c_p)_{HTS}} \qquad \varepsilon = \frac{\dot{m}}{(\nu S)_{He}}$$

and δ is the discrete function defined as:

$$\delta\begin{cases} 1 \text{ if } \mathrm{T} \geq \mathrm{T}_{\mathrm{lim}} \\ 0 \text{ if } \mathrm{T} < \mathrm{T}_{\mathrm{lim}} \end{cases}$$

Applying the *Euler* scheme:

$$\begin{cases} \dfrac{T_i^{n+1} - T_i^n}{\Delta t} = \alpha(k_{i+1} - k_{i-1})\dfrac{T_{i+1}^{n+1} - T_{i-1}^{n+1}}{4\Delta x^2} + \alpha k_i \dfrac{\left(T_{i+1}^{n+1} - 2T_i^{n+1} + T_{i-1}^{n+1}\right)}{\Delta x^2} - \beta\left(T_i^{n+1} - \theta_i^{n+1}\right) + R_c\varepsilon \\ \dfrac{\theta_i^{n+1} - \theta_i^n}{\Delta t} = \gamma\left(T_i^{n+1} - \theta_i^{n+1}\right) + \delta\dfrac{\theta_{i+1}^{n+1} - \theta_i^{n+1}}{\Delta x} \\ \dot{m} = -k_{end}\dfrac{A}{h_{fg}}\left(\dfrac{T_{end}^{n+1} - T_{end-1}^{n+1}}{\Delta x}\right) \end{cases}$$

If I assume:

$$r = \frac{\alpha\Delta t}{\Delta x^2} \qquad d = \frac{\varepsilon\Delta t}{\Delta x}$$

Then, rearranging and substituting the terms of the previous equations, according to those new definitions, I obtain:

$$\begin{cases} T_{i-1}^{n+1}\left(\dfrac{r}{4}(k_{i+1} - k_{i-1}) - rk_i\right) + T_i^{n+1}(1 + 2rk_i + \beta\Delta t) - T_{i-1}^{n+1}\left(\dfrac{r}{4}(k_{i+1} - k_{i-1}) + rk_i\right) - \beta\Delta t\theta_i = T_i^n + R_c\delta\Delta t \\ -T_i^{n+1}\gamma\Delta t + \theta_i^{n+1}[1 + \gamma\Delta t + d] - d\theta_{i+1}^{n+1} = \theta_i^n \\ \dot{m} = -k_{end}\dfrac{A}{h_{fg}}\left(\dfrac{T_{end}^{n+1} - T_{end-1}^{n+1}}{\Delta x}\right) \end{cases}$$

Then, as previously done for the steady case I solved at first the two equations for the temperature profile and then I iterated over the mass ratio for T and θ are function of $\dot{m}$.

As regards the temperature profile's equations I can write, in matrix form:

$$\begin{bmatrix} f(T)_{HTS} & f(\theta)_{HTS} \\ f(T)_{He} & f(\theta)_{He} \end{bmatrix} \begin{bmatrix} T \\ \theta \end{bmatrix}^{n+1} = \begin{bmatrix} T \\ \theta \end{bmatrix}^{n} + \begin{bmatrix} R_c \delta \Delta t \\ 0 \end{bmatrix} \qquad (35)$$

$$[M][X] = [B]$$

The matrix M is a n x n tridiagonal-shaped matrix where n is two times the number of nodes of the spatial discretization. The first block on the first row of M represent the term for T^{n+1} taken from the first equation of the system; the second block of the first row is the term regarding θ^{n+1} from the same equation; the first term of the second row is the term relative to T^{n+1} taken from the second equation of the system and the second one is the term for θ^{n+1} taken from the same equation.

The matrix B represents the terms relative to T^n: that is at the previous step time.

In the following plot there is a sketch of the matrix M:

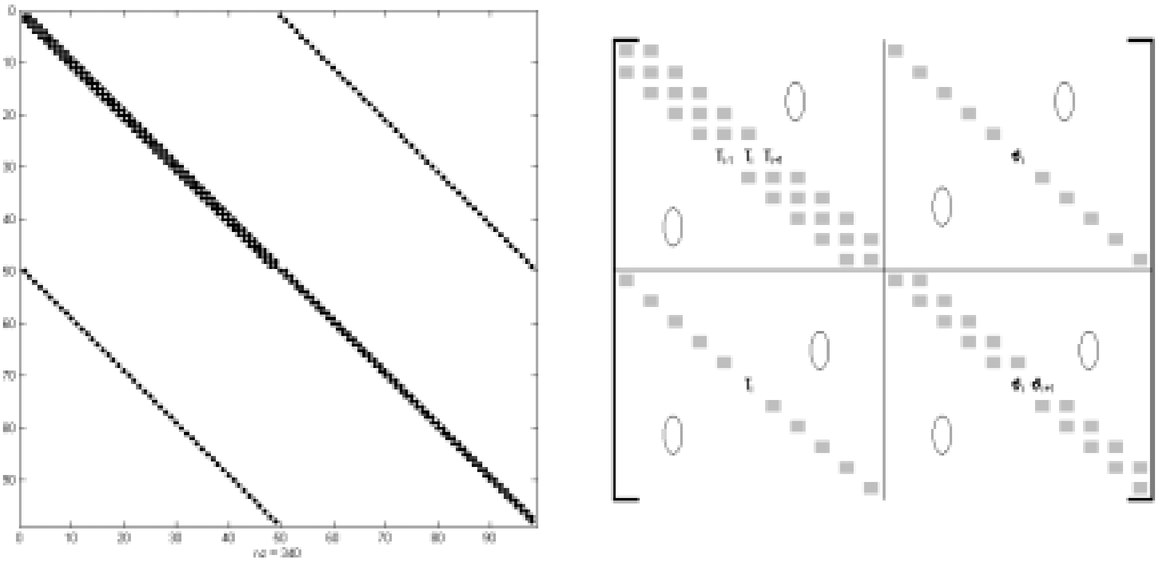

Figure 4-7. Non-zero elements of the tridiagonal matrix M.

The term B really is a vector containing the terms on right hand side of the system of equations. It contains also the border conditions, that is the temperature of the assembly at the cold and warm end.

The equations for the temperature profile can be rewritten, for the first and the last node, like follows:

$$\begin{cases} T_1^{\,n+1}\left(1+2rk_1+\beta\Delta t\right)-T_2^{\,n+1}\left(\dfrac{r}{4}\left(k_2-k_0\right)+rk_1\right)-\beta\Delta t\theta_1=T_1^{\,n}+R_c\delta\Delta t+T_0\left(\dfrac{r}{4}\left(k_2-k_0\right)-rk_1\right) \\ -T_1^{\,n+1}\gamma\Delta t+\theta_1^{\,n+1}\left[1+\gamma\Delta t+d\right]-d\theta_2^{\,n+1}=\theta_1^{\,n} \end{cases}$$

$$\begin{cases} T_{end-1}\left(\dfrac{r}{4}\left(k_N-k_{end-1}\right)-rk_{end}\right)+T_{end}^{\,n+1}\left(1+2rk_{end}+\beta\Delta t\right)-\beta\Delta t\theta_{end}= \\ \qquad\qquad =T_N^{\,n+1}\left(\dfrac{r}{4}\left(k_N-k_{end-1}\right)+rk_{end}\right)+T_{end}^{\,n}+R_c\delta\Delta t \\ -T_{end}^{\,n+1}\gamma\Delta t+\theta_{end}^{\,n+1}\left[1+\gamma\Delta t+d\right]=d\theta_N^{\,n+1}+\theta_{end}^{\,n} \end{cases}$$

Where T_0 and T_N are the temperature, respectively, at the warm and at the cold end of the assembly; θ_N is the temperature of the liquid helium that is fixed.

To solve the non-linearity due to the material properties I referred them to the temperature of the previous time step. It is not worth iterating over the properties, to refer them to the present time step, from the accuracy point of view.

4.4.2.1 Simulation of quench propagation

The main goal of the model is, as it was said, to study the behaviour of the HTS when quench occurs. With this model it is possible to simulate the resistive transition in a situation really close to that we will have in the current leads of the LHC.

To simulate experimentally a quench we warmed up the top end of the current lead's assembly until when it reached the transition temperature, T_c.

In the numerical code I develop a routine to simulate the warm up of the upper part of the lead. What I did was to increase the value of the fixed temperature T_0, with a rate that could be fixed each time. This temperature is one of the border conditions of the problem: by varying its value I obtained, at each time step, a new temperature profile for the initial condition of the problem.

Once reached the transition temperature the quench happened and I study its time evolution. There are two possible situations: the first one is when the quench does not propagate: it happens if the heat transmitted through the lead is larger than that generated by the resistive zone; the second one is when the quench propagates.

In the first case a thermal balance is necessary and I will do it in the next paragraph. In the second case, it is our interest to find a solution to stop the transition process before a too high temperature could damage the HTS. The protection system developed for the current leads cuts the power supply in case of quench detection. Starting from then the lead has to withstand the discharge of the magnet whose time constant depends on the inductance and the resistance of the electrical circuit.

The task is to find a quench-detection parameter which allows to cut off the current in safety condition: during the transient the temperature of the lead has to remain under control and always below a fixed temperature limit considered acceptable for the HTS' safety.

In my model I computed, at each time step, the value of the total voltage drop across the HTS. Then I fixed a limit value, V_{lim} above which I switched off the current and I simulate the discharge of the magnets with an exponential decay of the current with a time constant τ. The expression of the exponential decay is:

$$(36) \qquad I(t) = I_0 e^{-\frac{t}{\tau}}$$

Varying the value V_{lim}, I obtained different temporal evolution of the transient: it is possible, then, to choose a value that allows to operate safely even if quench occurs.

This value has to be adequate with the technological limits imposed by the protection systems. Sometimes too small values could be not detectable because of the electrical background-noise in the LHC tunnel. It is to remember that the current leads will be installed in an extremely complex machine where all the systems have to work in harmony with the others. If a too small value of V_{lim} is required, I can solve the problem considering the *integrated signal* of the voltage drop. Instead of fixing a limit value of the voltage drop I fixed a value for the integrated value of the voltage drop over a time interval *t*. Then, by integrating the voltage drop at each time step, I can compare, every *t* seconds this value with the limit one.

4.4.2.2 Minimum propagation zone

Once started, the quench propagates only if the heat generated by the resistive zone is larger than the heat transferred along the tape. In this case the temperature of the resistive zone keeps increasing: because of the thermal conduction also the temperature of the neighbouring regions starts to increase and the resistive transition propagates. The phenomenon can be stopped only reducing the current.

The main parameter which determines the propagation of quench is the length of the resistive zone. A basic thermal balance on the HTS allows to evaluate the minimum value of the resistive length which leads to quench propagation: this length is the *minimum propagation zone* (MPZ) [40].

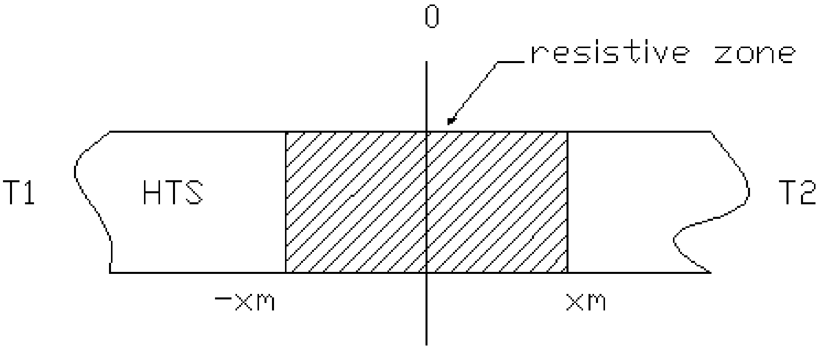

Figure 4-8. Control volume for the thermal balance.

For this purpose I consider a control volume on the HTS. As first rough approximation I consider only the thermal conduction as mechanism of heat exchange for the tape.

The thermal equations, in the superconducting and in the resistive case, are respectively:

$$\begin{aligned} &Ak\frac{d^2T}{dx^2}+\frac{\rho_{el}I^2}{A}=0 \quad \text{if } \mathrm{T}\geq \mathrm{T_c} \\ &Ak\frac{d^2T}{dx^2}=0 \quad \text{if } \mathrm{T}<\mathrm{T_c} \end{aligned} \tag{37}$$

I suppose the material's properties to be constant in the range of temperature I am using.

I will apply the first equation to the hatched region of Figure 4-8, while the second one will be used for the rest of the control volume. In $x = \pm x_m$ the temperatures from the two different equations have to be equal as well as their first derivative, in order to assure the continuity of the control volume's temperature profile.

For a small range of temperature around the critical one, I can consider the thermal conductivity independent from temperature, then the integral of the first equation in (37) is:

$$\int \frac{d^2T}{dx^2}dx=-\frac{\rho_{el}I^2}{kA^2}x+C_1$$

$$T(x)=-\frac{\rho_{el}I^2}{kA^2}\frac{x^2}{2}+C_1x+C_2$$

In a symmetric control volume with internal generating heat the temperature profile is parabolic: in this approximation the first derivative of the temperature in $x = 0$, must be zero. In this way C_1 cancels; to determine C_2 I know that the temperature in $x = x_m$ is $T = T_c$. the final result is, then:

$$T(x) = \frac{\rho_{el} I^2}{2kA^2}\left(x_m{}^2 - x^2\right) + T_c \tag{38}$$

Similarly I solve the second equation of (37) and I get:

$$T(x) = C_1 x + C_2$$

In this case the first derivative of T(x), in a pure conduction problem, is set to be equal to:

$$-\frac{Q_{conduction}}{kA} = \frac{T_2 - T_1}{L}$$

For $x = x_m$ is $T = T_c$ as previously said. Substituting the values of two constants, the final solution for this case is:

$$T(x) = T_c + \frac{Q}{kA}\left(x_m - x\right) \tag{39}$$

Now, applying the condition of continuity of the two temperature profile:

$$\left(\frac{dT_{hatched}}{dx}\right)_{x=x_m} = \left(\frac{dT_{non-hatched}}{dx}\right)_{x=x_m}$$

$$x_m = \frac{2QAfu}{\rho_{el} I^2} = MPZ \tag{40}$$

This is a first estimation of the *MPZ*. In the numerical model it will be sufficient to warm up the HTS over a length larger than x_m in order to be sure to have propagation.

In my thermal model, the simplifications used in the MPZ estimation are not valid because several reasons. First of all the shape of the temperature profile. In the current lead assembly the tapes are subjected to a temperature gradient. Around the resistive region, then, the shape of the profile is not necessary symmetric as I supposed even if the shape is parabolic.

Then the MPZ is a function of the peak of temperature in the resistive region, also. During a heating transient, the real value of x_m could be different than the computed one in relation to the heating parameters. Anyway this value gives a good estimation of what it should be.

In my thermal model I chose a value of the heating region larger enough than MPZ in order to assure propagation. Now, the only responsible of quench propagation is the local temperature reached.

The list of the code is reported in the appendix.

4.4.3 *Stability and convergence of the numerical method*

A discretization scheme is said to be unstable or wiggling if its nodal solution to a steady-state equation exhibits oscillatory behaviour or if its nodal solution to a transient equation starts being oscillatory and gradually grows unbounded.

As regards stability, in my model I used the *implicit Euler* scheme that is unconditionally stable.

From a theorem of the numerical analysis [39] is known that the matrix M is said *well conditioned* if its *condition* number κ is close to one. The definition for the *condition* number is:

$$\kappa_i(M) = \|M\|_i \|M^{-1}\|_i \qquad (i = 1, 2, \infty) \tag{41}$$

Where the index i determines the kind of norm we are using:

$$\|M\|_1 = \max_i \sum_j |m_{ij}|$$
$$\|M\|_2 = \sqrt{\rho(M^T M)}$$
$$\|M\|_\infty = \max_j \sum_i |m_{ij}|$$

$\rho(M)$ is the *spectral radius* of the matrix, i.e. its maximum eigenvalues.

Now, called T^* the exact solution, $T^\wedge$ the computed one and $r = B - MT^\wedge$, using:

$$AT = B$$
$$AT^* - AT^\wedge = B - (B - r) = r$$
$$\|T^* - T^\wedge\| = \|A^{-1} r\| \le \|A^{-1}\| \|r\|$$

it is not difficult to find this relationship for the condition number κ:

$$\frac{\|T^* - T^\wedge\|}{\|T^*\|} \le \kappa(M) \frac{\|r\|}{\|B\|} \tag{42}$$

That means that, if κ is small, the effect of rounding or experimental errors in the elements of the matrix, are bounded by a small value.

The most used is κ_2 and for my system $\kappa_2 \sim 2$. Then a fairly well conditioned matrix.

With reference to the convergence of the numerical method it is more difficult to demonstrate for the model is non-linear. Non linear problems are strongly influenced by boundary conditions and grid sizes.

Therefore convergence is usually checked using numerical experiments, i.e. repeating the calculation on a series of successively refined grids.

A numerical method is said *convergent* if the solution of the discretized scheme tends to the exact solution of the differential equation as the grid spacing tends to zero.

If the method is stable and if all the approximations used in the discretization process are consistent, we usually find that the solution does converge to a *grid-independent* solution.

In my model I used a *central difference* scheme for the *x*-discretization. This is a second order scheme: the error is reduced by two orders of magnitude when the grid spacing is reduced one order of magnitude. Instead, for the time equation, the *implicit Euler* scheme is a first order scheme.

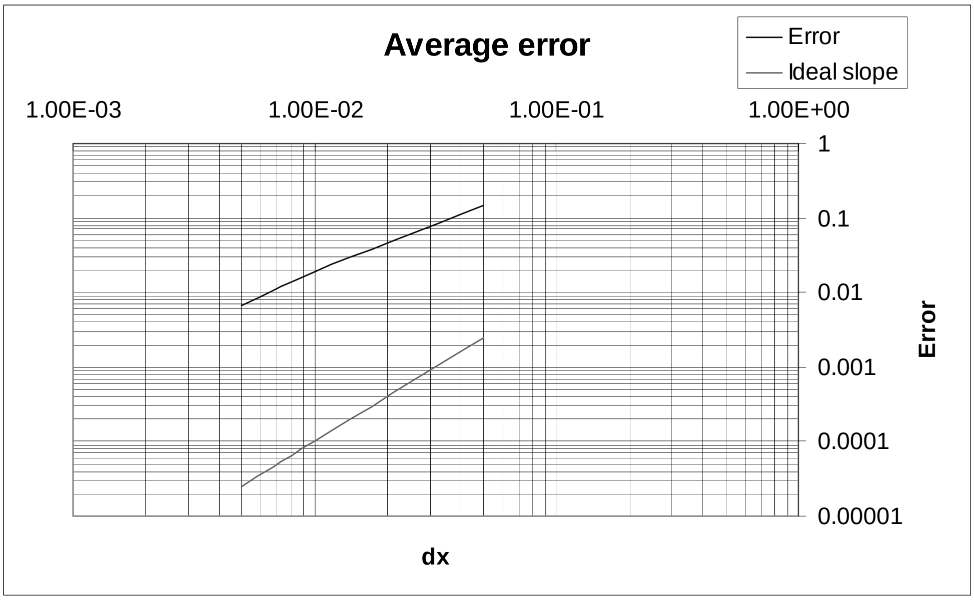

Figure 4-9. Average error for the evaluated heat flow in the solution of the steady case. The scheme is of the second order as it is expected.

Analysing the convergence of the model it is possible to make some considerations on the grid spacing and the time resolution. The numerical scheme is *consistent*: as the grid spacing approaches to zero the solution tends to the exact one.

Decreasing the grid spacing means to increase the computational cost and the time necessary to find out a solution.

I run the code with different grid spacing. The result is reported in Figure 4-9.

As we see, using a grid spacing *dx* = 5 mm instead of 1 mm, the relative difference between the solution is about 0.6%. The grid step I used in the model was, then, *dx* = 5 mm that is a good compromise.

As regards the unsteady solution I did the same procedure for the time step, assuming a fixed spatial step *dx* =5 mm.

The scheme is a first order scheme, as it was expected.

In the model I used a temporal resolution of 0.1 s, that is a good compromise between computational cost and relative precision of the solution.

For smaller time step the relative difference between the two solutions tends to really small values.

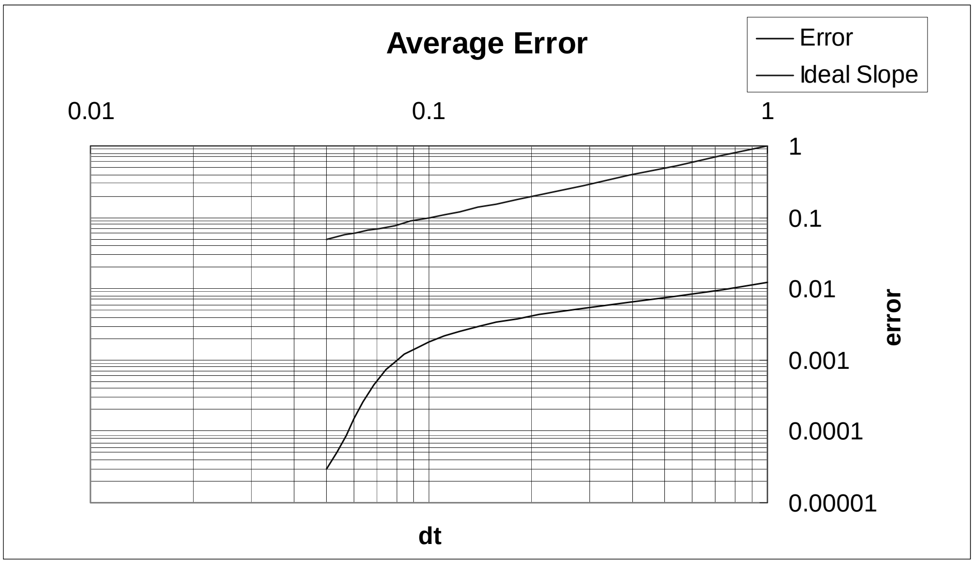

Figure 4-10. Average error in the maximum temperature for the transient model. The spatial grid spacing is 5 mm.

5 *Material's properties*

Before approaching the numerical solution it is necessary to have a look on the material's properties I will use in the thermal model and to consider whether or not one can simplify the model adopting constant properties in the range of temperature of my interest.

5.1 Helium

As said above the liquid helium into which are dipped the tapes has a constant temperature of 4.5 K (pressure = 1.3 bar). The helium that evaporates due to the tapes conduction is used to cool down the current leads' assembly. The helium's phase diagram is shown in Figure 5-1.

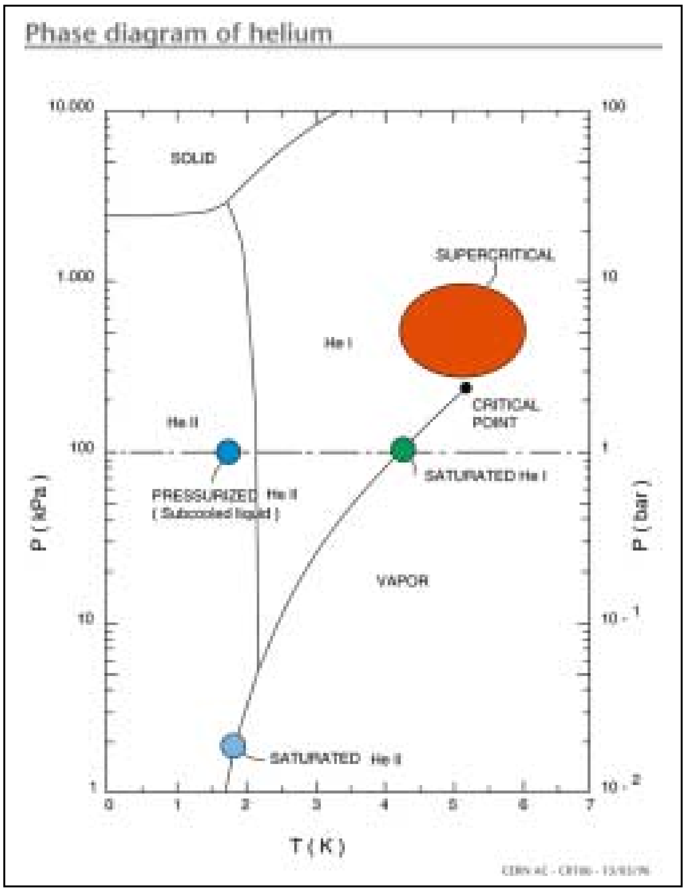

Figure 5-1. Phase diagram.

In normal conditions the range of temperature for the helium cooling the HTS part of the leads is between 4.5 and 50 K.

According to the equations previously reported, to the purpose of the thermal model it is necessary to know the specific heat, the density and the latent heat of evaporation of helium in order to proceed to the evaluation of the temperature profile.

The density of helium in the range 4.5 – 300 K is reported in Figure 5-2 [41]:

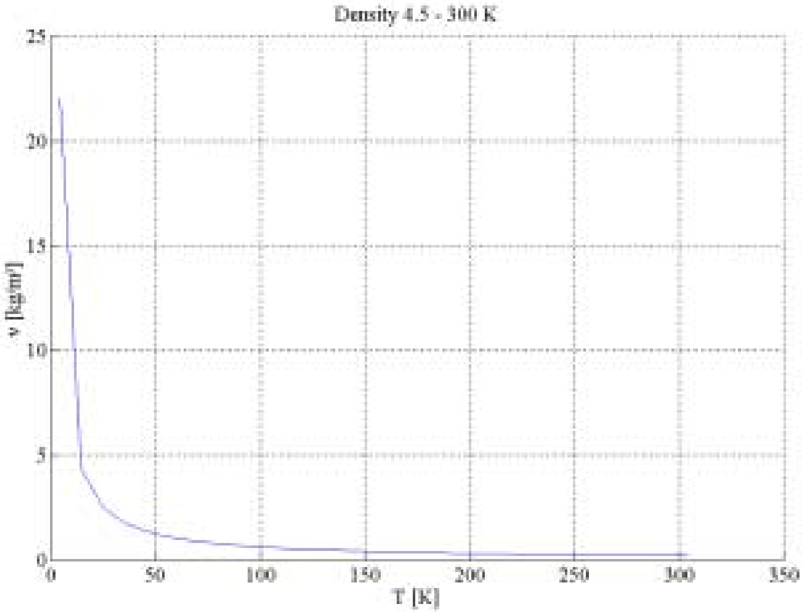

Figure 5-2. Density of helium.

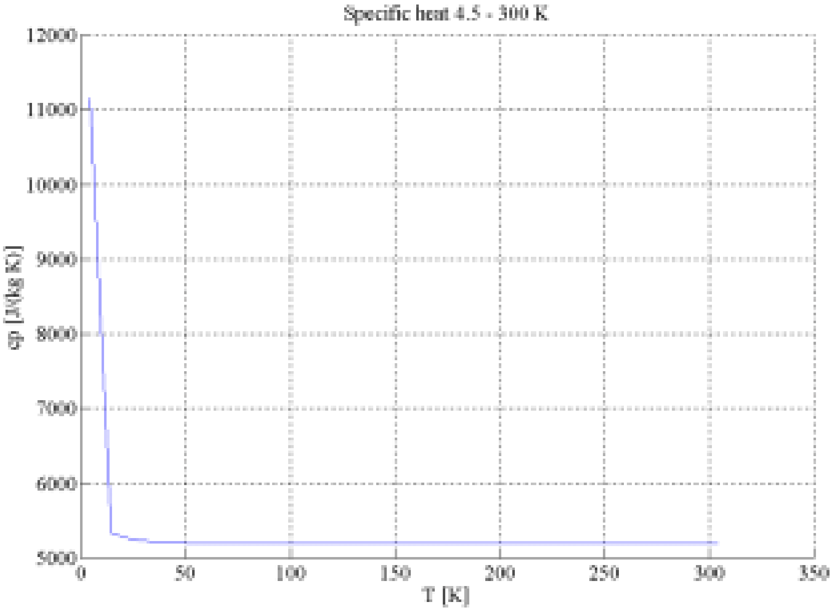

Figure 5-3. Specific heat.

The working temperature is between 4.5 and 50 K: in this range the mean value is ν = 3.6037 kg/m³. Since the temperatures of the two ends of the tapes are fixed, as we see from the graph the mean value is a rather good approximation also during the quench transient, due to the range of temperature in which it works.

The specific heat of helium is reported in Figure 5-3. In the range 4.5 – 50 K the mean value is ρ = 5.412 kJ/kg/K, that is a good approximation for the thermal model.

The latent head of evaporation for the liquid helium at 4.5 K is [42,43]: h_{fg} = 23000 J/kg .

The last unknown is the coefficient of heat convection *h* for helium. It depends on the type of flow of the helium gas. Guessing as first approximation a linear temperature profile between 4.5 and 50 K, the number of Reynolds, characterising the type of flow, is reported as a function of the cooling channel diameter in Figure 5-4. Since the transition between *laminar* and *turbulent* flow occurs for Reynolds bigger than 2500 [44] in our case the flow is undoubtedly laminar.

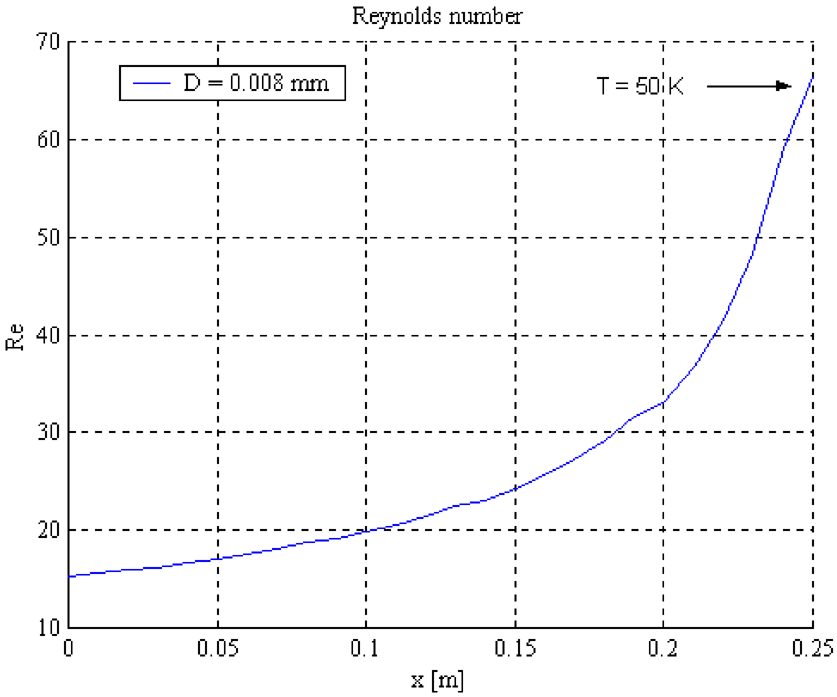

Figure 5-4. Reynolds' number as a function of the channel's diameter.

The equivalent diameter used is a guess value: it will be checked later, after the definition of the geometry. Anyway the N_{Re} is so low that a different value for the channel diameter will not influence the type of flow that is laminar.

The simplest correlation for the thermal convection coefficient is the one for the laminar flow with constant wall temperature [see also 45]:

$$(43) \qquad Nu = 3.656$$

Nu is the Nusselt's number and is equal to:

$$Nu = \frac{hD}{k}$$

where D is the equivalent diameter: $D = \frac{4A}{C}$, A is the cross section, C the wet perimeter

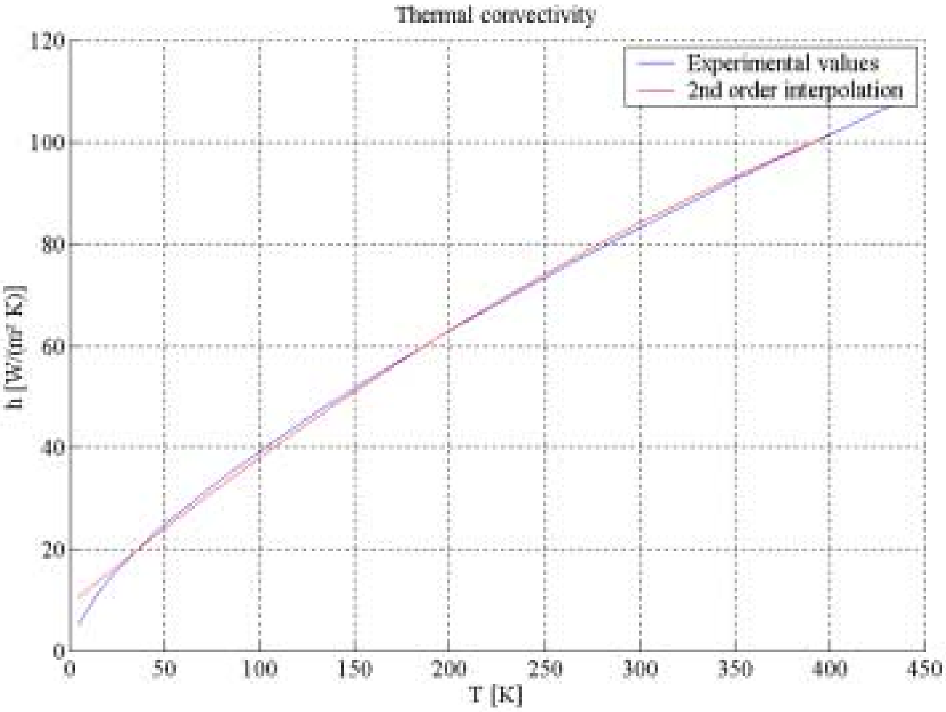

and k the thermal conductivity of helium.

Using the (43) for the evaluation of *h(T)* the result is:

Figure 5-5. Coefficient of thermal convection.

Another correlation for the evaluation of the h value is the one for the laminar flow in self-cooling condition [46]:

$$(44) \qquad Nu = 0.12(\Pr \cdot Gr)^{\frac{1}{3}}$$

$\Pr = \frac{c_p \mu}{k}$ Prandtl's number, where c_p is the specific heat, μ the dynamic viscosity and k the thermal conductivity of the gas.

$Gr = \frac{g\beta\Delta T}{\nu^2} D^3$ Grashof's number, where g is the gravity acceleration, β is the dilatation coefficient of the gas $\beta = -\frac{1}{\rho}\frac{\rho - \rho_\infty}{T - T_\infty}$ where the subscript ∞ means the value out of the boundary-layer, ν the cinematic viscosity (μ/ρ) and D the equivalent diameter.

ΔT, the temperature difference between the coolant and the tape, is unknown. For a first approximation I suppose the ΔT could vary between 1 and 20 K. According to these hypotheses the two possible results for the mean *h* are:

ΔT	Gr	Nu	$\langle h\rangle_{mean}$ [W/m²/K]
1	$39\ 10^3$	3.62	13.9
20	$1.44\ 10^6$	5.63	21.69

It is correct to suppose that the right value of *h* will fall between these values. The mean value of the convection coefficient according to (43) is *h* = 17.3 W/m²/K. The approximation used with (43) is then valid and can be used without committing any error.

As shown in Figure 5-5 the second order interpolation well follows the shape of the plot: I will use this interpolation for the *h* values on the numerical code instead of a mean-value approximation that is not careful in this case.

5.2 Superconducting tapes

As stated above the superconducting tapes are made of a silver-gold matrix, which works like a protection shunt and as mechanical support. The superconducting oxide is inside the metal matrix.

According to the equation (16) the material's properties I need are: the density of the tape, its specific heat, the coefficient of thermal conduction and the electrical resistivity.

Due to the composite nature of the tapes their properties could be estimated as a linear combination of the properties of each constituent.

If I designate with *fu* the filling factor of a tape: $fu = \frac{A_{HTS}}{A}$, that is the ratio of the superconducting oxide's cross section over the total one, the equivalent property of the tape could be written as:

$$(45) \qquad x_{eq} = x_{HTS} \cdot fu + x_{AgAu} \cdot (1 - fu)$$

The value of *fu* for the tapes I deal with in this work is *fu* = 0.27.

As regards the material's density, due to the large amount of metal in the tape, it is not trivial to use the density of the alloy as the one of the whole tape, that is $\rho = 10.34\ 10^3$[kg/m³] [47].

5.2.1 Specific heat

From the (45) it is evident I can write the expression for the specific heat, $c_p(T)$, of the tapes as:

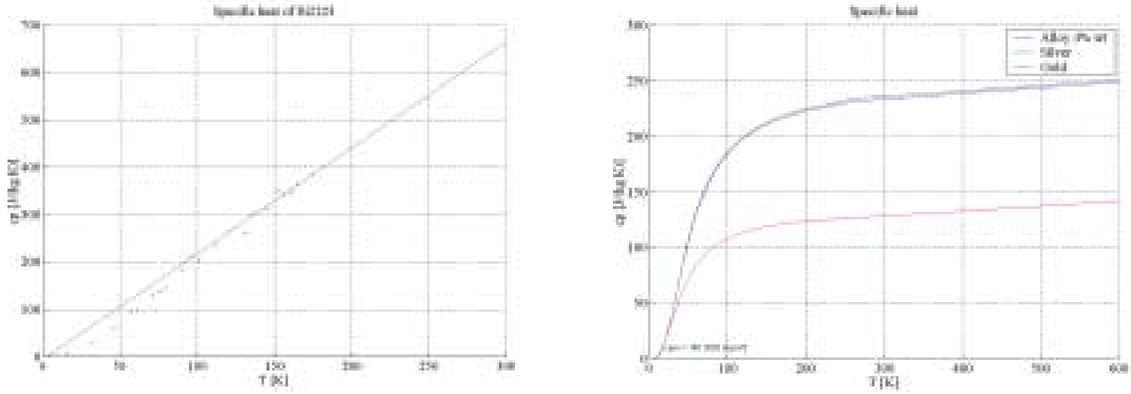

Figure 5-6. Specific heat for the oxide and the metal alloy.

$$c_{peq}(T) = c_{pHTS}(T) \cdot fu + c_{pAgAu}(T) \cdot (1 - fu)$$

In Figure 5-6 there are: $c_{p\ HTS}$ [48] and $c_{p\ AgAu}$ [49] for an alloy with an Au content of 4 % wt.

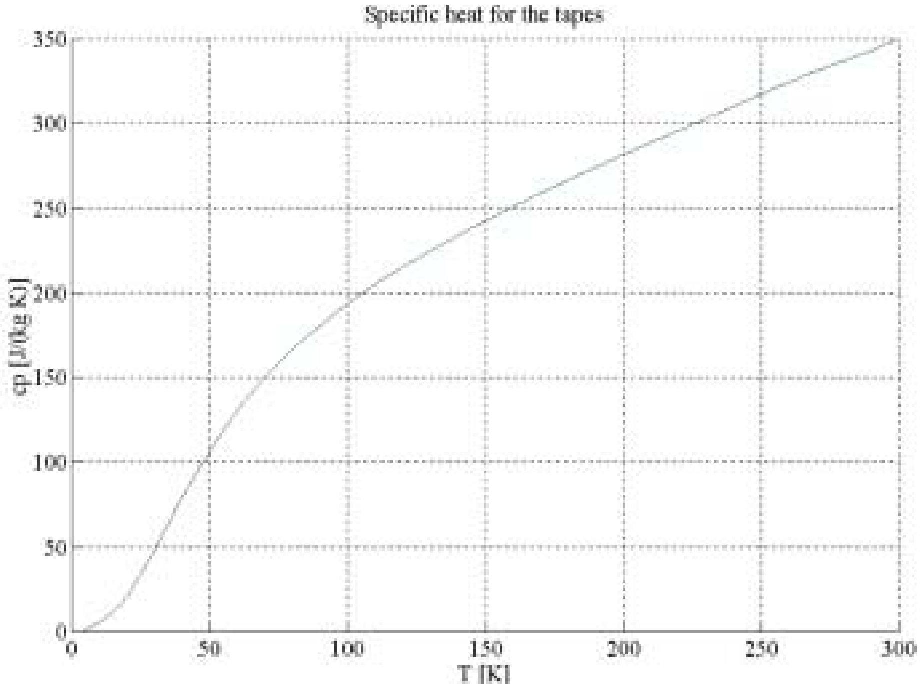

Figure 5-7. Equivalent specific heat for the superconducting tapes.

For the oxide superconductor a linear interpolation is the best approximation. As regards the silver alloy the importance of gold in the evaluation of c_p is negligible, anyhow it will be taken into account.

The plot of the equivalent specific heat for the tape is reported in Figure 5-7 for a *fu* = 0.27 as previously said.

Over the range of temperature 4 – 400 K it varies significantly and use of a mean value could lead to some errors in the evaluation.

5.2.2 Thermal conductivity

The thermal conductivity of the tapes, *k(T)*, could be evaluated using the (45) as:

$$k_{eq}(T) = k_{HTS}(T)\cdot fu + k_{AgAu}(T)\cdot(1-fu)$$

Using a *fu* of 0.27 and a silver alloy with 4 % wt of gold [50], one obtains an equivalent thermal conductivity as shown in Figure 5-8.

As previously said the alloying with gold allows to significantly reduce the thermal conductivity especially at low temperature (Figure 5-9) and then permits to limit the heat inleak into the liquid bath.

Also in this case the contribution of the oxide superconductor is really small and could be neglected.

Anyway the shape of the plot is rather changed by the presence of the oxide and I will take it into account.

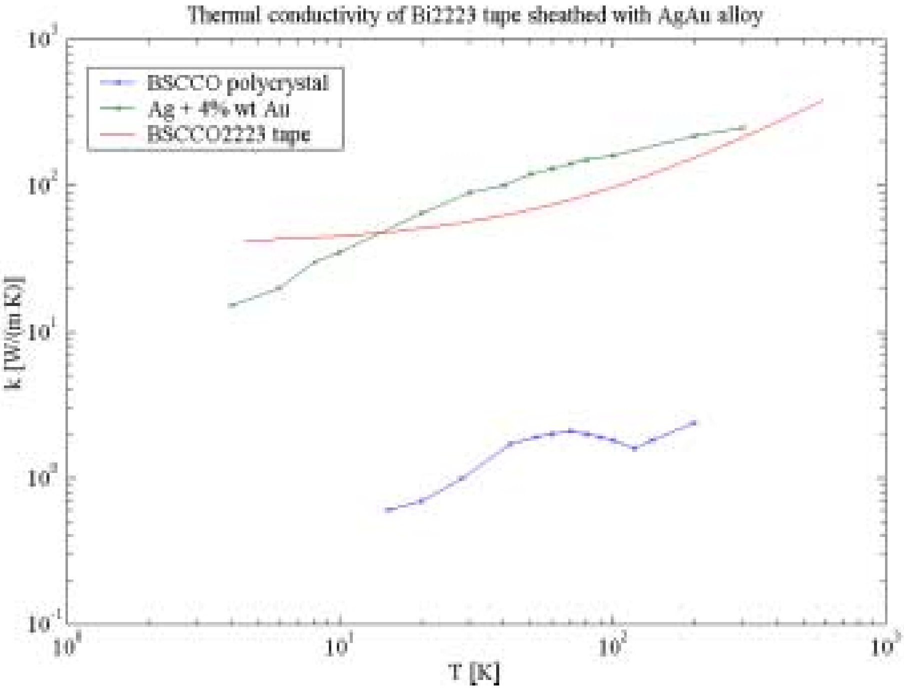

Figure 5-8. Equivalent thermal conductivity for a filling factor *fu* = 0.27.

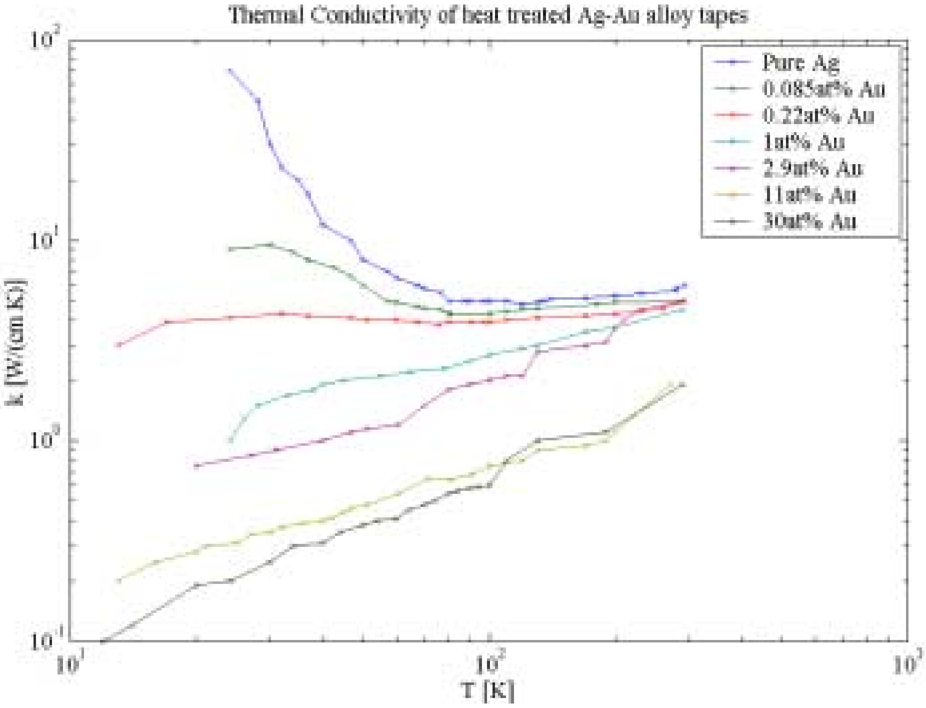

Figure 5-9. Thermal conductivity as a function of Au alloying.

The dependence of the thermal conductivity from temperature cannot be ignored: also in the superconducting state the gradient of temperature draw in a strong variation of *k(T)* that has to be considered.

5.2.3 Electrical resistivity

From an electrical point of view the oxide superconductor and the metal matrix are two conductors connected in parallel. Named R_{AgAu} the resistance of the AgAu matrix and R_{HTS} the one of the internal oxide, the equivalent electrical resistance, R_{eq} is equal to:

$$(46) \qquad R_{eq} = \left(\frac{R_{HTS} R_{AgAu}}{R_{HTS} + R_{AgAu}} \right)$$

From the Ohm's equations the resistance is $R = \rho \frac{L}{A}$ where L is the length of the conductor, A its cross section and ρ is the electrical resistivity.

The graph of ρ(T) for the Ag-Au alloy as a function of the atomic Au percentage is reported in the following figure [50].

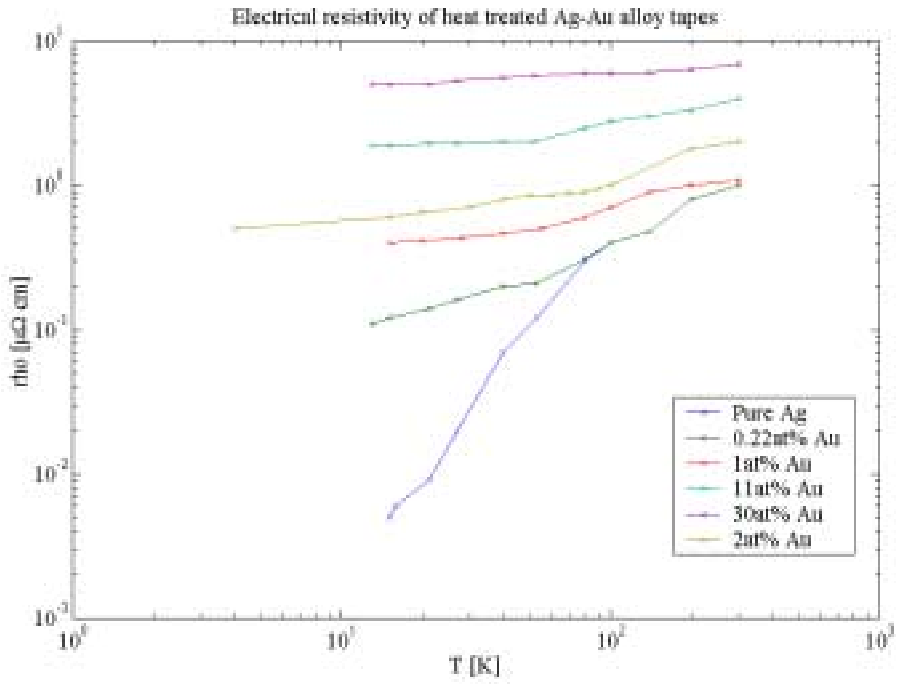

Figure 5-10. Electrical resistivity for AgAu alloys.

Adding gold to the silver is advantageous from the point of view of the thermal inleak, but not as regards to the electrical properties as it is evident from the previous picture.

The dependence of the resistivity from the temperature, also if less emphasised than the case of the thermal properties, is still remarkable and then it will be taken into consideration in the numerical code.

Dealing with the superconducting material this dependence is more marked. As it was described in the chapter dedicated to the theory of superconductivity, these materials show a zero electrical resistivity for temperature lower than the critical one, T_c; above this temperature they show resistivity bigger than those of normal metals.

Differently from the Low-Temperature-Superconductors (LTS) the HTSs exhibit a wide transition from the superconducting to the normal state and it has to be taken in consideration. Before reaching T_c they present a region called of *current sharing*, in which their electrical resistivity is no more zero but always less than that of the surrounding alloy.

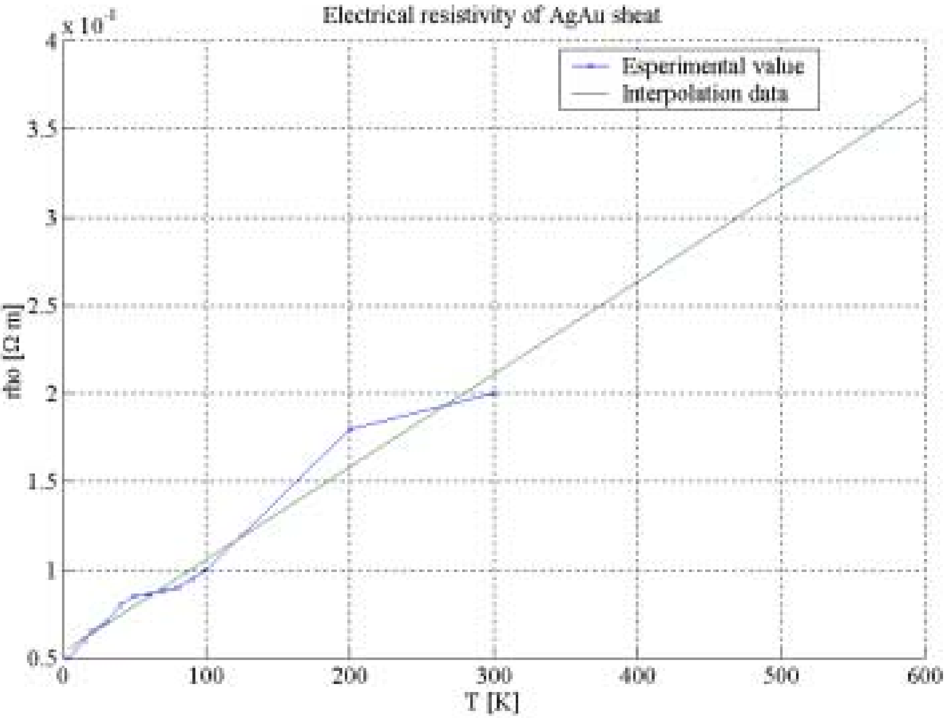

Figure 5-11. Electrical resistivity of AgAu alloy 4 % Au wt.

The resistive transition curve of a composite superconductor can well be approximated by the power law: $E \propto I^n$ [51] where E is the electric field along the superconductor and I the transport current. The index n reflects the sharpness of the resistive transition: the sharper the transition, the larger is *n*. For BSCCO 2223 a common-used value for *n* is 9.

Using this power law it is possible to describe analytically the current sharing region:

$$
\begin{aligned}
& E \propto I^n \propto \left(\frac{E}{R}\right)^n \rightarrow E^{n-1} \propto R^{-n} \\
& E \propto \rho^{\frac{n}{n-1}} \left(\frac{L}{A}\right)^{\frac{n}{n-1}} \\
& J = \frac{I}{A} \rightarrow E = RI = RJA = \rho JL \\
& \rho \propto J^{n-1} \frac{A^n}{L}
\end{aligned}
\tag{47}
$$

Using this relationship it is possible to correlate the value of the electrical resistivity at temperature *T* with the one at a given temperature. Then, the electrical resistivity in the *current sharing* region is expressed by:

$$
\rho(T) = \rho(T_0)\left(\frac{J}{J(T_0)}\right)^{n-1} \tag{48}
$$

where T_0 indicates the given temperature at which the value is taken.

Using the values taken from [52, 53, 54] for $J(T)$ and $\rho(T)$, the plot of the electrical resistivity of BSCCO 2223 is reported in the following figure (Figure 5-12).

The current sharing region starts at about 70 K. The resistive transition occurs between 96 K and 110 K; then the HTS is completely resistive and its resistivity varies linearly with temperature.

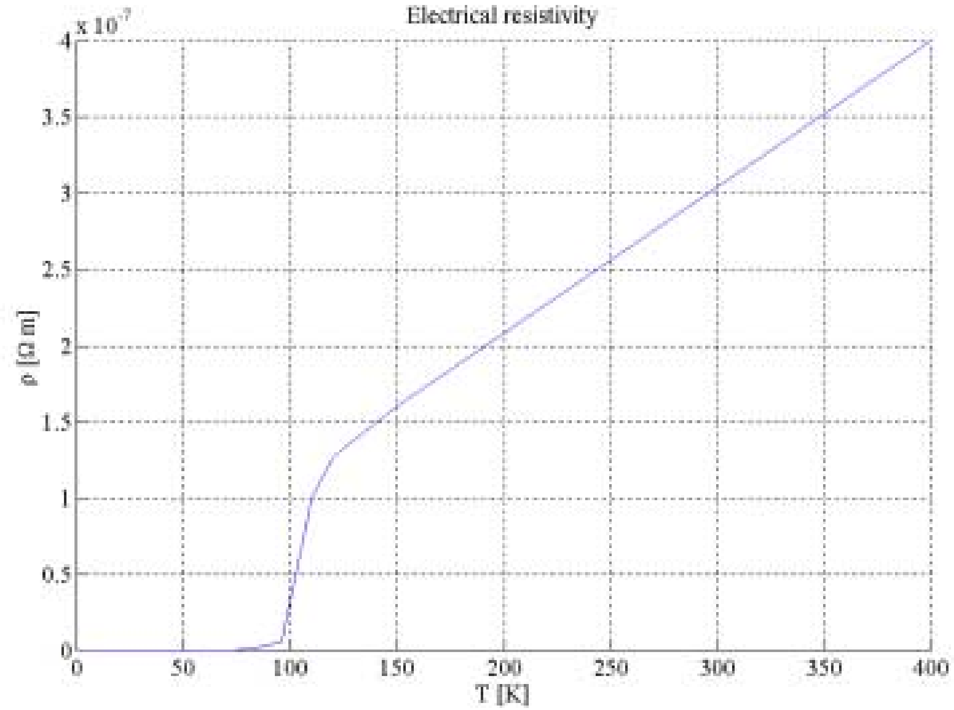

Figure 5-12. Electrical resistivity of BSCCO 2223.

Finally, using the relationship (46) and the definition of the electrical resistance: $R(T) = \rho(T)\frac{L}{A}$ the expression for $\rho_{eq}(T)$ is:

$$\rho_{eq}(T) = \frac{\rho_{AgAu}(T)\rho_{HTS}(T)}{\rho_{AgAu}(T)\cdot fu + \rho_{HTS}(T)\cdot(1 - fu)} \tag{49}$$

6 Geometric optimisation

Once written the general equations of the theoretical model I had to validate its results with experimental data. Hereinafter I will refer to the data of the prototype of the 13 kA current lead, tested here at CERN.

The material used for the 13 kA HTS assembly were the BSCCO 2223 tapes sheathed with a metallic matrix made of silver with 4 % wt of gold. The geometric dimensions of each tape are: 3.25 mm x 0.25 mm, with a length L = 0.25 m chosen for reason of design optimisation, thermal and electrical performance and space constraints. The *filling factor, fu,* of the tape is 0.27.

The first step of the development of the thermal model is the definition of the geometry of the assembly: the number of the tapes and their disposition according to the magnetic field's flux lines.

6.1 Evaluation of the number of the tapes required

The critical current I_c at 50 K with a magnetic field B = 0.13 mT (self-field) is 60 A. It means that in order to carry 13 kA I need 217 tapes that, with the dimensions written above, gives a total cross section S = 1.8 cm². For comparison, the cross section needed by a conventional conductor to carry such currents with a current density J = 4 A/mm² is about S = 32.5 cm².

The worst transient the leads have to withstand is a quench of the HTS assembly. After a "*quench detection*" the current is cut off by the protection system but the leads still have to withstand the discharge current of the magnets. The time constant for the main dipole magnets of LHC is τ = 120 s.

The goal of this optimisation is to find out the number of tapes necessary to carry this current without overheating.

As a first approximation I consider the hottest part of the tape, the upper one, and I study the temperature evolution upon time. If the lead is resistive, the equation which describes the thermal transient is:

$$(50) \qquad \frac{dT}{dt} = \frac{\rho_{el}}{\nu c_p} \frac{I^2}{A_T{}^2 (1 - fu)^2}$$

To be conservative I neglect the thermal conduction: in this way the heat generated cannot be removed. Then, because of the rather short time during the transient, I can ignore also the heat convection by the cooling gas: I consider an adiabatic transient.

The term $A_T\ (1\text{-}fu)$ represents the cross section of the metal matrix of the tape.

The expression for the decaying current is:

$$(51) \qquad I = I_0 e^{-\frac{t}{\tau}}$$

defining $\zeta = \frac{\rho_{\text{el}}}{\nu c_{\text{p}}} \frac{I^2}{(1 - fu)^2}$ and integrating the (50):

$$(52) \qquad \int_{T_0}^{T_{\max}} dT = \frac{\zeta}{A_T{}^2} \int_0^{t_B} e^{-\frac{2t}{\tau}}$$

where t_B is the time at the end of the transient and T_0 is the initial temperature of the upper part of the lead and T_{max} the maximum allowable temperature.

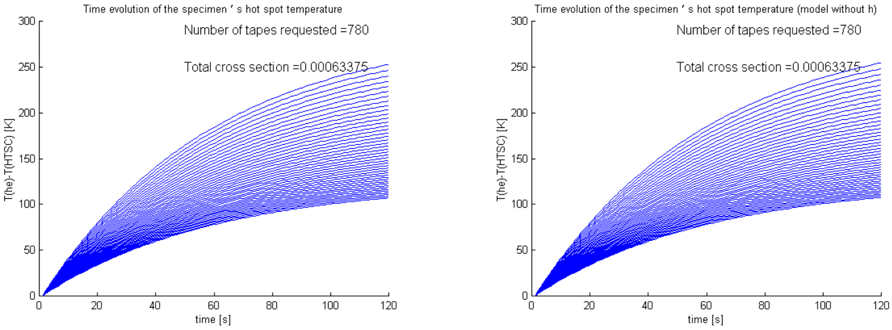

Figure 6-1. Temperature of the upper part of the tape during the resistive transient. In the right plot the evaluation using the simplified model; on the left the model which takes into account the thermal convection. The total cross sections are expressed in m².

The solution is:

$$T_{\max} - T_0 = \frac{\zeta}{A_T{}^2} \left[-\frac{\tau}{2} \left(e^{-\frac{2t_B}{\tau}} - 1 \right) \right]$$

$$A_T = \sqrt{\frac{\zeta}{T_{\max} - T_0} \left[-\frac{\tau}{2} \left(e^{-\frac{2t_B}{\tau}} - 1 \right) \right]}$$

The influence of the thermal convection in the solution is negligible as confirmed by Figure 6-1.

The total cross section needed with this hypothesis is A_t = 6.4833 cm², that is 797 tapes.

This value is considered too onerous as regards the heat conduction, i.e. a huge quantity of silver matrix leads to a large heat leak into the liquid bath: really the number of tapes is evaluated considering a safe critical current I_c = 27 A. The resultant number of tapes is N = 470, that corresponds to a cross section S = 3.81 cm²: rather ten times less than a normal conductor. With this cross section the maximum temperature reached during this adiabatic transient is T_{max} = 770 K.

Due to the too high temperature, it is necessary to introduce a protection criterion that permits to detect the quench of the tape with a safe time margin to avoid dangerous temperature increase.

6.2 Disposition of the assembly

Because of tapes' sensitivity to the magnetic field their disposition in the leads assembly has to be optimised.

The magnetic field is dangerous for the tapes because it causes a degradation of the superconducting properties of the ceramic oxide. Then, the anisotropic behaviour of the BSCCO material is such that a magnetic field along the *c-axis* of the tape is more dangerous as regards to the transport properties than one parallel to the *ab-plane*.

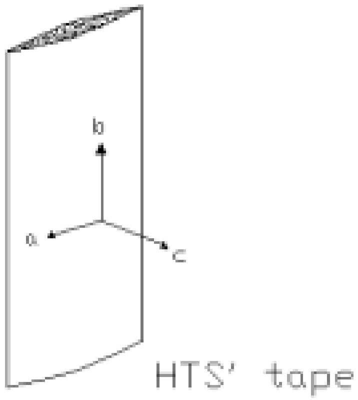

The tapes are placed onto a stainless steel cylindrical support. Its diameter is fixed to D = 100 mm.

The tapes are packed together in small groups and placed onto the external side of the cylinder. As regards to their orientation there are two possible solutions: with radial *c-axis* or tangent *c-axis*.

I used QuickField© to perform a magnetic analysis of the assembly in the two different solutions.

The tapes are packed in 76 cluster of 7 tapes each one. Their cross dimension is about 3 x 3 mm.

The average current density of each block is about 170 A.

The intensity of the magnetic field generated by the flowing current, and its flux lines, are reported in Figure 6-2.

The values of the magnetic field along a line that radially cross the assembly are reported in Figure 6-3.

As we see from the picture of the flux lines the *radial c-axis* configuration is the only one which assures a magnetic field perpendicular to the *c* direction.

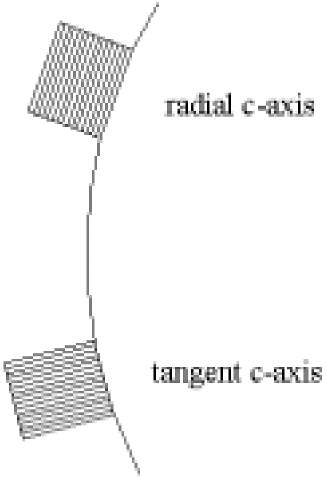

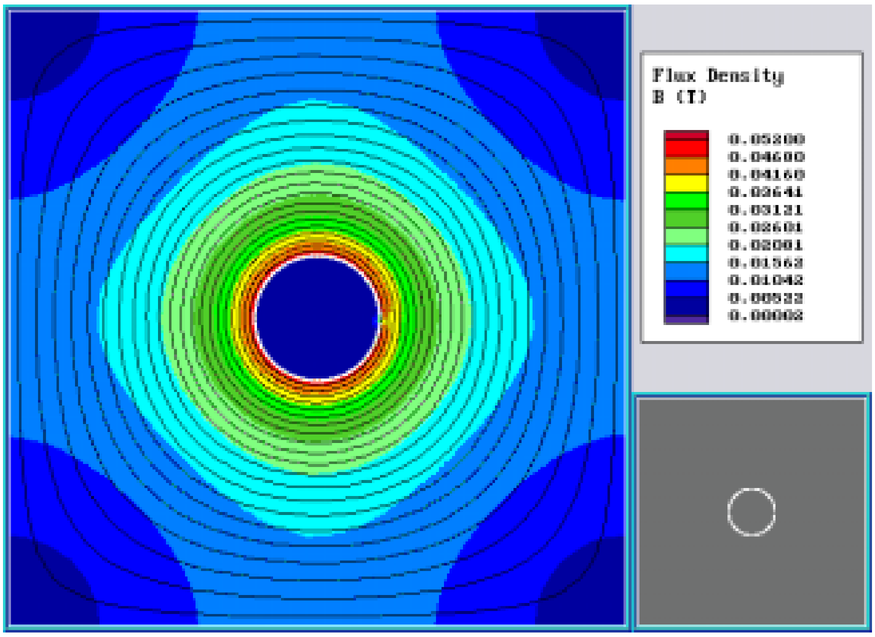

Figure 6-2. Magnetic field's lines. In the box on the lower right there is a sketch of the cylindrical assembly. The magnetic field's lines are parallel to the cylinder surface.

To increase the interleaves between the clusters of tapes and improve the cooling effect of helium, the number of tapes for each one is increased up to 10. At the end the number of cluster is 47 with 10 tapes each one. The tapes are assembled in the *radial c-axis* configuration: the magnetic field is parallel to the flowing direction and its maximum value is about B = 0.045 T.

Externally to the tape assembly, another stainless steel cylinder is used to mechanically protect the superconductors and guide the helium gas.

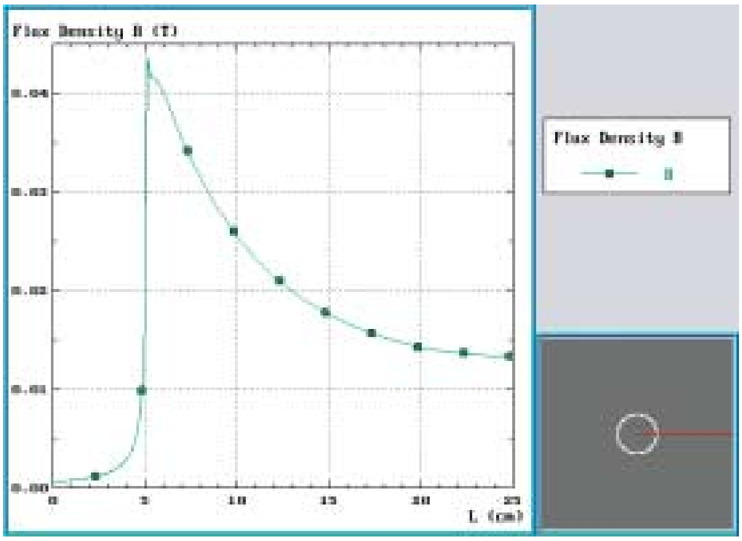

Figure 6-3. Magnetic field from the centre of the SS cylinder, in the radial direction.

The diameter of the stainless steel cylinder has to be chosen according to the cooling needs of the leads. The helium vapour rises along the channel left between the clusters. The space between the blocks and the outer cylinder determine the cooling channel. If I take a radius for the outer cylinder exactly equal to $R_{inner} + d$, where d is the depth of the tape's clusters, the cooling channel is a close rectangle whose dimensions are comparable with the ones of the clusters.

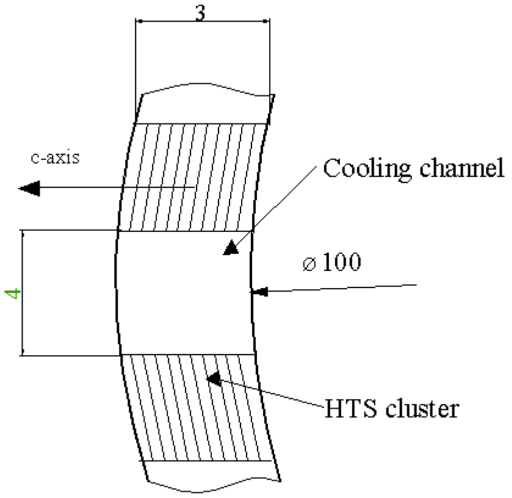

Figure 6-4. Sketch of the cooling channel in the lead's assembly.

The dimensions of the channel are 4 x 3 mm^2; the cross secrion of the clusters is 3 x 3.25 mm^2.

The wet perimeter of the tapes assemblage is about C = 10 mm. The equivalent diameter of the channel is: $D_{eq} = \frac{4S}{C}$, where S is the channel cross section.

In this geometry, a channel cros ssection S = 4 x 3 mm², leads to a D_{eq} that is approximately what I used in the Reynolds number evaluation in the previous chapter.

7 Thermal model validation

In this chapter there are the results of the thermal model I did. As previously said I validate the numerical results with the experimental data obtained from the tests of the 13 kA current leads.

In the following paragraphs there will be a brief description of the experimental apparatus used in those tests; then the test results will be compared to the numerical ones I obtained with my model.

7.1 Experimental results

The main parameters for the superconducting part of the 13 kA assemblies are the following:

Range of temperature	50 K – 4.5 K
Total length	L = 0.25 m
Matrix alloy	Ag 4% wt Au
Tape's cross section	0.25 x 3.25 mm²
Critical current per tape	I_c = 60 A (@50 K, 1.3 mT)
Numbers of tapes	n = 470
Filling factor	fu = 0.27

In the figure one of the current leads used in the tests.

7.1.1 Cryostat description

A cryostat has been built at CERN to test the thermoelectric performance of the prototype leads [55]. The cryostat provides the required working conditions: 4.5 K helium bath to cool the bottom part of the leads, warm helium gas to quench the HTS, recovery of helium gas to cool down the HTS and the necessary instrumentation and valve actuators for control and diagnostic measurements. The control and data acquisition system allows to monitor and to automatically control transients such as cool down, warm-up and current ramping.

The test cryostat is composed of an annular (outer) cryostat providing radiation shielding at 4.5 K, neck thermal interception of the inner cryostat and an inner cryostat in which the current leads are housed and cooled to maintain their nominal operating conditions.

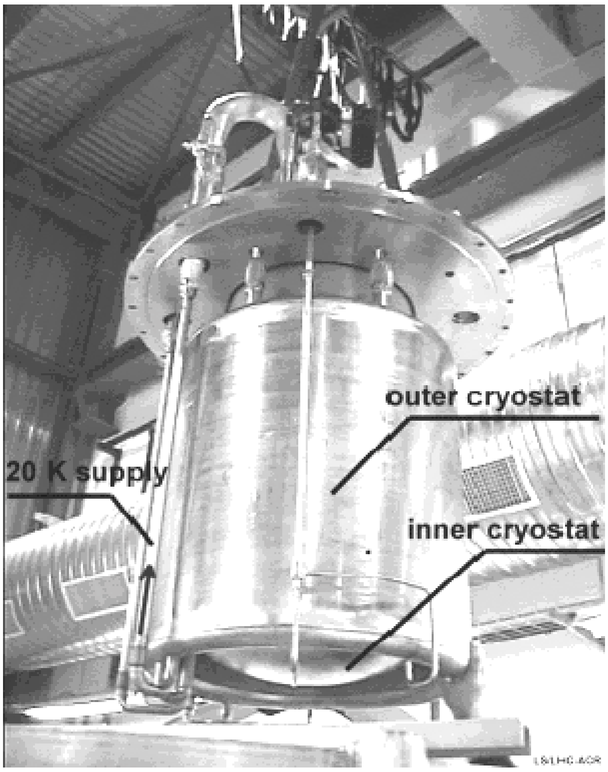

Figure 7-1. Inner and outer cryostat view.

The system makes use of the cryogenic infrastructures available at CERN, in particular a 6 kW @ 4.5 K cryogenic plant. Liquid helium is distributed via a vacuum-insulated and radiation-shielded transfer line, providing cooling and gas recovery for several test stations. The outer cryostat is filled with liquid helium and acts as a supply of liquid for the inner cryostat via cryogenic valve and for cold gaseous helium for cooling the resistive part of the leads. An electrical heater can be used to increase the boil-off from the outer cryostat during powering of the leads when a higher mass flow is required.

The test station has been designed for a maximum liquefaction requirement of about 4 g/s. The total nominal inventory of liquid helium in the two cryostats is about 150 l.

Two mass flow controllers adjust the necessary flow-rate to obtain the required gas temperature of 20 K. Additional electrical valves are used to add room temperature gas thereby increasing the temperature of the cooling flow in order to quench the HTS. The gas is recovered at the top part of each lead via an electro-pneumatic valve, which regulates the mass flow in order to maintain the HTS warm temperature at 50 K. These valves can also control the mass flow-rate depending on the current in the leads.

The pressure in the inner and outer cryostat is controlled via electro-pneumatic valves.

All the circuits' temperatures are monitored with Platinum 100 sensors (300 to 25 K) and Carbon or CERNOX™ sensors (25 to 4.5 K). The current leads of this test are equipped with a PT100 temperature sensor for the upper end of the HTS and a CERNOX™ for the lower part of the superconducting equipment. Several PT100 are distributed over the resistive part of the lead to measure its temperature profile.

Liquid levels are measured with superconducting wire gauges that can be pulsed to decreased heat input to the liquid helium bath.

Helium flow is measured at ambient temperature using thermal mass (0.5 g/s of full scale reading with 1% accuracy) and V-cone™ flowmeters (1.2 g/s of full scale reading with 1% of accuracy). In view of its accuracy over the full range, the first type is used to measure the boil-off from the leads bath; the second type is employed at the warm outlet of the current leads to measure the flow of 20 K helium gas.

Differential pressure sensors check the pressure drop in the resistive part of the lead.

The process control is performed using an industrial Programmable Logic Controller (PLC) in which the number of I/O channels is of the order of 30 and there are about 7 closed control loop. The automatic operation modes include cool down, normal operation, quench and warm-up. This equipment is interfaced with an industrial supervision system based on PCVUE32™.

The powering system of the leads is interlocked to the liquid level signal, the temperature of the warm part of the HTS and the cryogenic operator authorisation. The process control system is designed to run in fully automated mode 24h/24h. A shift operator is automatically called if a parameter of importance deviates from its expected range. The system can also be remotely accessed via Internet.

7.1.2 Temperature sensing probes

For the superconducting part of the current leads we used two temperature sensors: at the top end a platinum sensor, and a CERNOX™ probe in the second half of the lead where the temperature is lower.

Those sensors are based on the change with temperature of the resistance of the metals or semiconductors.

The PT100 is a platinum sensor [56]. It is used for temperature between 25 and 500 K. It shows a low dependence on the magnetic field and does not require individual calibration for temperature above the liquid nitrogen one. For lower temperature individual calibration leads to lower temperature errors.

Its calibration curve is:

$$T = 38.894 \cdot V + 26.247$$

The CERNOX™ [57] probe is useful at lower temperature and in the test described in this chapter have been used for the lower sensor, at about 12 K. This kind of sensors are extremely sensitive at low temperature. Instead of a metal it uses a semiconductor and so its temperature coefficient is negative, i.e. the resistivity increase when the temperature decrease.

It requires an individual calibration according to the range of temperature in which will be used. The model used in this test is CERNOX™ CX-1050-SD N° XO-05511. Its calibration curve is:

$$T = 10^{\frac{A_0}{(\log V)^0} + \frac{A_1}{(\log V)^1} + \frac{A_2}{(\log V)^2} + \frac{A_3}{(\log V)^3} + \frac{A_4}{(\log V)^4} + \frac{A_5}{(\log V)^5} + \frac{A_6}{(\log V)^6} + \frac{A_7}{(\log V)^7} + \frac{A_8}{(\log V)^8} + \frac{A_9}{(\log V)^9}}$$

where the constant are:

A0	343.3971658
A1	-8924.677189
A2	101083.1321
A3	-655663.8864
A4	2.69E+06
A5	-7.20E+06
A6	1.26E+07
A7	-1.40E+07
A8	8.96E+06
A9	-2.50E+06

and V is the output voltage signal obtained from the temperature probe.

7.1.3 Experimental data

The tests were performed to study the quench transient of the superconducting part in the 13 kA assembly. The top edge of the superconductor was warmed up to the critical temperature T_c. Once started the quench, the voltage drop across the HTS and its temperature (at the top and close to the end) were taken and recorded [58].

The leads are tested in pairs, with a low-temperature superconducting short at the cold end. The instrumentation, like temperature probes and voltage taps, is installed on the leads by the companies according to the CERN specifications.

Voltages, temperatures and current are recorded by a data acquisition system built with LabVIEW®.

Measurement have been performed in stand-by (I = 0 A) and in nominal operation (I = 13 kA). The leads are optimised for operating at 13 kA with the minimum 20 K helium flow which maintains the warm end of the superconductor at temperature T_0 below 50 K. The warm end of the resistive part is maintained at about 290 K.

For the measurements in operating condition (I =13 kA), the temperature at the warm end of the superconductor is brought to its critical value by increasing, at nominal current, the inlet temperature of the gas cooling the resistive heat exchanger. The quench detection signal is the voltage drop across the HTS element.

The heat flow in nominal operation condition is found to be $Q_{st} \approx 1$ W.

The quench test on the 13 kA current leads gave the following results.

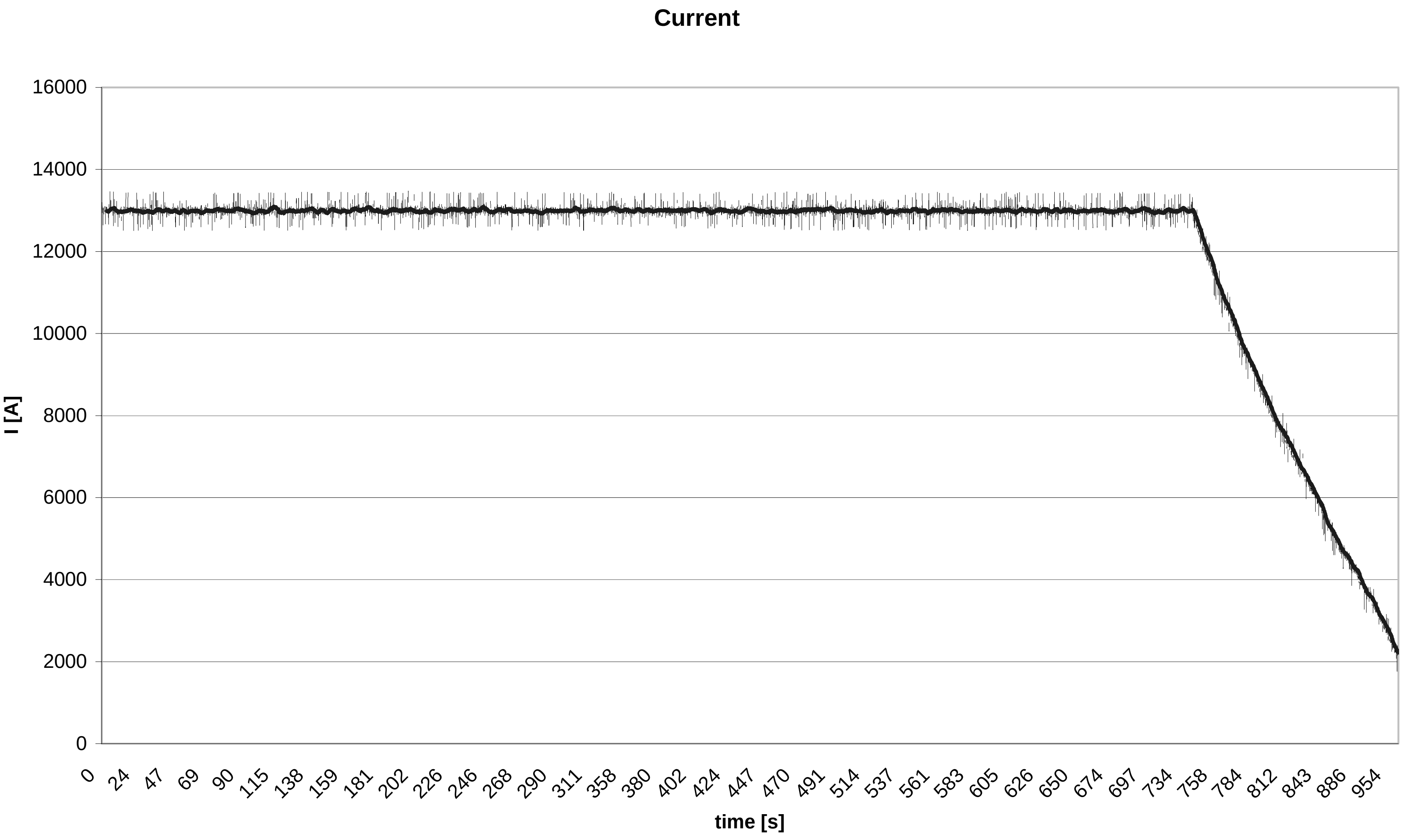
Current
16000
14000
12000
10000
8000
6000
4000
2000
0
I [A]
0
24
47
69
90
115
138
159
181
202
226
246
268
290
311
358
380
402
424
447
470
491
514
537
561
583
605
626
650
674
697
734
758
784
812
843
886
954
time [s]

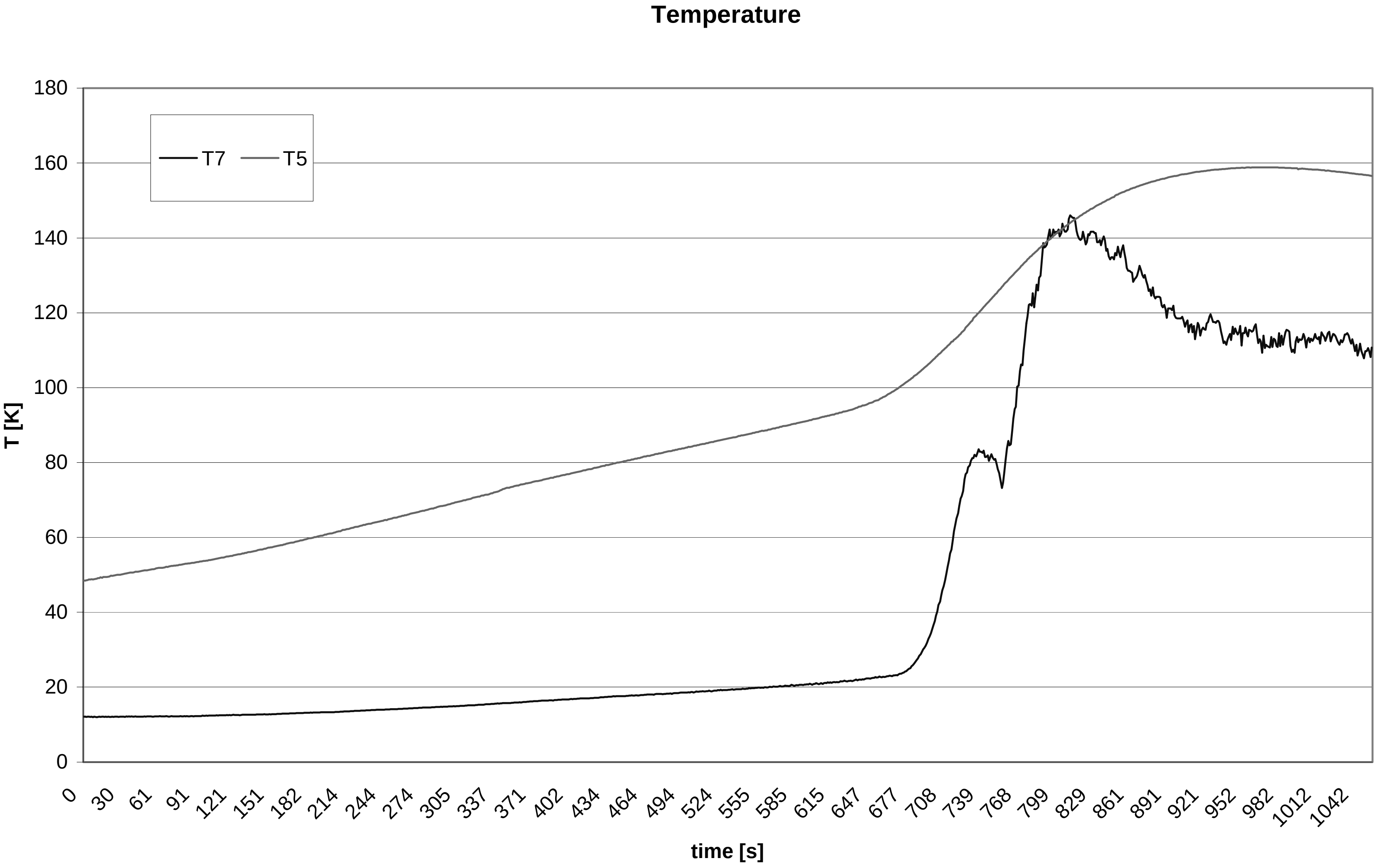
Temperature
T7
T5
T [K]
180
160
140
120
100
80
60
40
20
0
time [s]
0
30
61
91
121
151
182
214
244
274
305
337
371
402
434
464
494
524
555
585
615
647
677
708
739
768
799
829
861
891
921
952
982
1012
1042

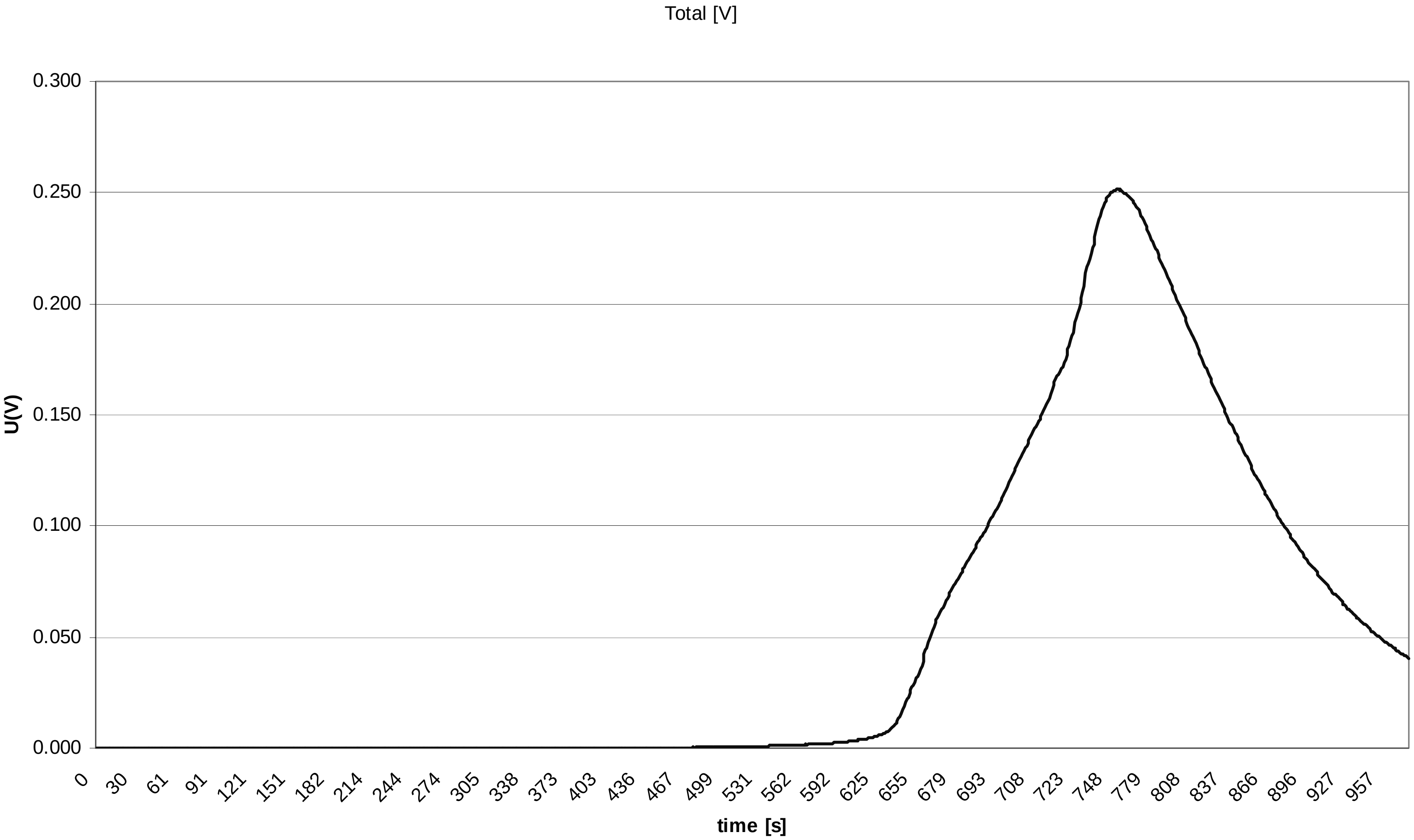
Total [V]
U(V)
0.300
0.250
0.200
0.150
0.100
0.050
0.000
0
30
61
91
121
151
182
214
244
274
305
338
373
403
436
467
499
531
562
592
625
655
679
693
708
723
748
779
808
837
866
896
927
957
time [s]

The quench detection signal was set to 0.25 V [59].

After detecting the resistive transition (when the measured voltage is equal to the V_{lim}), the current is made to decay exponentially with a time constant of 120 seconds. After 1τ the flowing current reaches value less than 2 kA, i.e. less than 15% of the nominal current.

The total heat generated during the transient is given by:

$$\begin{aligned} P(t) &= V(t)I(t) \\ W &= \int_0^{t_b} V(t)I(t)\,dt \end{aligned} \tag{53}$$

According to the experimental data $W_T = 3.9\ 10^5$ J.

The first temperature sensor *Tb7* is at the top end of the HTS; the second one, *Tb5* is placed below the middle of the superconducting lead.

The irregular shape of *Tb7*'s plot is due both to the difficulty of placement of the sensors on the assembly and to the thermal noise due to the steel support. About this aspect I will make some more considerations in the following paragraphs.

The voltage taps are placed at the top end, in the middle and at the low end of the HTS. The signal reported in the previous plot is the sum of these two signals.

7.2 Theoretical results

I run the code using the numerical data of the 13 kA prototype to check the validity of the thermal model. At first I got the results for the steady case: the temperature profile and the heat load.

With the steady temperature profile I run the transient simulation and I reproduced the experimental quench transient. In this section there are the numerical results of the prototype simulation.

7.2.1 *Steady solutions*

I computed the temperature profile of the HTS assembly in the pure conduction approximation: I used the thermal equations reported in Chapter 4, assuming the thermal conduction as the only form of heat transport in the assembly. This is a first approximation in which I neglect the cooling due to the evaporating helium. In this configuration the heat load is the highest for such assembly.

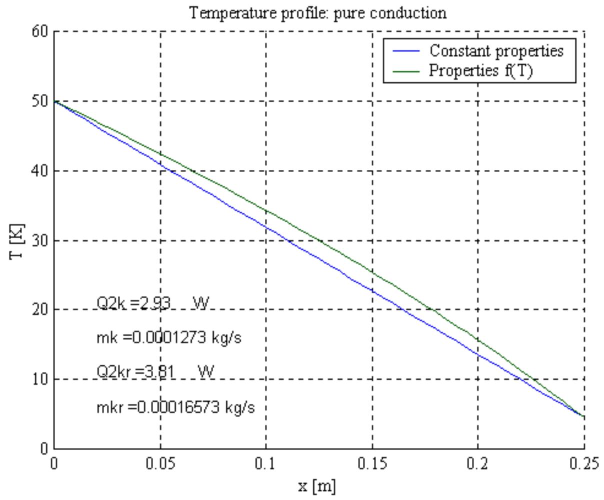

Figure 7-2. Pure conduction heat transfer.

With *Q2k* I indicate the heat leak into the liquid helium bath when all the properties of the material are constant. *Q2kr* is the heat leak when all the properties are function of *T*, as it was said in Chapter 4; *mk* and *mkr* are the respective mass flow in *kg/s*.

Hypothesizing an ideal heat transfer between the tape and the flowing helium, i.e. the *h* coefficient ideally close to ∞, I obtained the best configuration of heat exchange and consequently the heat load is the smallest possible for the assembly.

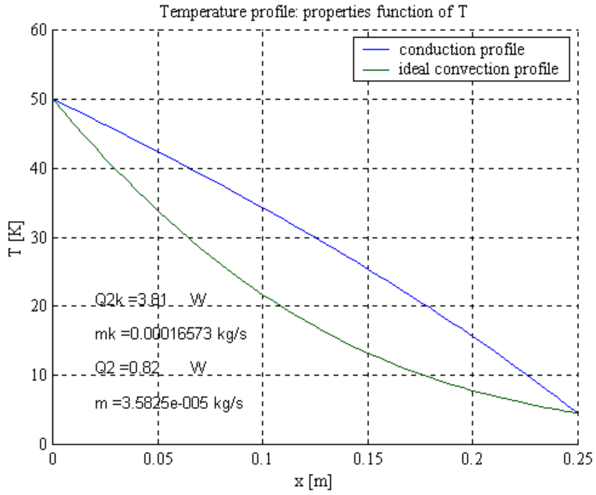

Figure 7-3. Comparison between the ideal convection and the pure conduction heat exchange.

Q2k and *mk* are respectively the heat leak and the mass flow for the pure conduction heat transfer; *Q2* and *m* are those of the ideal convection mechanism of heat exchange.

The real solution must be between those two: the real heat inleak into the helium bath will fall between those two values.

The final temperature profile for the tapes of the current leads in the normal working condition is reported in Figure 7-4.

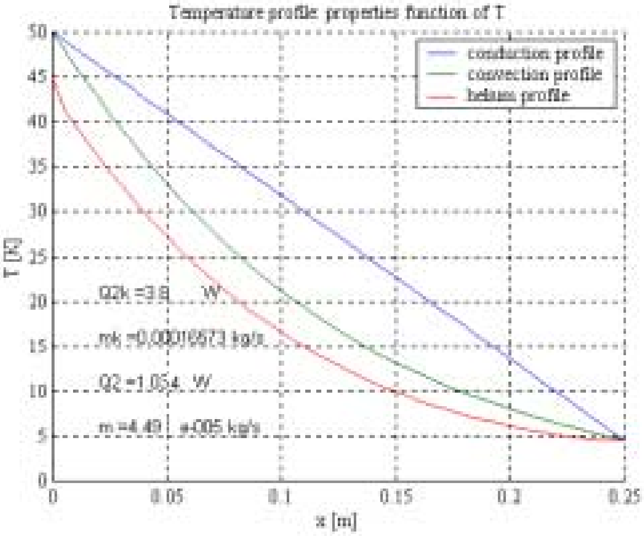

Figure 7-4. Steady temperature profile for the 13 kA current leads.

In Figure 7-4 *Q2* and m are the value for the real heat leak and mass flow.

In Table 7-1 are summarised the results, for the steady solution of the 13 kA HTS assembly:

Table 7-1.

	Pure conduction	**Real case**	**Ideal convection**
Heat inleak Q [W]	3.8 W	1.034 W	0.82 W
Helium mass flow ratio m [kg/s]	$1.6\ 10^{-4}$ kg/s	$4.5\ 10^{-5}$ kg/s	$3.5\ 10^{-5}$ kg/s

From these results it comes out the importance of the vapour cooling for the leads: in the stationary working condition it allows a reduction of the heat load in the liquid bath by a factor of 4.6 . It emerges also that the geometric configuration of that assemblage shows a good coefficient of thermal convection between helium and the tapes.

A final consideration is the crushing superiority of performances of the superconducting devices compared with the traditional ones: in Chapter 4 was computed the theoretical minimum heat flux for a all-metal optimised current lead: Q'_{all-m} = 1.04 W/kA, that for the 13 kA it means Q_{all-m} = 13.5 W. It is more than 10 times the superconducting one.

According to what previously reported the experimental measurements gave a steady-state heat flux into the liquid bath $Q_{ex} \approx 1$ W: then the theoretical model is in great accordance with the test data.

7.2.2 *Transient analysis*

I run the code with the unsteady equations to simulate the quench measured during the tests. To this purpose I heated the warm end of the tapes as described previously. The warming rate for T_0 is set equal to the experimental data:

$$\frac{dT_0}{dt} = 0.07 \quad \left[\frac{\mathrm{K}}{\mathrm{s}}\right]$$

The temperature of *current sharing* is T_{cs} = 70 K: at this temperature the BSCCO oxide is still in the superconducting region, but its electrical resistivity starts to increase.

The transition region is between 96 and 110 K. I modelled the resistive transition considering a smooth slope for the V-I curve as typical of HTS. To do that I suppose a linear dependence from the temperature of the electrical resistivity of the superconductor.

The *MPZ*, according to its expression reported in Chapter 4, is:

$$x_m = MPZ = \frac{2QAfu}{\rho_{el} I^2}$$

Q is the pure conduction heat flow: $Q = 3.8$ W;

A is the total cross section: $A = 3.8\ 10^{-4}$ m²;

fu is the filling factor: $fu = 0.27$;

I is the nominal current: $I = 13$ kA;

ρ_{el} is the electrical resistivity of the tape at $T = T_c$: $\rho_{el} = 4\ 10^{-9}\ \Omega$ m;

Finally the *MPZ* ≅ 1 mm. In my model I use a warming region whose width is 5 mm: well above the theoretical *MPZ*.

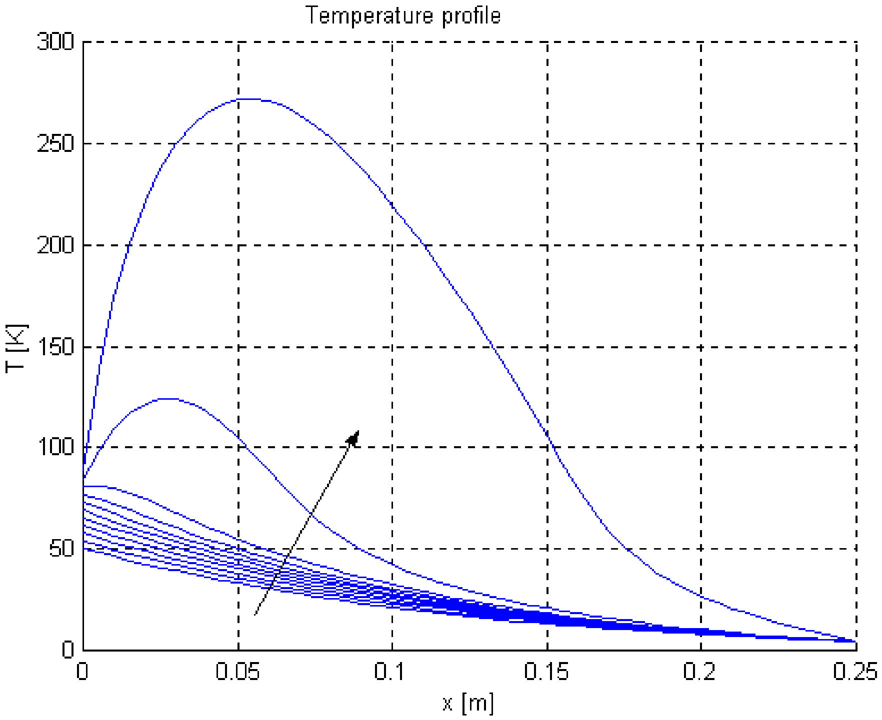

The protection criteria is the instantaneous voltage signal: the limit is the same than the experimental one: $V_{lim} = 0.25$ V.

In the following figure it is represented the quench transient.

Figure 7-5. Evaluated quench evolution: time step 5 seconds.

Once started, the quench evolves rapidly and the lead soon reaches high temperatures. The peak of T moves towards the middle of the HTS assembly.

Standing from these considerations it is clear that the tests performed in the leads were not able to identify the maximum temperature, but only the quench propagation.

We notice also that the HTS' quench is slower that the LTS' one. For the Low-Temperature superconductors in the bus-bars the propagation speed is of the order of some m/s while in this case we are dealing with few cm/s.

This allows to design an efficient quench-detection system by choosing an appropriate value for the voltage drop limit.

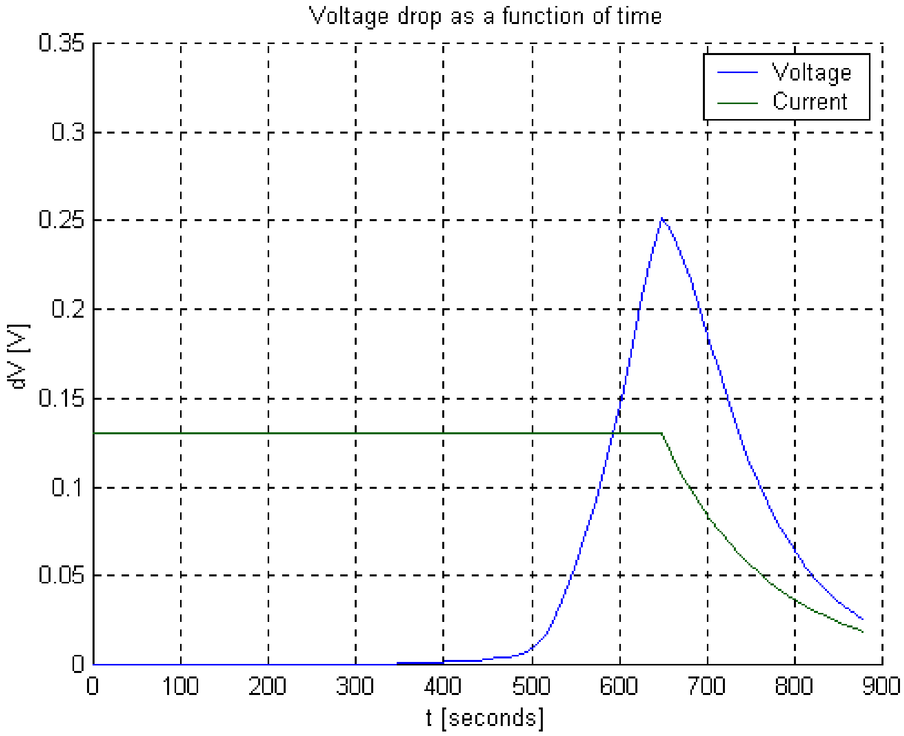

Looking at the plot of the numerical results, we can see a good agreement between the experimental and the theoretical data.

Figure 7-6. Current decay and voltage evolution. The current is expressed in arbitrary unit.

The total generated heat, during the transient is W_t = 4.2 10^5 J. The mass of helium that evaporates is, then, m_{ev} = 18 kg.

The maximum temperature reached during the transient is about T_{max} = 528 K. It falls between the two sensing probes and so is not possible to measure it experimentally. It's a quite high value and we prefer not to reach it even in a hard transient. In the following chapter I will show how is possible to reduce this value modifying the voltage limit.

Finally the theoretical model has been validate by the experiments we did. Now

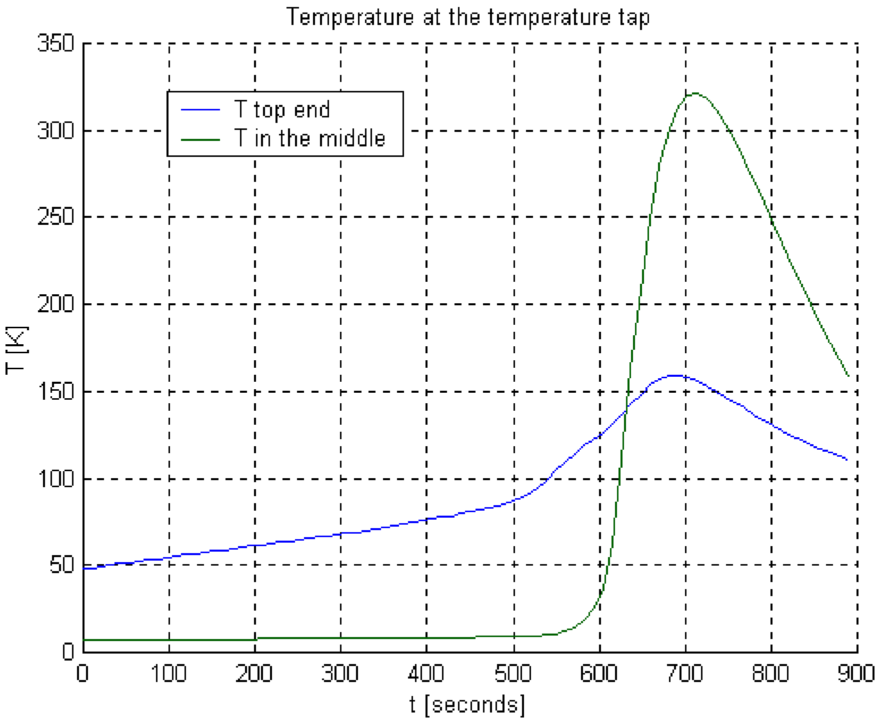

I can use that model to simulate the behaviour of the leads according to some changes brought in the design parameters.

Figure 7-7. Time evolution of temperature.

As we see the *Tb7* temperature (here "*T in the middle*") is slightly different from the experimental one. The main reason is the difficulty of measuring a temperature on the assembly due to fast variations of its value. Then, as I said before, the steel cylinder plays a role during the thermal transient and the difficulty of modelling its influence conducts to some discrepancies between the theoretical and the experimental results.

7.2.2.1 Correction factor

In the numerical code I introduced an empirical correction factor for the *thermal diffusivity* of the material: $\alpha = k(T) / (\rho c_p)_{HTS}$.

It works on the material properties and so it does not affect the theoretical structure of the code. I used it to well fit the numerical model to the real physical problem.

As regard the thermal diffusivity the presence of a stainless steel support, on which the superconducting tapes are embedded, entails a different time constant for the tapes' response. Albeit it is difficult to model this tiny influence theoretically some considerations can be made.

The general equation for an ideal convection thermal exchange is:

$$\frac{\partial T}{\partial t} = \left(\frac{k(T)}{A\rho c_p} \right)_{HTS} A \frac{\partial^2 T}{\partial x^2} + \frac{\dot{m} c_{p_{He}}}{\left(A\rho c_p \right)_{HTS}} \frac{\partial T}{\partial x}$$

The term $\alpha = \left(\frac{k(T)}{A\rho c_p} \right)_{HTS}$ has the dimensions of *1/s*: it is the time constant of the thermal conduction. In the model I used α_{HTS}: all the properties were referred to the tapes' one. In the real assembly the tapes are installed on a stainless steel support, as it was explained previously. Because of the close contact between the tapes and the steel a slight contribution in conduction by the steel could not be neglected. The α values for the tapes and the stainless steel are quite different:

$$\begin{array}{ll}
\nu_{sst} = 8.027\ 10^3\ [\text{kg/m}^3] & \nu_{HTS} = 10.34\ 10^3\ [\text{kg/m}^3] \\
< k >_{sst} = 15.57\ \ [\text{W/m/K}] & < k >_{HTS} = 43\ \ [\text{W/m/K}] \\
c_{p_{sst}} = 502\ [\text{J/kg/K}] & c_{p_{HTS}} = 200\ [\text{J/kg/K}] \\
\alpha_{sst} = 0.0037\ 10^{-3}\ [1/s] & \alpha_{HTS} = 0.021\ 10^{-3}\ [1/s]
\end{array}$$

There is one order difference between the two values. The correction factor I used takes into account this phenomenon and was determined empirically on the bases of experimental tests.

7.2.2.2 Thermal convection coefficient

As reported previously the gas cooling is determinant to reduce the heat flow into helium.

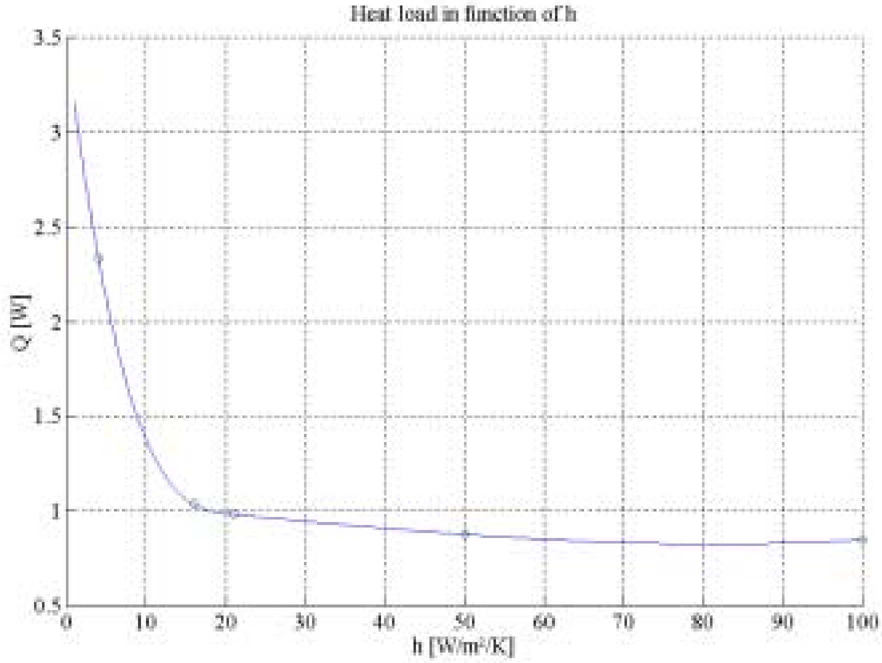

Figure 7-8. Heat leak at 4.5 K as function of the coefficient of thermal convection *h*.

In Chapter 6, I explained the empirical correlation I used for the evaluation of *h(T)*. As I said, the heat exchange coefficient is a function of the cooling gas, but also of the cooling channel geometry.

In the prototype current lead, the geometry of the channel is known, but it is not possible to know if any defect is present. Furthermore we need to know what is the real weight of the cooling parameters: the final current lead could be different than the prototype one.

In order to study this dependence, I forced into the code different values of *h(T)*. Then I plotted the dependence of the heat flux at 4.5 K as function of *h* mean (Figure 7-8).

The mean value of the convection coefficient I used in the thermal model is about h = 16 $W/m^2/K$. Then, for small deviation from this value the influence on the heat leak is slight.

7.2.2.3 Contact resistance

Another parameter one need to take into account is the contact resistance due to soldering. In particular, at the lower end of the leads, the soldering between the tape and the low-temperature superconducting wires for the connection with the bus-bars can lead to overheating due to a high value for the contact resistance.

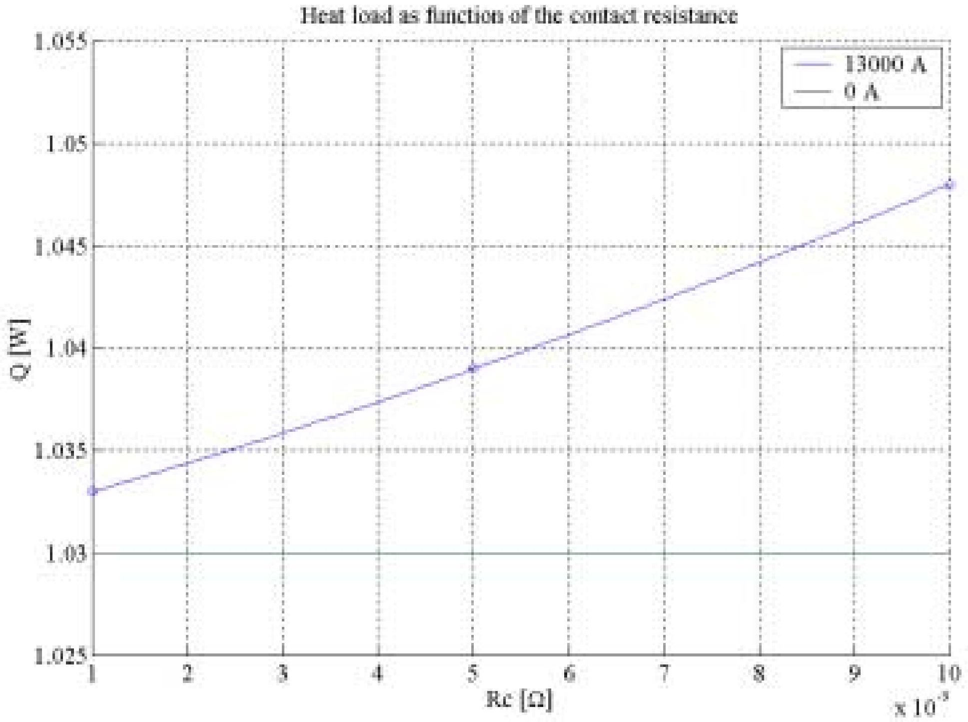

Figure 7-9. Heat flow at 4.5 K as function of the lower contact resistance. The *0 A* value is the heat flow due to the thermal gradient: i.e. with no current flowing.

The measured value for the prototype is R_c = 2.9 10^{-9} Ω. In the series production this value could be slightly higher. In the next figure I reported the value of the heat load at 4.5 K (into the liquid helium bath) as function of different values of the contact resistance.

If we pay attention to the scale of the plot we notice it is a small range of values. An acceptable contact resistance for this kind of soldering is of the order of few nΩ. In this range of values for the contact resistance the influence on the heat flow is not binding. This means that from a thermal point of view one can accept rather higher resistance. Anyhow contact resistances are a critical point: due to thermal cycling they can degrade compromising the performance of the assembly.

8 *Numerical simulation*

Once the model is validated by the experimental results, it can be applied to a different geometry and different materials, as well for different configuration parameters of the leads.

At first it is worth to focus the attention on the importance of a “real” model: that is with all the physical parameter taken into the right consideration.

Several works have been made on the subject of current leads [60, 61, 62]. In these works a similar thermal model was developed for gas cooled current leads. The main difference is the ideal convection simplification: in these works the heat exchange process that is considered is the ideal convection between the tapes and the cooling gas, whatever it is. The result of this approximation is generally underestimated.

Using my model, then, I computed a quench detection threshold for the voltage drop that allows to detect quench in time to avoid unwanted heating of the leads.

The last task was to study the difference influences of the tape’s parameter, filling factor *fu*, critical current densities etc., on the dynamic of the resistive transient evolution.

8.1 Voltage threshold

In the experimental tests the voltage limit was increased up to a value V_{lim} = 0.25 V. Whit this value the maximum temperature reached for the superconductor is T_{max} = 528 K that is considered too high. Unfortunately the voltage threshold has an inferior limit due to the background electrical noise and to the difficulties for the LHC’s electronics to detect such a small signal oven hundreds and hundreds of signals coming from the protection systems.

With an instant value for V_{lim} the safe detection signal is 5 mV. With this limit the quench does not propagate and the maximum temperature reached is T_{max} = 87 K: still in the current sharing mode. With a voltage limit V_{lim} = 1 mV the maximum temperature is lower T_{max} = 78 K, but such a small threshold could leads to spurious signals due to the background electric noise.

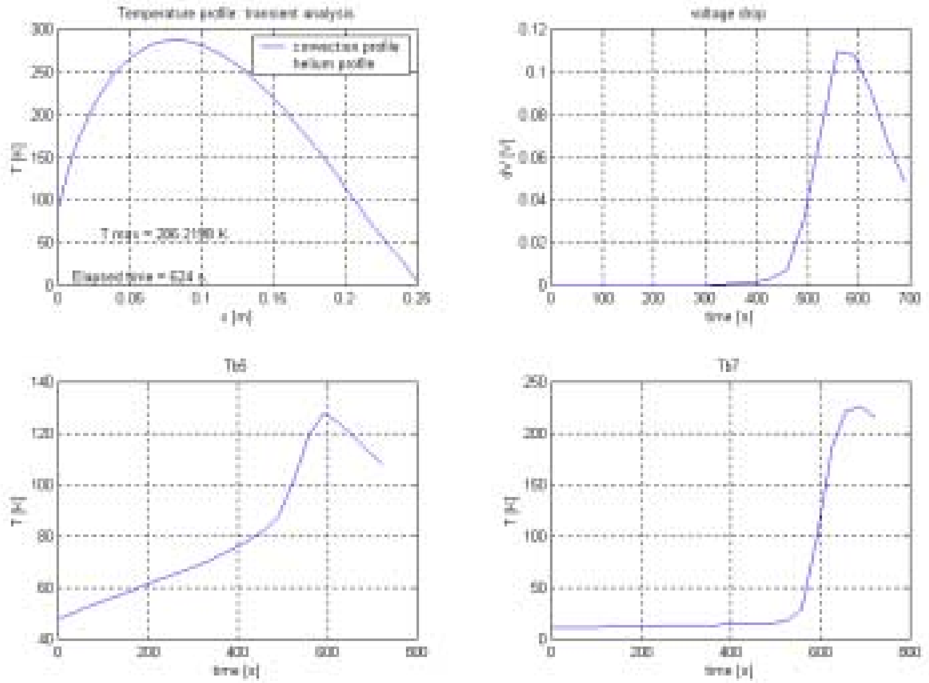

Figure 8-1. Temperature parameters for a voltage limit V_{lim} = 0.1 V. The plot in the upper left box represents the maximum temperature profile at the current cut-off.

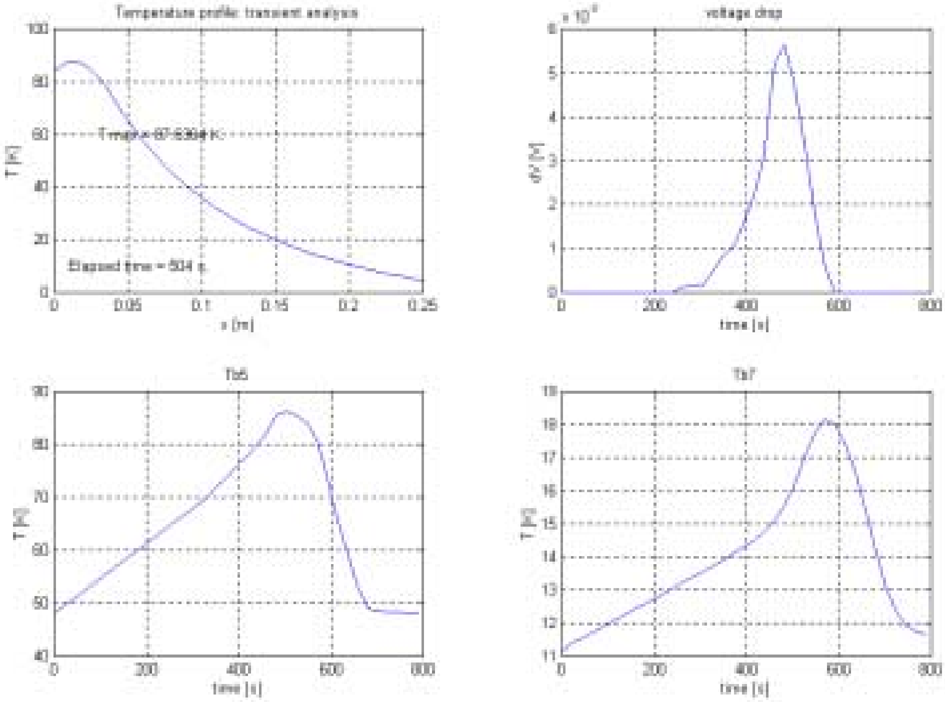

Figure 8-2. Temperature parameters for a voltage limit V_{lim} = 0.005 V.

In Figure 8-3 I reported the maximum reached temperature as function of the voltage threshold.

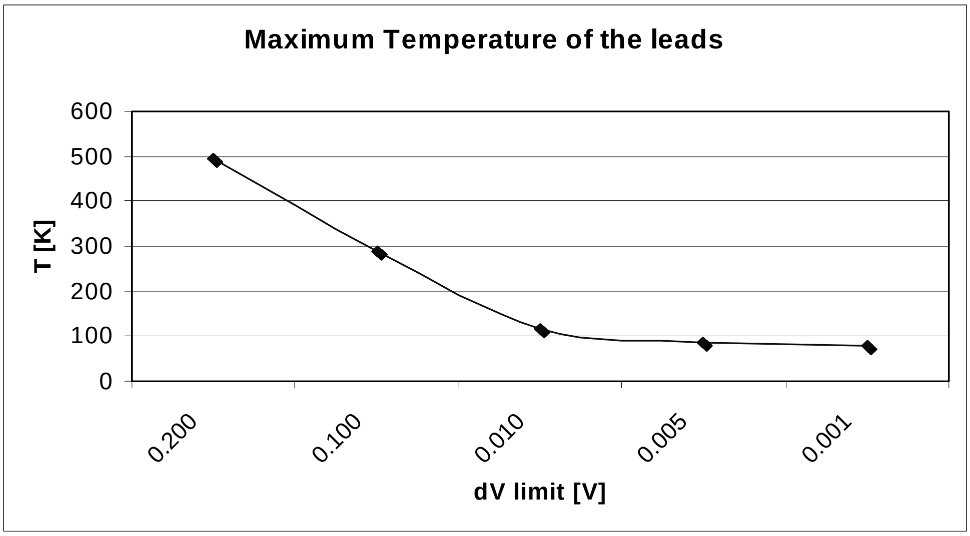

Figure 8-3. Maximum temperature of the leads as function of instant voltage limit values.

With an integrated signal I can set the limit at V_{lim} = 20 mV, integrated over 5 seconds, and quench does not propagate leading to a maximum temperature of T_{max} = 80 K.

This kind of signal is easier to detect and the risk of spurious signals is low. We can choose over a wide range of integrated limit, as it is reported in Figure 8-4.

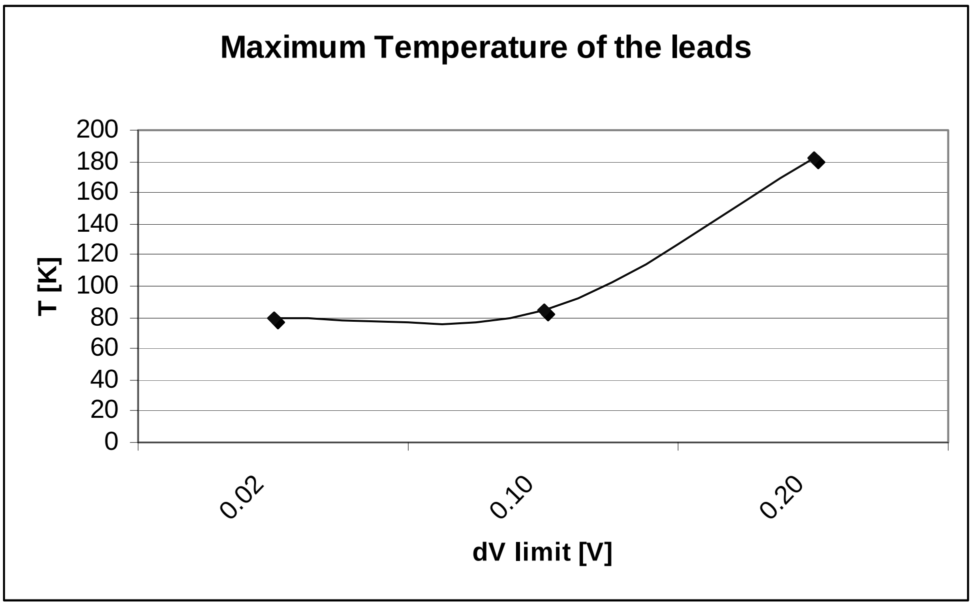

Figure 8-4. Maximum temperature of the leads as function of the integrated voltage limit. The integration time is set to 5 s.

The use of an integrated signal allows to safely detect quench and at the same time it is possible to handle from the protection signal point of view.

The temporal evolution of temperatures are reported in Figure 8-1.

It is clear that the transient in this case is lighter than in the case of the instant signal.

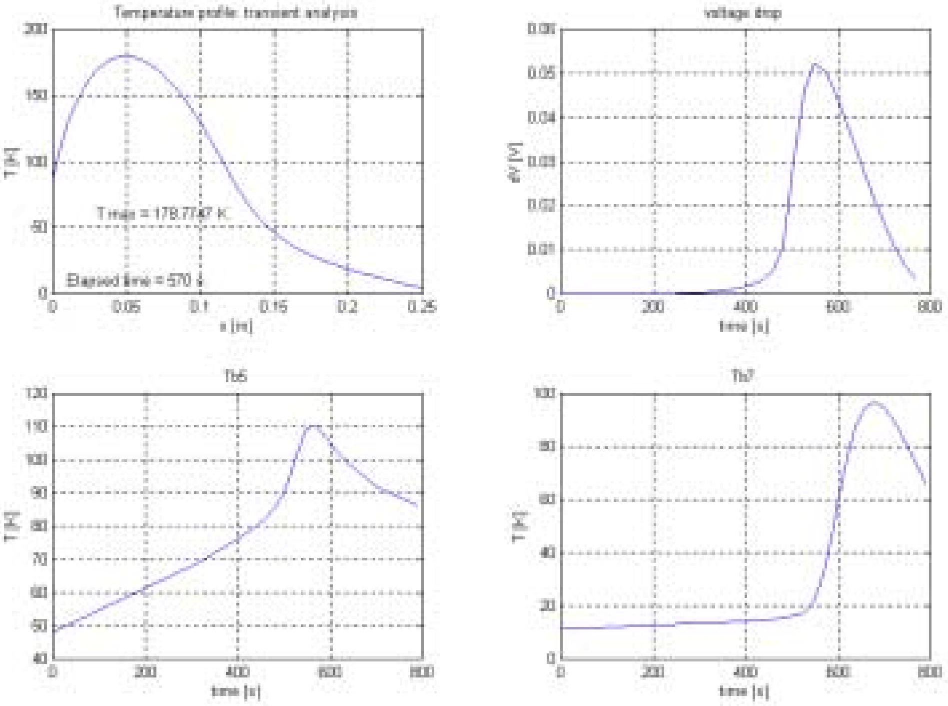

Figure 8-5. Temperature parameters for an integrated voltage signal ΔV_{lim} = 0.2 V. The integration time is set to 5 s.

8.2 Importance of gas cooling

As it was said in the previous chapter for the steady case, the gas cooling in the lead assembly permits to sensitively reduce the heat leak into the helium bath. The gain in power saving, then, is not the only advantage we have in using the gas-cooling scheme. Also the quench transient is affected by the presence of a convective cooling.

Using the rough model of Chapter 6 for the evaluation of the number of tapes I assessed the approximated maximum temperature reached in an adiabatic scheme. In that model I supposed an adiabatic transient to evaluate the number of tapes necessary to sustain the magnets discharge current without increasing the tape's temperature over a fixed value, set equal to 300 K. If I plug into the model the number of tape I am using, in the same adiabatic hypotheses, I can find the theoretical maximum temperature reached by the tapes in its warm end equal to T_{max} = 770 K. This is, obviously, the worst situation without any kind of thermal exchange.

Instead, with the unsteady thermal model, in the pure conduction approximation the maximum temperature reached is T_{max} = 620 K. Together with a higher maximum temperature, the absence of convection makes the quench to propagate widely: the overall mean temperature of the lead is higher.

To make a comparison with the experimental profile, in Figure 8-6 I used an instant voltage limit signal for quench detection V_{lim} = 0.25 V. One can compare this figure with the one on the previous chapter to notice all the differences.

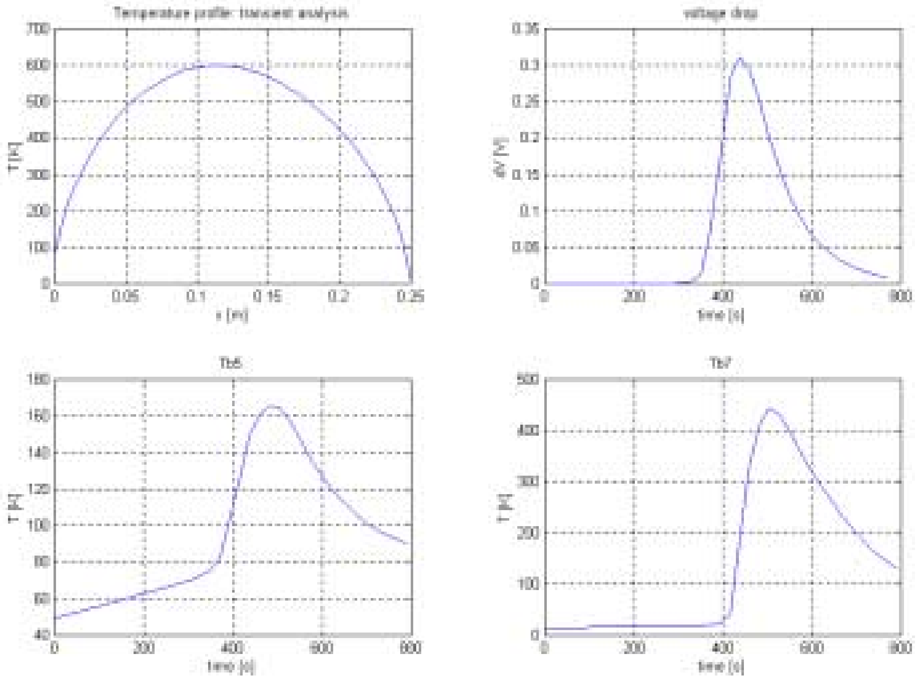

Figure 8-6. Quench transient in absence of cooling gas. The voltage limit is V_{lim} = 0.25 V. the maximum reached voltage is higher due to the more thermal inertia.

8.3 Influence of the current density of the tapes

Another important factor to determine stability in a quench transient is the critical current density of the tapes. In the tests we used a critical current I_c = 60 A (@ 50 K, 1.3 mT self-field).

A good point would be to know what would happen increasing this value. The superconductor's technology has rapidly grown and now, on a single tape, critical current of about $I_c = 120$ A (@ 50 K, 1.3 mT self-field) have been reached.

Assuming to use, for the tapes in the model, this value of critical current, I studied the quench propagation. Higher I_c means that, in order to carry the same amount of current, I can use only 235 tapes, instead of 470. While working in the normal conditions the assembly will show a lower heat flux into the helium bath with consequent less evaporating helium.

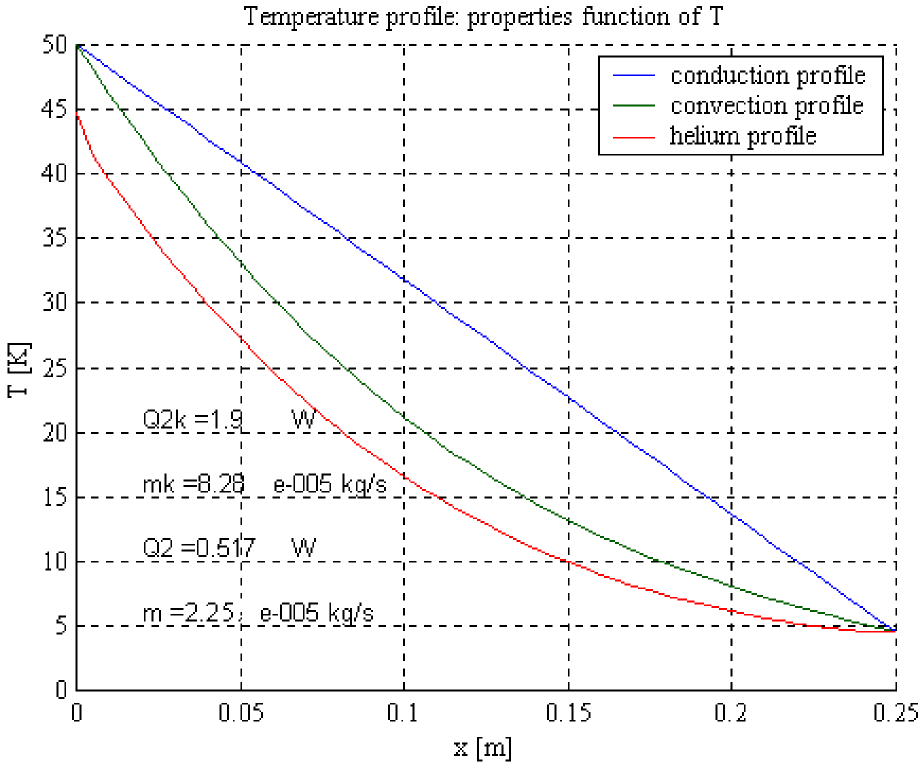

Figure 8-7. Steady solution for high critical current tapes. The number of tapes used is 235.

The total heat leak conducted in the helium bath is $Q2 = 0.52$ W: half the value of the 60A tapes.

Problems arise in a quench transient. The amount of metal now available in the tape's matrix is no more enough to dissipate the heat generated by the resistive transition.

The use of this over performing technology will then require a protection shunt for each current leads. This is a metal conductor device, assembled in parallel to the leads, dimensioned in order to be able to carry a big portion of the discharge current of the magnets in case of quench: the remaining current that flows in the superconducting tapes is then low enough not to overload the thermal capacity of the metal matrix.

Using an integral detection signal of V_{lim} = 20 mV, 10 times less than in Figure 8-5, we get a maximum value for temperature in this configuration T_{max} = 630 K.

Before choosing this kind of solution an economic analysis has to be made to the purpose to estimate the money saving due to the less number of tape involved in the assembly and to compare it with the increasing costs due to the shunts.

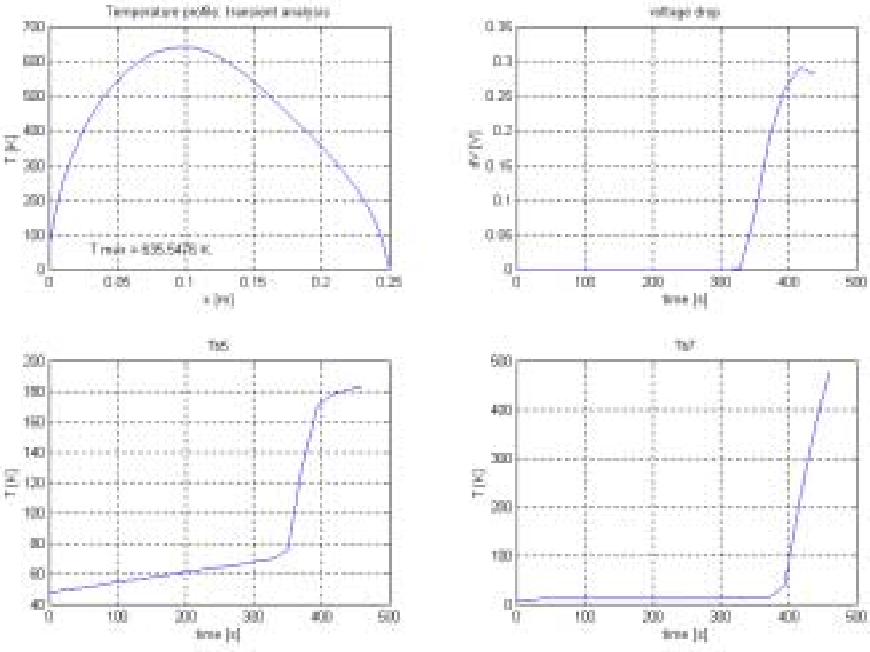

Figure 8-8. Temperature parameters for a high-I_c assembly (I_c = 120 A @ 50 K, 1.3 mT). The detection signal is integrated over 5 s and it is set to V_{lim} = 0.02 V.

8.4 Influence of the metal matrix

In the tests we used BICC's tapes for which the filling factor *fu* = 0.27. The filling factor is defined as:

$$fu = \frac{A_{HTS}}{A_{tot}}$$

It represents the percentile amount of superconductor on the tape's cross section: *fu* = 0.27 is a common used value for BICC, however different values are available.

By changing the *fu* value, keeping the same total cross section, actually I change the total amount of the metal matrix in the assembly. The total cross section for the lead assembly was overestimated for safety reason, as it was reported in Chapter 6. Varying *fu* I reduce this safety margin: it is like using tapes with higher critical current.

Increasing the value of the filling factor will lead to a lower heat flux, in the steady case; but it will cause thermal instability during quench. The reduction of the metal matrix will reduce the tape's shunt in case of resistive transition: the flowing current does not have enough cross-section and will overheat the tape.

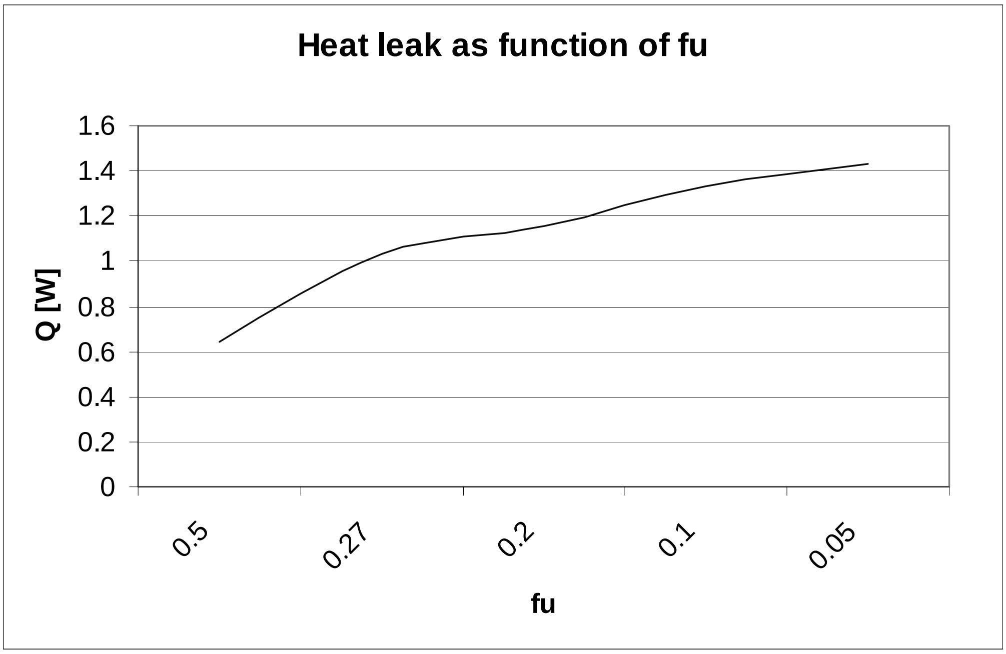

Figure 8-9. Heat leak at 4.5 K as function of the filling factor *fu*.

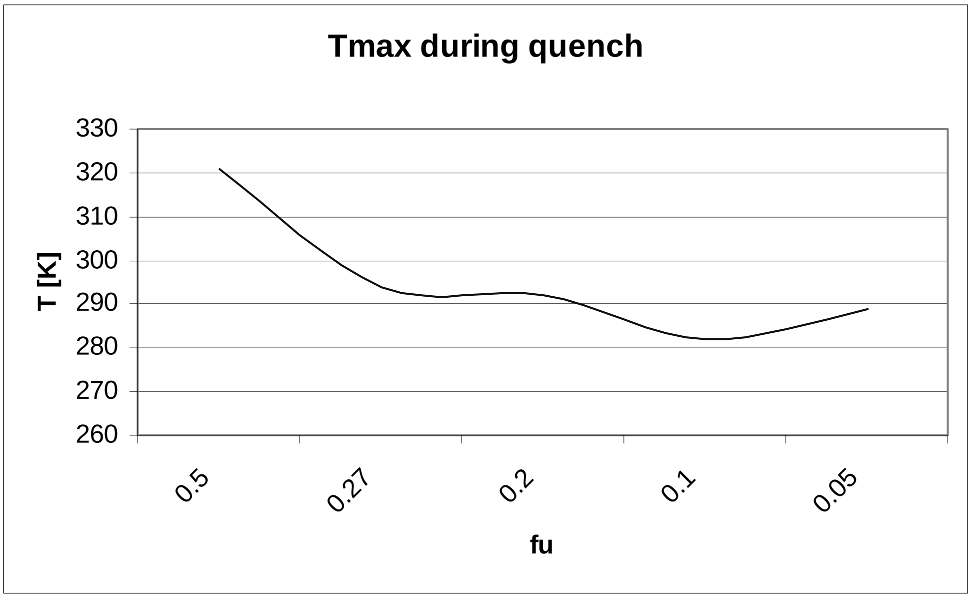

Figure 8-10. Maximum temperature of the lead, during the resistive transition as function of the filling factor *fu*. T_{max} was evaluated according to the instant voltage limit, and V_{lim} = 0.1 V.

In Figure 8-9 the shape of the curve is the one predicted; as regards the maximum temperature there is a slight increase if T_{max} passing from *fu* = 0.1 to *fu* =

0.05. The reason is that on this situation the reduction of the superconducting cross section affects the current-sharing region: with a relative low detection signal (V_{lim} = 0.1 V) the quench does not evolve dramatically: the temperature increase is limited and the influence of the current sharing region endures.

On the other hand one can compare the behaviour of the HTS for the same voltage limit, V_{lim} = 0.1 V, and *fu* = 0.27 or *fu* = 0.5.

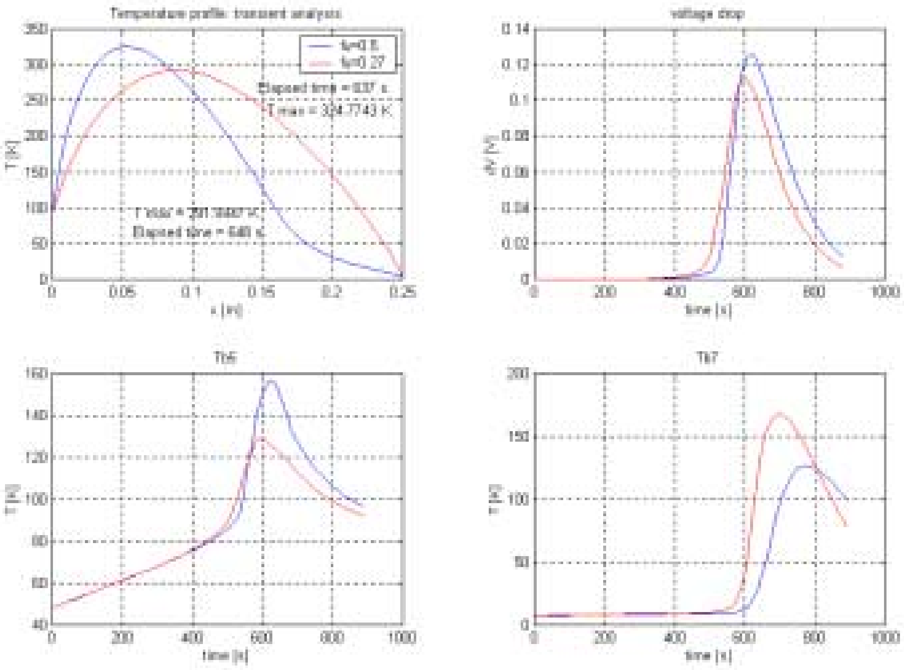

Figure 8-11. Temperature parameters of quench transient for two different values of the filling factor *fu*. The instant voltage limit is V_{lim} = 0.1 V.

For higher *fu*, that is for less amount of metal in the cross section, the maximum temperature is higher as it was noticed, but the propagation speed of the resistive transition is lower because of the low thermal conductivity. For this reason the detection voltage is reached sooner and the resistive transition does not propagate widely, as it is evident from the *Tb7*’s plot. Using low detection thresholds, a higher filling factor contributes to restrain the quench propagation involving a slight increase of the maximum temperature: from 291 K to 324 K.

8.5 Influence of alloying

For the metal matrix the alloying with gold was required for a thermal reason, because it decreases the thermal conductivity of pure silver, and for a chemical reason: it does not react chemically with the superconducting oxide as copper-alloys do.

It is necessary, now, to find a criterion in order to choose among the various Ag-Au alloys the best one for this purpose.

The silver-gold alloys present a lower thermal conductivity than pure silver but a higher electrical resistivity. If on one hand I decrease the heat load into helium in the nominal working conditions, from the other hand, during a resistive transition, I increase the energy loss due to Joule effect.

By changing in the code the thermal and electrical properties of the materials, I studied quench using different alloys for the metal matrix.

As function of gold enrichment, the stationary heat load at 4.5 K is reported in the picture.

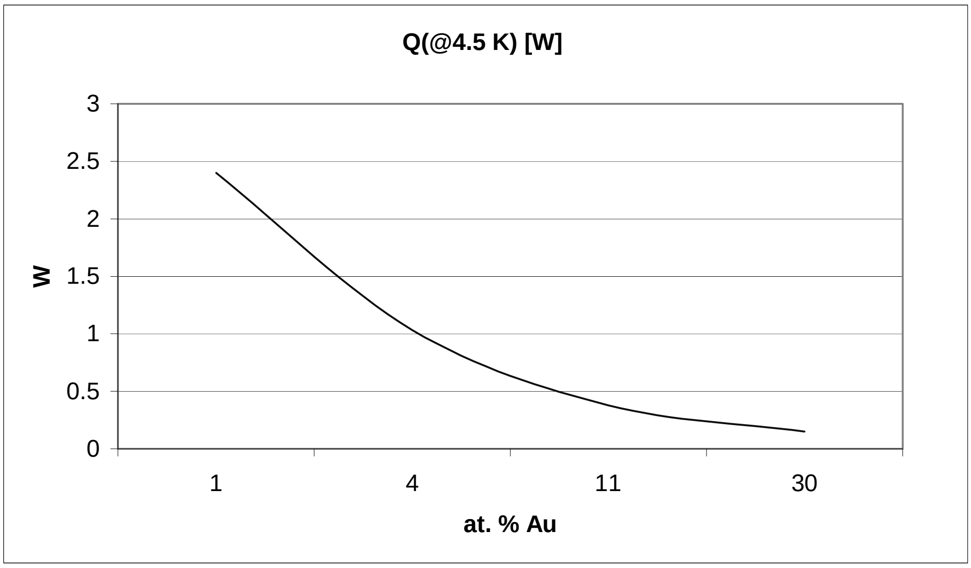

Figure 8-12. Heat flow in liquid helium at the low end of the current leads.

Due to the decreasing thermal conductivity the steady heat flux decreases while the atomic percentile of gold in the alloy increases.

When quench occurs, the different alloys behave differently according to the gold atomic percentile. For increasing Au at. percentage, the maximum temperature also increases. The conductor is more resistive and this conducts to higher temperature and higher heat flux. For an alloy 11% at. Au there is a maximum in the plot of the heat load and temperature. For higher values of gold enrichment the heat flux starts to decrease.

This implies that it is possible to find an optimum solution for the alloying.

Combining the costs and advantages of the two configurations it is easy to notice that a silver alloy 4% at. Au is one of the best possible solutions.

In Figure 8-13 are reported, in logarithmic scale, the trends of the heat flow and of the maximum temperature reached during the transient.

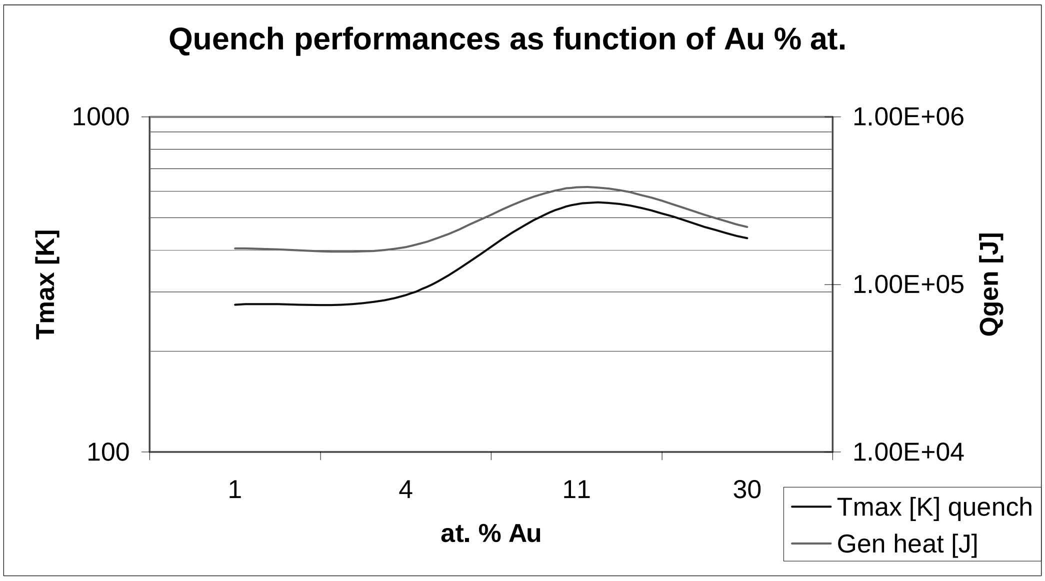

Figure 8-13. Temperature parameters as function of gold enrichment. The quench detection signal for in these transients is V_{lim} = 0.1 V.

About the choice of the metal alloy a last consideration has to be made regarding the linear thermal expansion.

The linear thermal expansion coefficient of superconducting oxides is of the order $\alpha \sim 10^{-7}$ [63], while for the metal matrix $\alpha \sim 10^{-5}$ [64]. Because of that difference is desirable to avoid thermal excursion. Since in the LHC machine the HTS current leads will work for several years and a good reliability is required, the number of possible quenches has to be reduced and the thermal excursion during a quench has to be limited. The final choice has to be made taking these consideration into account.

8.6 Magnet's time constant

Another parameter that influences the dynamic of the quench transient is the time constant of the magnet.

The equation that describes the current in a magnet is:

$$(54) \qquad L\frac{dI}{dt} + R(t)I(t) = 0$$

Solving this equation through the method of separation of variables I obtain:

$$\ln I = -\frac{1}{L}\int R(t)dI$$

Assuming small variation of the resistance of the magnet during the transient, the final solution is:

$$(55) \qquad I = I_0 e^{-\frac{R}{L}t}$$

The ratio L/R, where R is the electrical resistance of the magnet and L its inductance, is the time constant of the magnet:

$$\tau = \frac{L}{R}$$

As we can see it depends on the magnet and we cannot change it.

It is a matter of fact that small values of this constant lead to quick transient and then to lower temperature during quench and less propagation of the resistive zone.

The value of 120 s for τ is the biggest one for LHC. The worst transient is, then, the one which involves magnets with that constant.

If I compare the transient for τ = 120 s with one in which τ = 10 s, with the same conditions for the detection, I notice the influence of this constant.

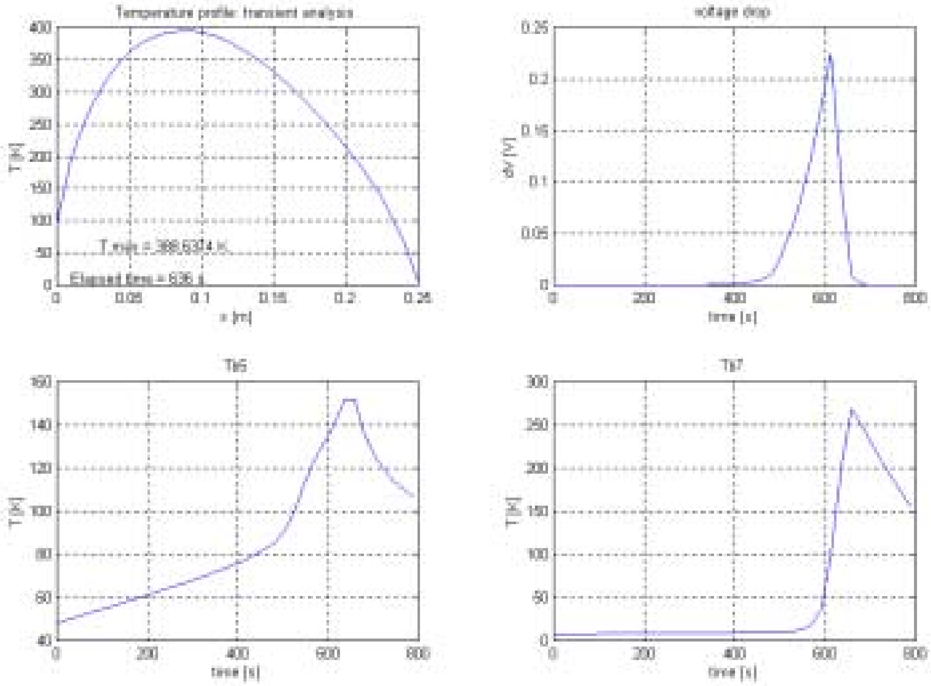

Figure 8-14. Temperature parameters of quench transition. Voltage limit integrated over 5 s, with a limit of 0.2 V. The time constant τ = 10 s.

Conclusions

The tests on the superconducting materials have demonstrated that, at the present time, the high temperature superconductor's technology is developed enough to provide tape conductors with high critical current density I_c = 100 A at 77 K in zero magnetic field.

To study the quench propagation in a HTS current leads I developed a theoretical thermal model for a HTS current lead. The superconducting material is BSCCO 2223 sheathed by a silver alloy with 4% at. Au.

In that model I numerically solved a non-linear system of equations for a gas-cooled lead. I took into account the temperature dependence of the material's properties both for the steady and the transient solution.

The magnetic evaluation allowed to define the geometry of the tapes assembly: the superconducting materials is strongly anisotropic and the orientation of the magnetic field lines respect to the transport axes of the conductor is determinant to achieve good transport performances. The current leads will operate in their self field: according to these evaluation the geometric layout of the assembly is such not to suffer for this magnetic field.

I compared the results of the theoretical model with the experimental results we obtained from the tests of a 13 kA prototype.

The forecasted steady heat flow at 4.5 K (Q = 1.03 W) is in good agreement with the experimental one (Q ~ 1 W) and demonstrates that with the HTS current leads a reduction by a factor 10 is possible respect to the conventional all-metal current leads.

I studied the influence of the cooling parameters on the lead performances. The gas cooling allows a heat flow reduction at 4.5 K by a factor 4 with respect to pure conduction cooling and this demonstrates the importance of cooling in order to reduce the cooling power of LHC. The cooling gas is provided by the evaporation of the liquid helium of the bath in which the cold end of the lead is dipped.

Another important consideration is the influence of the contact resistance due to the joint between the HTS and the bus-bar connection. A too high value for this contact resistance overheats the lower end of the lead causing a helium boil-off increase. Reasonable values for 13 kA prototypes are of the order of few nΩ. Computing the influence of the contact resistance on the heat flow at 4.5 K I noticed a small influence for values around the nΩ: it means that the soldering quality is less stringent than what one can estimate from pure conductor cooled conductors. In the 13 kA prototype this value was 2.9 nΩ which did not lead to any overheating. According to these considerations we can consider acceptable values up to 10 nΩ.

The solution of the quench transient well fits the experimental results. The total heat generated during a quench transient was computed: $W_q = 4.2\ 10^5$ J. The error with respect to the experimental one is within 7%. Moreover the experimental test does not allow to detect the maximum temperature reached during quench because of the limited number of sensing probes can be installed. The theoretical model gave a value T_{max} = 528 K for the prototype configuration.

Once the code has been validated I used it to study the influence of all the design parameters on quench evolution.

Firstly was demonstrated the importance of gas cooling also during quench. The presence of the gas cooling allows to reach lower maximum temperature during quench and avoids the resistive zone to propagate widely. This was a further confirmation about the importance of this solution for the LHC machine.

Another parameter that was investigated is the critical current of the HTS tapes. Nowadays the manufacturers of HTS reached values for the critical current density double than those of few years ago. The tapes installed in our prototype have I_c = 60 A (@77 K, in self-field). Tapes with I_c = 120 A (@77 K, in self-field) are now available. The number of tapes required in this case would be half the previous one with a consequent heat leak reduction. Nevertheless I demonstrated the use of such tapes would lead to thermal instability in case of quench because the smaller amount of metal stabiliser. Choosing this solution would require a new lead design which could take into account the introduction of an external protection shunt to protect the assembly in case of quench.

The importance of the metal matrix emerged from these analysis. The choice of a silver-gold alloy was imposed by thermal and chemical considerations. Thermally: alloying silver with gold reduces its thermal conduction; chemically because alloying silver with other metal like copper causes degradation of the superconducting oxide properties. The atomic percentage of gold in the alloy was chosen according to some thermal considerations. The alloying with gold reduces the thermal conduction but also increases the electrical resistivity. During quench an alloy richer in gold will lead to higher temperatures. According to the parametric analysis the optimum, according to the heat flow reduction and maximum temperature increase, is an atomic percentage between 2 and 6 %.

The filling factor (*fu*) of the tape was the other parameter which characterised the tapes. The filling factor represents the percentile amount of metal in the tape's cross section. The reduction of the metal cross section causes thermal instability during quenches as well as a reduction of the heat leak in the normal working conditions. It is remarkable that for small increases of *fu* (from 0.27 to 0.5) the disadvantage due to a higher maximum temperature reached during quench is overcame by a little resistive zone propagation with an overall advantage for the assembly. From this parametric analysis emerged that a good solution to limit the resistive zone propagation during quench is to slightly vary the filling factor, *fu*.

Finally, a parametric study on the importance of a quench detection signal was done. The protection signal used for the tests was the instant voltage drop across the HTS; the limit was set to V_{lim} = 0.25 V. It was seen this value is too high. In order to safely protect the HTS a value of the order of V_{lim} = 0.005 V is required.

According to the technical difficulty to detect such small signal, during the operation of the LHC, I chose the integrated-signal system to set up the quench detection. Using an integrated signal over a small time interval (5 s), was possible to fix the detection signal to V_{lim} = 0.02 V, integrated over 5 s. This value is not difficult to detect and does not suffer the background noise of LHC's electronics allowing a safe quench detection.

In conclusion I can say the thermal model is in good agreement with the experimental measurements.

Using the HTS technology allows reducing the heat leak into the liquid helium bath by a factor 10 with respect the all-metal current lead. Using the gas-cooling scheme allows a reduction of the heat load by a factor of 4 with respect to the pure conduction scheme.

A safe protection voltage for the assembly is 0.02 V integrated over 5 s.

Appendix

Computer programs

Matlab listing

Steady solution

```
% 12/01/2001
%
% Theoretical model for heat exchange in a current lead.
%
% steady case
% real convection
% k=k(T), h=h(T)
%
% steady.M
%
% *********** numerical model **************
%
%
% file inventory m_inter.m mass iterations
%
% strebC10.txt
% strebC13.txt
% strebC16.txt temperature profile’s files from => streb.m
%
% with contact resistance
% k values from papers by Isawa

close all;
clear all;
clc

T0=50;                  % [K] upper cup’s temperature
TN=4.5;                 % [K] lower cup’s temperature
L=0.250;                % [m] length of the HTSC
n=470;                  % number of tapes required
A=(0.25*3.25)*1e-6*n;      % [m²] total cross section of the assembly
C=13e-3*n/10;           % [m] wet perimeter
S=4*5*1e-6*n/10;           % [m²] cross section of the channel
Deq=4*S/C;              % [m] equivalent diameter of the channel
hfg=23000;              % [J/kg] latent heat for helium
cp=5.4124*1e3;             % [J/kg/K] medium specific heat 4.5-50 K (5.47
at 4.5 He)
rho=3.6037;             % [kg/m³] mean density for He
```

```
fu=0.27;                % utilization factor Ah/At


ak=0.578681;
bk=39.523;              % coefficients of the interpolation polynomial 4%
wt
%ak=0.750895;
%bk=51.1064;            % coefficient for fu = 0.05
hm=3.656*0.0308/Deq;       % [W/m²/K]
ah=-.00019419;
bh=0.30805;
ch=9.1365;              % coefficients of the interpolation polynomial for
h: 4.5 - 50 K 2nd order

I=13000;                % [A]

Tlim=96;                % [K] critical temperature
Tcs=70;                 % [K] current sharing temperature
Tlim2=110;              % [K] critical temperature: end of transient
dVlim=0.2;              % [V] voltage limit for quench protection
Textr=800;              % [T] maximum allowable temperature

precisione=1e-6;           % set iteration precision

titolo='Contact resistance';
dati={'Rc [ohm]'};
def={'2.8e-9'};
lineno=1;
answer=inputdlg(dati,titolo,lineno,def);
string=answer{1};
Rcont=str2num(string)*A/1e-4; % [ohm m] contact resistance


% pure conduction
% constant properties

kag=ak*TN+bk;           % [W/m/K] tape's thermal conductivity @ 4.5 K

dx=5e-3;                % space discretization

x=0:dx:L;               % [m] space vector
Tk=T0+x./L*(TN-T0);        % [K] temperature distribution
Q2k=-kag*A*(TN-T0)/L;      % [W] heat load in liquid He, pure conductive
model
m0=Q2k/hfg;             % [kg/s] mass flow ratio


% properties function of T

d=-x./L.*(ak/2*(TN^2-T0^2)+bk*(TN-T0))-ak/2*T0^2-bk*T0;

T=(-bk+sqrt(bk^2-2*ak*d))/ak;
Q2kr=-kag*A*(T(end)-T(end-1))/dx;   % [W] heat load in liquid He, pure
conductive model
m0r=Q2kr/hfg;                       % [kg/s] mass flow ratio
Tr=T;                               % [K] temperature profile of pure
conduction


lx=length(x)-2;
delta=zeros(lx+1,1);
```

```
delta(end)=1;                       % set contact resistance


% initial guess for temperature profile

load strebC13.txt
T=strebC13(:,1);
teta=strebC13(:,2);


m=-kag*A/hfg/dx*(T(end)-T(end-1));     % [kg/s] steady mass ratio: initial
guess
Q2=-kag*A*(T(end)-T(end-1))/dx;        % [W] steady heat leak: initial
guess

l=0;
daitarn=0;
puffetta=0;
m1=1e-5;
m2=5e-5;                            % [kg/s] Initial guess for the mass
flow rate

tic
while puffetta==0
   tetan=teta;
   Tn=T;
   Q2n=Q2;
   h=(ah*tetan.^2+bh*tetan+ch);        % [W/m²/K]
   k=ak.*Tn+bk;                        % [W/m/K]
   beta=C.*h*4*dx^2/A;
   l=l+1

while daitarn==0

   % first run
   alfa=m1*cp/C./h/dx;

   for z=lx+1:-1:2
      MA=[8*k(z)+beta(z) -beta(z);1 -(1+alfa(z))];
      MB=[(Tn(z+1)-Tn(z-1))*(k(z+1)-k(z-1))+4*k(z)*(Tn(z+1)+Tn(z-
1))+Rcont*I^2*4*dx^2/A*delta(z) ; -alfa(z)*tetan(z+1)];

      X=MA\MB;
      T(z)=X(1);
      teta(z)=X(2);
   end
   teta(1)=(T(1)+beta(1)*teta(2))/(1+beta(z));
   mc1=-kag*A/hfg/dx*(T(end)-T(end-1));

   % second run
   alfa=m2*cp/C./h/dx;

   for z=lx+1:-1:2
      MA=[8*k(z)+beta(z) -beta(z);1 -(1+alfa(z))];
      MB=[(Tn(z+1)-Tn(z-1))*(k(z+1)-k(z-1))+4*k(z)*(Tn(z+1)+Tn(z-
1))+Rcont*I^2*4*dx^2/A*delta(z) ; -alfa(z)*tetan(z+1)];

      X=MA\MB;
      T(z)=X(1);
      teta(z)=X(2);
   end
```

```
   teta(1)=(T(1)+beta(1)*teta(2))/(1+beta(z));
   mc2=-kag*A/hfg/dx*(T(end)-T(end-1));

   % Callback to the interpolation function
   m=m_inter(m1,mc1,m2,mc2);

   % check of the convergence
   alfa=m*cp/C./h/dx;

   for z=lx+1:-1:2
      MA=[8*k(z)+beta(z) -beta(z);1 -(1+alfa(z))];
      MB=[(Tn(z+1)-Tn(z-1))*(k(z+1)-k(z-1))+4*k(z)*(Tn(z+1)+Tn(z-
1))+Rcont*I^2*4*dx^2/A*delta(z) ; -alfa(z)*tetan(z+1)];

      X=MA\MB;
      T(z)=X(1);
      teta(z)=X(2);
   end
   teta(1)=(T(1)+beta(1)*teta(2))/(1+beta(z));
   mc=-kag*A/hfg/dx*(T(end)-T(end-1));


   if abs((m-mc)/m)<precisione
      daitarn=1;
   else
      if abs(m-m1)<abs(m-m2)
         m2=m;
      else
         m1=m;
      end
   end

end

Q2=-kag*A*(T(end)-T(end-1))/dx;
if abs((Q2n-Q2)/Q2n)<precisione,puffetta=1;end
daitarn=0;
end

toc

disp('Properties function of T')
disp('Pure conduction')
disp(['Conduction heat leak = ',num2str(Q2kr),' W.'])
disp(['Evaporating mass for Helium = ',num2str(m0r),' kg/s.'])
disp('With convection')
disp(['Convection heat leak = ',num2str(Q2),' W.'])
disp(['Evaporating mass for Helium = ',num2str(m),' kg/s.'])

figure(1)
set(gca,'FontName','Times new roman','FontSize',12)
hold on
title('Temperature profile: properties function of T')
grid on
xlabel('x [m]')
ylabel('T [K]')
plot(x,Tk,x,T,x,teta)
legend('conduction profile','convection profile','helium profile')

text(0.02,6,['m =',num2str(m),' kg/s'])
text(0.02,11,['Q2 =',num2str(Q2),' W'])
```

```
text(0.02,16,['mk =',num2str(m0r),' kg/s'])
text(0.02,21,['Q2k =',num2str(Q2kr),' W'])
```

Mass interpolation

```
function m=m_inter(m1,mc1,m2,mc2)

q=(mc2-mc1)/(m2-m1);
m=(mc1-q*m1)/(1-q);


% Interpolation function for mass iteration.
```

Unsteady solution: conduction only

```
% 12/01/2001
% Thesis
%
% Theoretical model for heat exchange in a current lead.
%
% pure conduction
%
% UstCOND.M
%
% *********** numerical model **************
%
% unsteady case
% k,h =f(T)
%
% FILE INVENTORY
%
% steady.txt data files for the temperature profile
% m_iter.m function's file for m interpolation
% steady case by file steady.m
%

clc
clear all; close all

% Input Data

T0=50;                  % [K] upper cup's temperature
TN=4.5;                 % [K] lower cup's temperature
L=0.250;                % [m] length of the HTSC
n=470;                  % number of tape required
A=(0.25*3.25)*1e-6*n;      % [m²] total cross section of the assembly
C=13e-3*n/10;           % [m] wet perimeter
S=4*5*1e-6*n/10;           % [m²] cross section of the channel
Deq=4*S/C;              % [m] equivalent diameter of the channel

I=13000;                % [A]
Rcont=2.8e-9;           % [Ohm] contact resistance
fu=0.27;                % utilization factor Ah/At

% ***** Helium properties *****

hfg=23000;              % [J/kg] latent heat for helium
cp=5.4124*1e3;             % [J/kg/K] medium specific heat 4.5-50 K (5.47
at 4.5 He)
```

```
rho=3.6037;             % [kg/m³] mean density for He

% ***** Tape properties *****

rhosc=10.34*1e3;           % [kg/m³]density of HTSC

% Specific heat [J/kg/K]
Tcp=4:2:300;            % [K] vector of temperature range for the specific
heat
T1s=[4 175];
c1s=[3 385];
p=polyfit(T1s,c1s,1);
cpb=polyval(p,Tcp);        % [J/kg/K] specific heat of BSCCO
T1m=[4 6 8 10 15 20 25 30 40 50 60 70 80 90 100 120 140 160 180 200 220 240
260 280 300 400 600]; % [K]
cpag=[.124 .39 .91 1.8 6.4 15.5 28.7 44.2 78 108 133 151 166 177 187 200
209 216 221 225 228 231 234 235 236 241 251];% [J/kg K]
cpau=[.16 .5 1.2 2.2 7.4 15.9 26.3 37.1 57.2 72.6 84.2 92.8 99.2 104.3
108.3 113.7 117.5 120.2 122.1 123.5 124.7 125.7 126.7 127.6 128.5 133
142];% [J/kg K]
atpr=4*.55/100;                  % atomic percentage
c1m=(1-atpr).*cpag+atpr.*cpau;   % [J/kg/K] vector of specific heat of the
metal matrix Ag+Au 4% at
cpmed=mean(c1m);
cpm=spline(T1m,c1m,Tcp);         % [J/kg/K] specific heat of the metal
matrix Ag+Au 4% at

cpe=cpb*fu+cpm*(1-fu);           % [J/kg/K] equivalent specific heat of the
tape

% Thermal conductivity

ak=0.578681;
bk=39.523;              % coefficients of the interpolation polynomial 4%
wt

% Electrical resistivity

hm=3.656*0.0308/Deq;       % [W/m²/K]
ah=-.00019419;
bh=0.30805;
ch=9.1365;              % coefficients of the interpolation polynomial for
h: 4.5 - 50 K 2nd order
rhoelm=6.8e-9;          % [OHM m] mean electrical resistivity of AgAu sheat
4.5 - 50 K
arh=5.2535e-11;
brh=5.3281e-9;          % coefficients of the interpolation polynomial for
rhoel AgAu
arhbi=4.8143e-010;         % coefficients of the interpolation polynomial
for rhoel BSCCO: transient
brhbi=-4.0257e-008;
arhbi2=1.3333e-009;        % coefficients of the interpolation polynomial
for rhoel BSCCO up to 400K
brhbi2=-4.0000e-008;

% Critical parameters of superconductor

Tlim=96;                % [K] critical temperature
Tcs=70;                 % [K] current sharing temperature
Tlim2=110;              % [K] critical temperature: end of transient
dVlim=0.25;             % [V] voltage limit for quench protection
```

```
Textr=700;              % [T] maximum allowable temperature

fc=1.7;                 % empirical factor => steel matrix


% ******* Numerical evaluation *******

precisione=1e-8;           % iteration precision


% Steady solution: pure conduction profile

dx=5e-3;                % space discretization
x=0:dx:L;               % [m] space vector

kag=ak*TN+bk;           % [W/m/K] thermal conductivity @ 4.5 K

Tk=T0+x./L*(TN-T0);        % [K] temperature distribution
Q2k=-kag*A*(TN-T0)/L;      % [W] heat load in liquid He, pure conductive
model
m0=Q2k/hfg;             % [kg/s] mass flow ratio

d=-x./L.*(ak/2*(TN^2-T0^2)+bk*(TN-T0))-ak/2*T0^2-bk*T0;

T=(-bk+sqrt(bk^2-2*ak*d))/ak;
Q2kr=-kag*A*(T(end)-T(end-1))/dx;   % [W] heat load in liquid He, pure
conductive model
m0r=Q2kr/hfg;                       % [kg/s] mass flow ratio

% display of steady data

disp(’Steady solution’)
disp(’Pure conduction: k = constant’)
disp([’Conduction heat leak = ’,num2str(Q2k),’ W.’])
disp([’Evaporating mass for Helium = ’,num2str(m0),’ kg/s.’])
disp(’Pure conduction: k(T)’)
disp([’Conduction heat leak = ’,num2str(Q2kr),’ W.’])
disp([’Evaporating mass for Helium = ’,num2str(m0r),’ kg/s.’])

figure(1)
set(gca,’FontName’,’Times new roman’,’FontSize’,12)
hold on
title(’Temperature profile: properties function of T’)
grid on
xlabel(’x [m]’)
ylabel(’T [K]’)
plot(x,Tk,x,T)
legend(’Constant properties’,’Properties f(T)’)

text(0.02,16,[’mk =’,num2str(m0),’ kg/s’])
text(0.02,21,[’Q2k =’,num2str(Q2k),’ W’])
text(0.02,6,[’mkr =’,num2str(m0r),’ kg/s’])
text(0.02,11,[’Q2kr =’,num2str(Q2kr),’ W’])




% Transient solution
% Input transient parameters

titolo=’Intervallo temporale’;
```

```
dati={’Number of time steps’,’dt’,’Tau decay constant’};
def={’1000’,’0.1’,’120’};
lineno=3;
answer=inputdlg(dati,titolo,lineno,def);
string=answer{1};
nnod=str2num(string);   % No of time steps
string=answer{2};
dt=str2num(string);     % dt
string=answer{3};
tau=str2num(string);    % [s] current decay constant


titolo=’Heating parameters’;
dati={’Heating temperature’,’Heating wideness’,’Heating rateo’};
def={’96’,’1’,’0.07’};
lineno=3;
answer=inputdlg(dati,titolo,lineno,def);
string=answer{1};
Tpeak=str2num(string);  % Peak temperature
string=answer{2};
n=str2num(string);      % heating wideness
string=answer{3};
dTdt=str2num(string);   % [K/sec] heating rate


figure(2)
set(gca,’FontName’,’Times new roman’,’FontSize’,12)
hold on
subplot(221);plot(x,T)
title(’Temperature profile: initial value’)
grid on
xlabel(’x [m]’)
ylabel(’T [K]’)
subplot(222);title(’voltage drop’)
hold on
grid on
xlabel(’time [s]’)
ylabel(’dV [V]’)
subplot(223);title(’Tb5’)
hold on
grid on
xlabel(’time [s]’)
ylabel(’T [K]’)
subplot(224);title(’Tb7’)
hold on
grid on
xlabel(’time [s]’)
ylabel(’T [K]’)


% setup variables

lx=length(T)-2;




minni=0;
pluto=0;
gpstep=10;
grandepuffo=0;                        % check counters
ll=1;
```

```
Tmax=max(T);                        % [K] max temperature of the leads
Tvect=[T(2) mean(T(41:42))];        % [K] vector of temperature
time=[0];
I0=I;

T=T’;

nn=9;                               % current sharing parameters
rho0=5e-8;                          % [Ohm m] rho(125K)
J0=-3.4309e1*125+2.6066e1;          % [A/cm²]

tic

for t=0:dt:nnod*dt

   if Tmax<=max(T)
      Tmax=max(T);
   else
      pluto=1;
   end
   if T(1)<Tpeak & minni==0
      T(1:n)=T(1)+dTdt*dt;          % heating routine
   end
   if minni==1 & T(n+1)<=T(1) & T(1)>T0
      T(1)=T(n+1);                  % cooling routine
      if T(1)<T0,T(1)=T0;end
   end
   if minni==1
      I=I0*exp(-(t-tstar)/tau);
   end

   k=ak.*T+bk;                      % [W/m/K]
   cpsc=spline(Tcp,cpe,T);

   alfa=1/rhosc./cpsc(2:lx+1);
   r=alfa.*dt/dx^2;

   eps1=T>=Tcs & T<Tlim;
   eps2=T>=Tlim & T<Tlim2;
   eps3=T>=Tlim2;

   if max(eps1)==1 | max(eps2)==1 | max(eps3)==1
      J=-3.4309e1.*T+2.6066e1;      % [A/cm²]
      rhocs=rho0*(J./J0).^(nn-1).*eps1;% [Ohm m]
      rhobi=(arhbi.*T+brhbi).*eps2;
      rhobi2=(arhbi2.*T+brhbi2).*eps3;

      rhoel=rhocs+rhobi2+rhobi;     % [Ohm m] BSCCO
      rhoag=(arh.*T+brh);           % [Ohm m] AgAu alloy.

      rhoeq=(rhoag.*rhoel)./((1-fu).*rhoel+fu.*rhoag);   %      [Ohm      m]
equivalent resistivity for the parallel
   else
      rhoeq=zeros(lx+2,1);
   end

   Rc=rhoeq(2:lx+1).*I^2/A^2/rhosc./cpsc(2:lx+1);

   dv=0;
```

```
   ad=(r/4.*(k(3:lx+2)-k(1:lx))-r.*k(2:lx+1));
   ac=1+2*r.*k(2:lx+1);
   au=(-r/4.*(k(3:lx+2)-k(1:lx))-r.*k(2:lx+1));

   MA=spdiags([[ad(2:end);0] ac [0;au(1:end-1)]],-1:1,lx,lx);

   BA=T(2:end-1)+Rc*dt;


   BA(1)=BA(1)-ad(1)*T(1);
   BA(end)=BA(end)-au(end)*TN;

   X=MA\BA;


   T=[T(1);X;TN];


   DV=I/(A*(1-fu))*dx/2*(rhoeq(1:lx-1)+rhoeq(2:lx));
   dv=sum(DV);

   if grandepuffo==gpstep
      time=[time t];
      hold on
      if pluto==0
         clf
         subplot(221);plot(x,T,'b')
         text(.01,10,['Elapsed time = ',num2str(t),' s.'])
         text(.03,60,['T heated = ',num2str(T(n)),' K.'])
      end

      dV(ll)=dv;                            % [V] vector of tensions
      current(ll)=I;                        % [A] vector of currents
      subplot(222);plot(time(1:end-1),dV)

      Tvect=[Tvect;T(2) mean(T(41:42))];        % [K] vector of temperature
      subplot(223);plot(time,Tvect(:,1))
      subplot(224);plot(time,Tvect(:,2))
      pause(.0001)
      grandepuffo=0;
      ll=ll+1;
   else
      grandepuffo=grandepuffo+1;
   end

   if max(T)>Textr,break,end
   if dv>dVlim & minni==0
      tstar=t;
      minni=1
   end
end
toc

subplot(221);title('Temperature profile: transient analysis')
hold on
grid on
xlabel('x [m]')
ylabel('T [K]')
subplot(222);title('voltage drop')
hold on
grid on
```

```
xlabel(’time [s]’)
ylabel(’dV [V]’)
subplot(223);title(’Tb5’)
hold on
grid on
xlabel(’time [s]’)
ylabel(’T [K]’)
subplot(224);title(’Tb7’)
hold on
grid on
xlabel(’time [s]’)
ylabel(’T [K]’)


Q2t=-kag*A*(T(end)-T(end-1))/dx;             % [W] heat leak
m=Q2t/hfg;                                % [kg/s] mass flow ratio
Wt=sum(dV.*current*dt*(gpstep+1));           % [J] generated heat

disp(’ ’)
disp([’Elapsed time = ’,num2str(t),’ s.’])
disp(’Transient analysis’)
disp([’Maximum temperature of the leads = ’,num2str(Tmax),’ K’])
disp([’Convection heat leak = ’,num2str(Q2t),’ W.’])
disp([’Evaporating mass for Helium = ’,num2str(m),’ kg/s.’])
disp([’Total generated heat = ’,num2str(Wt),’ J.’])


figure(3)
set(gca,’FontName’,’Times new roman’,’FontSize’,12)
hold on
plot(time(1:end-1),dV,time(1:end-1),current*1e-5)
title(’Voltage drop as a function of time’)
grid on
xlabel(’t [seconds]’)
ylabel(’dV [V]’)
legend(’Voltage’,’Current’)


figure(4)
set(gca,’FontName’,’Times new roman’,’FontSize’,12)
hold on
plot(time,Tvect)
title(’Temperature at the temperature tap’)
grid on
xlabel(’t [seconds]’)
ylabel(’T [K]’)
legend(’T top end’,’T in the middle’)
```

Unsteady solution: real case

```
% 12/01/2001
% Thesis
%
% Theoretical model for heat exchange in a current lead.
%
% REAL convection
%
% UstR.M
%
% *********** numerical model **************
```

```
%
% unsteady case
% k,h =f(T)
%
% linear interpolation for m iterations
%
% FILE INVENTORY
%
% steady.txt data file for the steady temperature profile
% m_iter.m function’s file for m interpolation
% steady case by file steady.m

clc
clear all; close all

% Input Data

T0=50;                  % [K] upper cup’s temperature
TN=4.5;                 % [K] lower cup’s temperature
L=0.250;                % [m] length of the HTSC
n=470;                  % number of tape required
A=(0.25*3.25)*1e-6*n;      % [m²] total cross section of the assembly
C=9e-3*n/10;            % [m] wet perimeter
S=4*3*1e-6*n/10;           % [m²] cross section of the channel
Deq=4*S/C;              % [m] equivalent diameter of the channel

I=13000;                % [A]
Rcont=2.8e-9;           % [Ohm] contact resistance
fu=0.27;                % utilization factor Ah/At

% ***** Helium properties *****

hfg=23000;              % [J/kg] latent heat for helium
cp=5.4124*1e3;             % [J/kg/K] medium specific heat 4.5-50 K (5.47
at 4.5 He)
rho=3.6037;             % [kg/m³] mean density for He

% ***** Tape properties *****

rhosc=10.34*1e3;                 % [kg/m³]   density of HTSC

% Specific heat [J/kg/K]
Tcp=4:2:300;                  % [K] vector of temperature range for the
specific heat
T1s=[4 175];
c1s=[3 410];
p=polyfit(T1s,c1s,1);
cpb=polyval(p,Tcp);              % [J/kg/K] specific heat of BSCCO
T1m=[4 6 8 10 15 20 25 30 40 50 60 70 80 90 100 120 140 160 180 200 220 240
260 280 300 400 600]; % [K]
cpag=[.124 .39 .91 1.8 6.4 15.5 28.7 44.2 78 108 133 151 166 177 187 200
209 216 221 225 228 231 234 235 236 241 251];% [J/kg K]
cpau=[.16 .5 1.2 2.2 7.4 15.9 26.3 37.1 57.2 72.6 84.2 92.8 99.2 104.3
108.3 113.7 117.5 120.2 122.1 123.5 124.7 125.7 126.7 127.6 128.5 133
142];% [J/kg K]
atpr=4*.55/100;                  % atomic percentage
c1m=(1-atpr).*cpag+atpr.*cpau;   % [J/kg/K] vector of specific heat of the
metal matrix Ag+Au 4% at
cpmed=mean(c1m);
cpm=spline(T1m,c1m,Tcp);         % [J/kg/K] specific heat of the metal
matrix Ag+Au 4% at
```

```
cpe=cpb*fu+cpm*(1-fu);           % [J/kg/K] equivalent specific heat of the
tape

% Thermal conductivity
ak=0.578681;
bk=39.523;              % coefficients of the interpolation polynomial 4%
wt
%ak=0.888166;
%bk=94.7716;            % coefficient for the interpolation polynomial 15%
at. Au

% Electrical resistivity
hm=3.656*0.0308/Deq;       % [W/m²/K]
ah=-.00019419;
bh=0.30805;
ch=9.1365;              % coefficients of the interpolation polynomial for
h: 4.5 - 50 K 2nd order
rhoelm=6.8e-9;          % [OHM m] mean electrical resistivity of AgAu sheat
4.5 - 50 K
arh=5.2535e-11;
brh=5.3281e-9;          % coefficients of the interpolation polynomial for
rhoel AgAu 4% wt
%arh=2.7419e-11;
%brh=3.8184e-9;            % different Au %

arhbi=4.8143e-010;         % coefficients of the interpolation polynomial
for rhoel BSCCO: transient
brhbi=-4.0257e-008;
arhbi2=1.3333e-009;        % coefficients of the interpolation polynomial
for rhoel BSCCO up to 400K
brhbi2=-4.0000e-008;

% Critical parameters of superconductor
Tlim=96;                % [K] critical temperature
Tcs=70;                 % [K] current sharing temperature
Tlim2=110;              % [K] critical temperature: end of transient
Textr=700;              % [T] maximum allowable temperature

fc=1.7;                 % empirical factor => steel matrix

% Quench protection
disp('Kind of protection')
disp('1. dV limit')
disp('2. integrated signal')

pause(3)

titolo='Protection';
dati={'Which kind'};
def={'1'};
lineno=1;
answer=inputdlg(dati,titolo,lineno,def);
string=answer{1};
kpro=str2num(string);      % [V] voltage limit

switch kpro
case 1
   titolo='Voltage Limit';
   dati={'Voltage drop limit [V]'};
   def={'0.1'};
```

```
   lineno=1;
   answer=inputdlg(dati,titolo,lineno,def);
   string=answer{1};
   dVlim=str2num(string);  % [V] voltage limit
case 2
   titolo=’Integrated signal’;
   dati={’Voltage limit [V]’,’Integration time [s]’};
   def={’0.2’,’5’};
   lineno=2;
   answer=inputdlg(dati,titolo,lineno,def);
   string=answer{1};
   dVlim=str2num(string);  % [V] voltage limit
   string=answer{2};
   tauint=str2num(string); % [V] voltage limit
end


% ******* Numerical evaluation *******

precisione=1e-6;           % iteration precision

% Steady solution: pure conduction profile

dx=5e-3;                % space discretization
x=0:dx:L;               % [m] space vector

kag=ak*TN+bk;           % [W/m/K] thermal conductivity @ 4.5 K

Tk=T0+x./L*(TN-T0);        % [K] temperature distribution
Q2k=-kag*A*(TN-T0)/L;      % [W] heat load in liquid He, pure conductive
model
m0=Q2k/hfg;             % [kg/s] mass flow ratio

d=-x./L.*(ak/2*(TN^2-T0^2)+bk*(TN-T0))-ak/2*T0^2-bk*T0;

T=(-bk+sqrt(bk^2-2*ak*d))/ak;
Q2kr=-kag*A*(T(end)-T(end-1))/dx;   % [W] heat load in liquid He, pure
conductive model
m0r=Q2kr/hfg;                       % [kg/s] mass flow ratio

% display of steady data

disp(’Pure conduction: k = constant’)
disp([’Conduction heat leak = ’,num2str(Q2k),’ W.’])
disp([’Evaporating mass for Helium = ’,num2str(m0),’ kg/s.’])
disp(’Pure conduction: k(T)’)
disp([’Conduction heat leak = ’,num2str(Q2kr),’ W.’])
disp([’Evaporating mass for Helium = ’,num2str(m0r),’ kg/s.’])

figure(1)
set(gca,’FontName’,’Times new roman’,’FontSize’,12)
hold on
title(’Temperature profile: properties function of T’)
grid on
xlabel(’x [m]’)
ylabel(’T [K]’)
plot(x,Tk,x,T)
legend(’Constant properties’,’Properties f(T)’)

text(0.02,16,[’mk =’,num2str(m0),’ kg/s’])
text(0.02,21,[’Q2k =’,num2str(Q2k),’ W’])
```

```
text(0.02,6,[’mkr =’,num2str(m0r),’ kg/s’])
text(0.02,11,[’Q2kr =’,num2str(Q2kr),’ W’])



% load temperature profile from .txt files

load steady.txt                     % alternative solution mod9_1mm.txt

T=steady(:,1);                   % [K] HTS temperature
teta=steady(:,2);                   % [K] He temperature
m=-kag*A/hfg/dx*(T(end)-T(end-1));  % [kg/s] equilibrium temperature
Q2=-kag*A*(T(end)-T(end-1))/dx;

hold on
plot(x,T,’k’,x,teta,’r’)
legend(’Constant properties’,’Properties f(T)’,’real convection
profile’,’helium profile’)

text(0.02,26,[’m =’,num2str(m),’ kg/s’])
text(0.02,31,[’Q2 =’,num2str(Q2),’ W’])


% ***************** transient analysis
% ********   REAL CONVECTION
% Input transient parameters

titolo=’Intervallo temporale’;
dati={’transient length’,’Initial dt’,’Tau decay constant’};
def={’400’,’2’,’120’};
lineno=3;
answer=inputdlg(dati,titolo,lineno,def);
string=answer{1};
nnod=str2num(string);   % No of time steps
string=answer{2};
dt=str2num(string);     % dt
string=answer{3};
tau=str2num(string);    % [s] current decay constant


precisione=1e-6;        % iteration precision


titolo=’Heating parameters’;
dati={’Heating temperature’,’Heating wideness’,’Heating rateo’};
def={’96’,’1’,’0.07’};
lineno=3;
answer=inputdlg(dati,titolo,lineno,def);
string=answer{1};
Tpeak=str2num(string);  % Peak temperature
string=answer{2};
n=str2num(string);      % heating wideness
string=answer{3};
dTdt=str2num(string);   % [K/sec] heating rateo


figure(2)
set(gca,’FontName’,’Times new roman’,’FontSize’,12)
hold on
subplot(221);plot(x,T)
title(’Temperature profile: initial value’)
```

```
grid on
xlabel('x [m]')
ylabel('T [K]')
subplot(222);title('voltage drop')
hold on
grid on
xlabel('time [s]')
ylabel('dV [V]')
subplot(223);title('Tb5')
hold on
grid on
xlabel('time [s]')
ylabel('T [K]')
subplot(224);title('Tb7')
hold on
grid on
xlabel('time [s]')
ylabel('T [K]')

pause(1)


% setup variables

gamma=C/S/rho/cp;
BA=T(2:end-1);
BB=teta(2:end-1);

lx=length(x)-2;
ee=ones(lx,1);


ll=1;
tstar=0;
minni=0;                         % magnet's discharge
pluto=0;
goldrake=0;                      % mass iterations
puffetta=0;                      % properties iterations
grandepuffo=0;                   % plotting scanner
gpstep=10;                       % scanning step

m1=3e-5;                         % Initial guess for mass interpolation
m2=5e-5;
Tmax=max(T);                     % [K] max temperature of the leads
tetamax=teta(1);
Tvect=[T(2) mean(T(41:42))];

time=[0];                        % initializing variables
I0=I;
t=0;
l=0;
dV=0;
dvint=0;

nn=9;                            % current sharing parameters
rho0=5e-8;                       % [Ohm m] rho(125K)
J0=-3.4309e1*125+2.6066e1;          % [A/cm²]

tic

for t=0:dt:nnod*dt
```

```
   if Tmax<=max(T)
      Tmax=max(T);
   else
      pluto=1;
   end
   if tetamax<=teta(1),tetamax=teta(1);end
   if T(1)<Tpeak & minni==0
      T(1:n)=T(1:n)+dTdt*dt;
   end
   if minni==1 & T(n+1)<=T(1) & T(1)>T0
      T(1)=T(n+1);
      if T(1)<T0,T(1)=T0;end
   end
   if minni==1
     I=I0*exp(-(t+dt-tstar)/tau);
   end

   Tn=T;
   tetan=teta;
   Q2n=Q2;

   puffetta=0;                      % reinitializing counter

   while puffetta==0
      Tgue=T;                       % [K]
      tetague=teta;
      Q2gue=Q2;                        % [W]
      mgue=m;
      cpsc=spline(Tcp,cpe,Tgue)*fc;    % [J/kg/K] specific heat of the
tapes
      beta=C/A/rhosc./cpsc(2:lx+1);
      r=dt/dx^2/rhosc./cpsc(2:lx+1);

      k=(ak.*Tgue+bk);                 % [W/m/K]
      h=(ah.*tetague.^2+bh.*tetague+ch);  % [W/m²/K]

      eps1=Tgue>=Tcs & Tgue<Tlim;
      eps2=Tgue>=Tlim & Tgue<Tlim2;
      eps3=Tgue>=Tlim2;


      if max(eps1)==1 | max(eps2)==1 | max(eps3)==1
         J=-3.4309e1.*Tgue+2.6066e1;      % [A/cm²]
         rhocs=rho0*(J./J0).^(nn-1).*eps1;   % [Ohm m]
         rhobi=(arhbi.*Tgue+brhbi).*eps2;
         rhobi2=(arhbi2.*Tgue+brhbi2).*eps3;
         %rhobi2=1.4e-7.*eps4;

         rhoel=rhocs+rhobi2+rhobi;        % [Ohm m] BSCCO
         rhoag=(arh.*Tgue+brh);           % [Ohm m] AgAu alloy.

         rhoeq=(rhoag.*rhoel)./((1-fu).*rhoel+fu.*rhoag);   % [Ohm m]
equivalent resistivity for the parallel
      else
         rhoeq=zeros(lx+2,1);
      end

         Rc=rhoeq.*I^2/(A^2)/rhosc./cpsc;    % resistive term

         dv=0;
         goldrake=0;                      % reinitializing counters
```

```
while goldrake==0

   % first run
   delta=m1/S/rho;
   d=delta*dt/dx;
   ad=(r./4.*(k(3:lx+2)-k(1:lx))-r.*k(2:lx+1));
   ac=1+2.*r.*k(2:lx+1)+beta.*h(2:lx+1).*dt;
   au=(-r./4.*(k(3:lx+2)-k(1:lx))-r.*k(2:lx+1));

   MA=spdiags([[ad(2:end);0] ac [0;au(1:end-1)]],-1:1,lx,lx);
   MB=spdiags([-beta.*dt.*h(2:lx+1)],0,lx,lx);
   MC=spdiags([-gamma*dt.*h(2:lx+1)],0,lx,lx);
   MD=spdiags([(1+gamma*dt.*h(2:lx+1)+d) -d*ee],0:1,lx,lx);


   MM=[MA MB;MC MD];

   BA=Tn(2:end-1)+Rc(2:end-1).*dt;

   BA(1)=BA(1)-ad(1)*Tn(1);
   BA(end)=BA(end)-au(end)*TN;

   BB=tetan(2:end-1);
   BB(end)=BB(end)+TN*d/2;

   B=[BA;BB];

   X=MM\B;

   mc1=-kag*A/hfg/dx*(TN-X(lx));

   % second run
   delta=m2/S/rho;
   d=delta*dt/dx;
   MD=spdiags([(1+gamma*dt.*h(2:lx+1)+d) -d*ee],0:1,lx,lx);

   MM=[MA MB;MC MD];

   X=MM\B;

   mc2=-kag*A/hfg/dx*(TN-X(lx));

   % Callback to the function interpolation
   m=m_inter(m1,mc1,m2,mc2);

   % Iteration for convergence
   delta=m/S/rho;
   d=delta*dt/dx;
   MD=spdiags([(1+gamma*dt.*h(2:lx+1)+d) -d*ee],0:1,lx,lx);


   MM=[MA MB;MC MD];


   X=MM\B;

   T=[Tn(1);X(1:lx);TN];
   teta=[tetan(1);X(lx+1:end);TN];
   mc=-kag*A/hfg/dx*(TN-X(lx));
   if abs((m-mc)/m)<precisione
```

```
              goldrake=1;
            else
              if abs(m-m1)<abs(m-m2)
               m2=m;
              else
               m1=m;
              end
            end
         end
         if abs(mean(T-Tgue)/mean(Tgue))<precisione*100
            puffetta=1;
            T=Tgue;                                % [K] tape temperature
            teta=tetague;                          %    [K]    vapour    helium
temperature
            Q2=Q2gue;                              % [W] heat flow
            m=mgue;                                % [kg/s] mass flow rate
         end
      end

      DV=I/A*dx/2.*(rhoeq(1:lx+1)+rhoeq(2:lx+2));
      dv=sum(DV);                                  % [V] voltage drop

      switch kpro                                  % quench detection
      case 1
         if dv>dVlim & minni==0
            tstar=t+dt;
            minni=1;
         end
      case 2
         if l*dt<tauint
            dvint=dvint+dv*dt;
            l=l+1;
         else
            l=0;
            if dvint>dVlim & minni==0
              tstar=t+dt;
              minni=1;
            end
            dvint=0;
         end
      end

      if grandepuffo==gpstep
         time=[time t];

         if pluto==0                               %     Maximum     temperture
reached
            clf
            subplot(221);plot(x,T,’b’)
            text(.01,10,[’Elapsed time = ’,num2str(t),’ s.’])
            text(.03,60,[’T max = ’,num2str(Tmax),’ K.’])
         end

         dV(ll)=dv;                                % [V] vector of tensions
         current(ll)=I;                            % [A] vector of currents
         subplot(222);plot(time(1:end-1),dV)
         Tvect=[Tvect; T(2) mean(T(41:42))];          %    [K]    vector    of
temperature
         subplot(223);plot(time,Tvect(:,1))
         subplot(224);plot(time,Tvect(:,2))
         pause(.0001)
```

```
         grandepuffo=0;
         ll=ll+1;
      else
         grandepuffo=grandepuffo+1;
      end
end

toc

subplot(221);title(’Temperature profile: transient analysis’)
hold on
grid on
xlabel(’x [m]’)
ylabel(’T [K]’)
subplot(222);title(’voltage drop’)
hold on
grid on
xlabel(’time [s]’)
ylabel(’dV [V]’)
subplot(223);title(’Tb5’)
hold on
grid on
xlabel(’time [s]’)
ylabel(’T [K]’)
subplot(224);title(’Tb7’)
hold on
grid on
xlabel(’time [s]’)
ylabel(’T [K]’)


Q2t=-kag*A*(T(end)-T(end-1))/dx;
m=Q2t/hfg;                                % [kg/s] mass flow ratio
Wt=sum(dV.*current*dt*(gpstep+1));           % [W] generated heat

disp(’ ’)
disp([’Elapsed time = ’,num2str(t),’ s.’])
disp(’Transient analysis’)
disp([’Maximum temperature of the leads = ’,num2str(Tmax),’ K’])
disp([’Convection heat leak = ’,num2str(Q2t),’ W.’])
disp([’Evaporating mass for Helium = ’,num2str(m),’ kg/s.’])
disp([’Total generated heat = ’,num2str(Wt),’ J.’])


figure(3)
set(gca,’FontName’,’Times new roman’,’FontSize’,12)
hold on
plot(time(1:end-1),dV,time(1:end-1),current*1e-5)
title(’Voltage drop as a function of time’)
grid on
xlabel(’t [seconds]’)
ylabel(’dV [V]’)
legend(’Voltage’,’Current’)


figure(4)
set(gca,’FontName’,’Times new roman’,’FontSize’,12)
hold on
plot(time,Tvect)
title(’Temperature at the temperature tap’)
grid on
```

```
xlabel('t [seconds]')
ylabel('T [K]')
legend('T top end','T in the middle')
```

References

[1] The LHC study group, The Large Hadron Collider. Conceptual design, CERN/AC/95-05 (LHC), 1995.

[2] L.R. Evans, The Present Status of LHC, IEEE Transaction on Magnetics, Vol. 32, no. 4, 1996.

[3] P. Lebrun, Cryogenics for the large Hadron Collider, IEEE Transaction on Applied Superconductivity, Vol. 10, no. 1, 2000.

[4] L. R. Evans, The Large Hadron Collider – Present Status and Prospect, IEEE Transactions on Applied Superconductivity, Vol.10, no.1, 2000.

[5] T. M. Taylor, HTS Current Leads for the LHC, IEEE Transaction on Applied Superconductivity, Vol. 9, no. 2, 1999.

[6] A. Ballarino, High Temperature Superconducting current leads for the Large Hadron Collider, LHC Project Report 337, 1999.

[7] P. Schmüser, Superconductivity, CAS - CERN Accelerator School : Superconductivity in Particle Accelerators, Hamburg, Germany, 17 - 24 May 1995 / Ed. by Turner, Stuart - CERN, Geneva, 1996.

[8] S. Jin, Processing and properties of High Tc superconductors. Vol.1 Bulk material. AT & T Bell laboratories. World Scientific, 1992.

[9] A. Bourdillon & N. X. Tan Bourdillon, High Temperature Superconductors: Processing and Science, Academic press INC., 1993.

[10] N. M. Plakida, High-temperature superconductivity, Springer 1994.

[11] B. Seeber, Applied Superconductivity, Vol. 1. YoP publ. 1998.

[12] K. Salama, V. Selvamanickam, L. Gao and K. Sun.High, Current density in bulk Yba2Cu3Ox superconductor Appl. Phys. Lett. 54 (23), 1989 p.2352.

[13] Uri Dai, Guy Deutscher and Ralph Rosenbaum, Critical current of YBCO in strong applied fields, Appl. Phys. Lett. 51 (6), 10 August 1987.

[14] K. Heine, J. Tenbrink, M. Thoner, High-field critical current densities in BSCCO2212/Ag wires, Appl. Phys. Lett. 55 (23), 1989, p. 2441.

[15] R. Garrè, P. Crincoli, G. Lunardi and N. Tonarelli, Processing and critical currents of Ag sheathed Bi-based Superconducting wires and tapes. Europa metalli – LMI research centre. Supercond. Sci. Technol. 5 (1992), p.316.

[16] J. Bock and S. Elschner, Melt cast processed (MCP) BSCCO 2212 tubes for power applications up to 10 kA, ALCATEL ALSTHOM RECHERCHE. IEEE transactions on applied superconductivity, Vol. 5, no. 2, 1995, p.1409.

[17] J. Bock and S. Elschner, G. Brommer, High currents in MCP BSCCO 2212 bulk material, ALCATEL ALSTHOM RECHERCHE. IEEE transactions on magnetics, Vol. 32, no. 4, 1996, p.2724.

[18] M. S. Walker, C. M. Trautwein and L. R. Motowidlo, Practical coated BSCCO-2212 high Tc conductors IEEE transaction on applied superconductivity, Vol. 5, no. 2, 1995, p.1857.

[19] C. H. Rosner, M. S. Walker, P. Haldar and L. R. Motowidlo, Status of HTS superconductors: Progress in improving transport critical current densities in HTS Bi-2223 tapes and coils. Cryogenics 1992 Vol. 32, no. 11, p. 940.

[20] De la Fuente G. F., Huang Y. B., Angurel L. A., Larrea A., Ruiz M. T., Lera F., Navarro R., Powder in tube method achievements on HTSC wires and tapes. Superconductivity in Spain (1990-1992) Midas Program, p.195.

[21] Hiroyuki Fujishiro, Manabu Ikebe, Koshichi Noto and Michiaki Matsukawa, Low thermal Conductive Bi-2223 tapes sheathed with Ag-Au alloys, IEEE Transaction on Magnetics, Vol. 30 no. 4, July 1994.

[22] L. F. Goodrich and S. L. Bray, High T_c superconductors and critical current measurement, Cryogenics 1990, Vol. 30 August.

[23] ASM Handbook, Material Characterisation, Vol. 10, 1986.

[24] Vanderah, Chemistry of Superconductor materials. Noyes Pubbl. 1991

[25] A. Ballarino, Discendenti di corrente con materiale superconduttore ad alta temperatura per l'alimentazione dei magneti del Large Hadron Collider, PhD thesis, Politecnico di Torino, Torino, 1997.

[26] P.F. Herrmann, E. Beghin, G. Bottini, C. Cottevieille, A. Leriche, T. Verhaege and J. Bock, Test results of a 1 kA-20 kV HTSC current lead model, Cryogenics Vol. 34, n. 6, 1994.

[27] P. F. Herrmann, C. Cottevieille, G. Duperray, A. Leriche, T. Verhaege, C. Albrecht and J. Bock, Cryogenic load calculation of high T_c current lead, Cryogenics Vol. 33, n. 5, 1993.

[28] J. R. Hull, High temperature superconducting current leads for cryogenic apparatus, Cryogenics Vol. 29, December 1989.

[29] K. Maehata, T. Nishioka and K. Ishibashi, Design chart of high temperature superconducting gas cooled current leads, IEEE Transaction on applied superconductivity, vol. 5, n. 2 1995.

[30] R. Wesche and A. M. Fuchs, Design of superconducting current leads, Cryogenics Vol. 34, n. 2, 1994.

[31] A. Ballarino, A. Ijspeert, Expected Advantages and Disadvantages of High-T_c Current Leads for the Large Hadron Collider Orbit Correctors, CERN AT/93-31 (MA), LHC note 231, 1996.

[32] Yu. L. Buyanov, A. B. Fradkov and I. Yu Shebalin, A review of current leads for cryogenic devices, Cryogenics, April 1975.

[33] M. N. Wilson, Superconducting magnets, Oxford Science Publication, 1983.

[34] Yu. L. Buyanov, Current leads for use in cryogenic devices. Principle of design and formulae for design calculations, Cryogenics Vol. 25, February 1985.

[35] Jacob, Heat Transfer, John Wiley and Sons, 1955.

[36] A. Bacciotti, F. Ricci, Lezioni di Analisi Matematica 2, Levrotto & Bella, 1991.

[37] T. M. Shih, Numerical Heat Transfer, Springer, 1984.

[38] Joel H. Ferziger, M. Peric, Computational Methods for Fluid dynamics, Springer, 1999.

[39] J. L. Buchanan, P. R. Turner, Numerical methods and analysis, Mc Graw Hill, 1992.

[40] S. B. Kim, A. Ishiyama, H. Okada and S. Nomura, Normal-zone propagation properties in Bi-223/Ag superconducting multifilament tapes, Cryogenics Vol. 38, 8, 1998.

[41] HEPAK, program written by V. Arp, R. D. McCarty and B. A. Hands. The numerical output is consistent with tabulated helium properties in NIST TECH NOTE 1334 (1989).

[42] Wright, Patterson, A compendium of the properties of materials at low temperature, Wrigth Air Development Division, 1961.

[43] C. R. Berman, R. Mate, Phyl. Mag. (8) 3, 461-469, 1958.

[44] B. Panella, Lezioni di termocinetica, CLUT Torino.

[45] K. Maehata, T. Nishioka and K. Ishibashi, Design chart of High Temperature Superconducting Gas cooled current leads, IEEE Transaction on applied superconductivity, Vol. 5 n. 2, 1995.

[46] C. Boffa, P. Gregorio, Elementi di Fisica Tecnica, Levrotto & Bella, Torino, 1976.

[47] A. Badia, Y. B. Huang, G. F. de la Fuente, M. T. Ruiz, L. A. Angurel, F. Lera, C. Rillo and R. Navarro, Magnetic and electric transport properties of Ag/(Bi,Pb)-Sr-Ca-Cu-O superconducting fibres, Cryogenics vol. 32, 11, 1992.

[48] M. Ikebe, H. Fujishiro, T. Naito, and K. Noto, Simultaneous Measurement of Thermal Diffusivity and Conductivity Applied to Bi-2223 Ceramic Superconductors, Journal of the Physical Society of Japan, Vol 63, No 8, 1993.

[49] F. W. De Wette and A. Rahman, specific Heat below 3 K of Silver Gold alloys, Physical review, Vol. 176 n. 3, 1968.

[50] H. Fujishiro, M. Ikebe, K. Noto, T. Sasaoka and K. Nomura, thermal and electrical properties of AgAu and AgCu alloy tapes for metal stabilisers of oxide superconductors, Cryogenics 33, 1993.

[51] A. Rimikis, R. Kimmich and Th. Schneider, Investigation of n-values of Composite Superconductors, IEEE Transaction on applied superconductivity, Vol. 10 n.1, 2000.

[52] G. Balestrino, U. Gambardella, M. Marinelli, A. Paoletti, P. Paroli and G. Paternò, Electric, magnetic and transport critical current density behavior of the 2201, 2212 and 223 phases of BSCCO, Journal-of-Superconductivity (USA), pp: 1989, vol.2, no.3, p.387-94

[53] I. I. Akimov, N. I. Kozlenkova, P. A. Kuznetsov, D. N. Rakov, A. K. Shikov, Properties of Bi-2223/(Ag+Au) tapes, IEEE Transaction on applied superconductivity, Vol. 10 n.1, 2000.

[54] A. Sànchez, J. E. Rodriguez, A. Mariño, Thermoelectric and thermomagnetic effects of Ag-doped BSCCO samples, Physica B 284-288 (2000) 1940-1941.

[55] A. Ballarino, A. Bezaguet, P. Gomes, L. Metral, L. Serio and A. Suraci, A low heat inleak cryogenic station for testing HTS current leads for the Large Hadron Collider, LHC Project Report 320, 1999.

[56] B. A. Hands, Cryogenic Engineering, Academic Press, 1986.

[57] Lake Shore Cryotronics, Inc. Web site: http://www.lakeshore.com/

[58] A. Ballarino, L. Serio, tests results on the first 13 kA prototype HTS leads for the LHC, PAC, 1999 N.Y.

[59] Inst. Phys. Conf. Ser. No. 167, Quench protection of 13 kA HTS prototype leads for the LHC.

[60] L. Martini, F. Barberis, R. Berti, L. Bigoni, M. Putti, G. Volpini and F. Curcio, Quench propagation in AFM Bi-2223 conductors for current leads, IEEE Transaction on applied superconductors, 2000.

[61] S. Y. Seol and J. R. Hull, Transient analysis and burnout of high temperature superconducting current leads, Cryogenics, Vol. 33, 10, 1993.

[62] S. Y. Seol, J. R. Hull, M. C. Chyu, Optimisation of high-temperature superconductor current leads, IEEE Transaction on applied superconductivity, Vol. 5, 2, 1995.

[63] B. Seeber, Handbook of Applied Superconductivity, IoP, Vol. 1.

[64] NST, A compendium of the properties of materials at low temperature, Wright air development division, Part II.